

國立交通大學

電子工程學系電子研究所

博士論文

準彈性反射電子模擬與分析



**THE SIMULATION AND ANALYSIS
OF QUASI-ELASTICALLY
BACKSCATTERED ELECTRONS**

研究生：黎裕群 Yu-Chun Li

指導教授：桂正楣 Cheng-May Kwei


中華民國九十四年六月

準彈性反射電子模擬與分析
**THE SIMULATION AND ANALYSIS OF
QUASI-ELASTICALLY BACKSCATTERED
ELECTRONS**

研究生：黎裕群
指導教授：桂正楣

Student: Yu-Chun Li
Advisor: Cheng-May Kwei

國立交通大學
電子工程學系電子研究所
博士論文



**A Dissertation
Submitted to
Institute of Electronics
College of Electrical Engineering and
Computer Science
National Chiao Tung University
In Partial Fulfillment of the Requirements
For the Degree of
Doctor of Philosophy
In
Electronic Engineering**

**June 2005
Hsinchu, Taiwan, Republic of China**

中華民國 九十四 年 六 月

準彈性反射電子模擬與分析

研究生：黎裕群

指導教授：桂正楣

國立交通大學電子工程學系電子研究所

摘要

本論文在探討移動電子對固體做運動時而發生的彈性及非彈性交互作用，引用或研究相關的理論模式，並對從固體準彈性反射出來的電子做出模擬與分析。

在彈性交互作用方面，我們利用非相對論性及相對論性彈性交互作用模式，並配合自由原子位能及固體原子位能，來計算電子的微分彈性散射截面(elastic differential cross section: EDCS)，計算的結果，針對非相對論性及相對論性模式做出比較。利用所求得的微分彈性散射截面，可以得到電子在固體中移動時的彈性平均自由行徑(elastic mean free path: EMFP)，我們也計算了相對論性模式的彈性平均自由行徑，並對其做出分析。另外，化合物固體在電子的交互作用研究當中，也扮演重要角色，故而，我們根據化合物固體裡個別元素的彈性散射截面或彈性平均自由行徑，演示了化合物固體的總彈性散射截面及總彈性平均自由行徑的理論計算方法，並且也了解，電子在化合物固體裡碰撞個別元素的機率，此碰撞機率計算方式對後續的電子彈性波峰研究有所幫助。除此之外，由於電子在彈性碰撞過程中，還伴隨著反衝能量損失(recoil energy loss)，此反衝能量損失，可以透過Rutherford 彈性碰撞模型而求得，我們也演示其理論計算式，此計算式對於電子準彈性反射能譜的研究有所助益。

在非彈性交互作用方面，我們的目的是在推導一個可以適用於電子以任意方向入射或出射固體的非彈性交互作用模式。我們應用介電理論(dielectric response theory)，在滿足邊界條件之下，去解 Poisson 方程式，可以得到電子相對固體做運動時，而產生的感應電場(induced electric field)，利用作用在電子本身的感應電場，可以求得電子所受到的阻擋本領(stopping power)，透過此阻擋本領，並在動量積分上採用球座標系統，從而推導出了電子的非彈性微分倒數平均自由行徑(differential inverse inelastic mean free path: DIIMFP)、非彈性平均自由行徑(inelastic mean free path: IMFP)以及表面激發參數的計算式(surface excitation parameter: SEP)。配合 extended Drude 介電函數的使

用，我們根據所推式子而計算出，與電子位置、能量及運動方向有關的非彈性微分倒數平均自由行徑和非彈性平均自由行徑，以及與電子能量及運動方向有關的表面激發參數；並且發現表面激發參數遵守一個簡單的通式，在我們的研究當中，也對此通式的相關係數做出模擬，以適用於電子入射及出射不同固體的表面激發參數。由於所推導的非彈性交互作用模式，並不能包含電子在極高速運動之下而顯現出來的延遲效應(retardation effect)，故而，我們另針對極高速電子而推導一個含延遲效應之非彈性交互作用模式。同樣利用介電理論，去解 Maxwell 方程式，以類似於不含延遲效應之非彈性交互作用模式的推導過程，推導出了適用於極高速電子平行於固體表面運動時的阻擋本領、非彈性微分倒數平均自由行徑以及非彈性平均自由行徑，並與用傳統模式計算出的結果做出比較。

根據對彈性交互作用及非彈性交互作用的理論研究，我們利用 Monte Carlo 方法並記錄反衝能量損失，從而模擬理想狀態下的電子準彈性反射能譜。另外，我們也考慮電子束能量分佈、電子能譜測量儀器的能量解析度以及原子受熱能而振盪之三種效應對反彈能譜的影響，其最後結果與實驗值做出比較，並探討其中的差異。另外，電子的非彈性平均自由行徑，可以藉由對電子彈性波峰(electron elastic peak)的分析而得，我們根據自己的 Monte Carlo 方法，去分析 GaAs 的電子準彈性波峰，並藉由其而得出 GaAs 的非彈性電子平均自由行徑。

THE SIMULATION AND ANALYSIS OF QUASI-ELASTICALLY BACKSCATTERED ELECTRONS

Student : Yu-Chun Li

Advisor : Cheng-May Kwei

**Department of Electronics Engineering and Institute of Electronics
National Chiao Tung University**

ABSTRACT

In this thesis, the models dealing with the elastic interactions between a moving electron and a solid were described. The inelastic interactions between a moving electron and a solid were studied theoretically. Based on the elastic-scattering and inelastic-scattering models, the simulation and analysis of electrons backscattered from solids surfaces were made.

In the work for the elastic scattering, to calculate the elastic differential cross section (EDCS) of an electron moving in a solid, the applied non-relativistic and relativistic models with free-atom and solid-atom potentials were described. The results calculated using the non-relativistic and the relativistic models were compared. Through the EDCS, the elastic mean free path (EMFP) of the electron can be determined. Since compounds have been widely used in many studies, the methods adopted to determine the total elastic cross sections and total EMFPs for compounds were also described. The method for the calculation of the probability of an electron scattered by each element in a compound was further given. Moreover, the Rutherford-type recoil energy loss in elastic scattering was discussed.

In the aspect of inelastic scattering of electrons with solids, our purpose was to derive an inelastic-scattering model that was suitable for electrons incident into and escaping from solid surfaces in arbitrary moving directions. Based on the dielectric response theory, the induced electric field can be obtained by solving the Poisson equation. Through the induced electric field with the adoption of spherical coordinates in the momentum integration, stopping power, differential inverse inelastic mean free path (DIIMFP), inelastic mean free path (IMFP) and surface excitation parameter (SEP) can be determined. The spherical coordinates was adopted in the momentum integration to satisfy energy and momentum conservations completely. Using the extended dielectric functions in this derived model, the crossing-angle-dependent and energy-dependent DIIMFPs and IMFPs and SEPs were shown. It was found that the calculated results of SEPs followed a simple formula. The fitted values of parameters in the simple formula for solid surfaces of Au, Ag and Cu were also listed in tables. Due to the exclusion of retardation effect of the induced electric fields in this derived inelastic-scattering model, it is inadequate for high-speed electrons interacting with solids. Hence, we further constructed a model that can determine the stopping power, DIIMFP and IMFP for high-speed electrons moving parallel to solid surfaces by solving the Maxwell equation instead of Poisson equation in the dielectric response theory. The results calculated using the models without and with the retardation effect were shown and compared.

Applying the results of elastic and inelastic interactions of electrons with solids, the energy distribution of the elastic peak of electrons backscattered from solid surfaces can be simulated by recording the recoil energy loss in the Monte Carlo (MC) method. The effects of the energy distribution of the electron beam, the energy resolution of the spectrometer and the thermal motion of atoms in solids were also

included. Comparisons of the calculated energy spectra with the experimental data were also made. On the other hand, the electron effective IMFP can be extracted from the electron elastic peak. This method was also discussed in the present thesis.



ACKNOWLEDGEMENTS

I would like to express my sincere gratitude to my dissertation advisor, Prof. C. M. Kwei, for her guidance and encouragement during the course of the work. I would also like to appreciate Prof. C. J. Tung's corrections on my writings for publication. In addition, special thanks are given to the previous and present members working in Solid State Physics Development Laboratory for their reported results and theories of studies and for their valuable discussions and assistance.

This dissertation is dedicated to my family for their love.



CONTENTS

ABSTRACT (CHINESE)	i
ABSTRACT (ENGLISH)	iii
ACKNOWLEDGEMENTS	vi
CONTENTS	vii
TABLE CAPTIONS	x
FIGURE CAPTIONS	xi
CHAPTER 1 INTRODUCTION	1
1.1 Background	1
1.2 Elastic Scattering	1
1.3 Inelastic Scattering	3
1.4 Electron Quasi-elastic Peak	4
CHAPTER 2 ELASTIC SCATTERING	7
2.1 Elastic Differential Cross Section	7
2.2 Elastic Mean Free Path	12
2.3 Elastic Scattering Model for Compounds	14
2.3.1 Total Elastic Cross Section and Total Elastic Mean Free Path for a Compound Based On Elastic Cross Section	14
2.3.2 Total Elastic Cross Section and Total Elastic Mean Free Path for a Compound Based On Elastic Mean Free Path	16
2.3.3 Comparisons for Total Elastic Mean Free Paths between The Method Based On Elastic Cross Section and The Method Based On Elastic Mean Free Path	17
2.4 Energy Loss in Elastic Scattering	19

CHAPTER 3	INELASTIC SCATTERING	21
3.1	The Basic Knowledge	21
3.2	The Dielectric Response Theory	23
3.2.1	Induced potential	23
3.2.2	Stopping Power	28
3.2.3	Differential Inverse Inelastic Mean Free Path and Inelastic Mean Free Path	31
3.2.4	Differential Inverse Inelastic Mean Free Path and Inelastic Mean Free Path for an Electron Crossing a Solid Surface	32
3.3	Surface Excitation Parameter	43
3.4	The Inelastic-scattering Model with Retardation Effect	55
3.4.1	The Basic Knowledge	55
3.4.2	The Induced Vector and Scalar Potentials for Electrons Moving Parallel to an Interface	59
3.4.3	The Stopping Power and DIIMFP with Retardation Effect for Electrons Moving Parallel to an Interface	67
3.4.4	Comparisons between the Model without Retardation Effect and the Model with Retardation Effect for Electrons Moving Parallel to a Solid Surface	74
CHAPTER 4	ELECTRON QUASI-ELASTIC PEAK	80
4.1	Simulation for Energy Spectra of Electrons Quasi-elastically Backscattered from a Semi-infinite Solid	81
4.1.1	The Monte Carlo Method	81
4.1.2	The Results Calculated Using Monte Carlo method	86
4.1.3	Adjustments to Energy Spectra of Quasi-elastically Backscattered Electrons	91
4.1.4	Formula for Energy Spectra Contributed by Single-scattering Event	99
4.2	Elastic Reflection Coefficient	104

4.3	Elastic Reflection Coefficient for a Compound	104
4.3.1	The Monte Carlo Algorithm for a Compound	104
4.3.2	Using Elastic Reflection Coefficient to Determine Electron Inelastic Mean Free Path for a Compound	105
CHAPTER 5 SUMMARY		111
REFERENCES		113
VITA		117
PUBLICATION LIST		118



TABLE CAPTIONS

CHAPTER 3

Table 3.1 Fitted values of parameters a , b and c in Eq. (3.32) for escaping electrons

Table 3.2 Fitted values of parameters a , b and c in Eq. (3.32) for incident electrons



FIGURE CAPTIONS

CHAPTER 2

Fig. 2.1 Comparison of the angular dependence of the non-relativistic (solid curve) and the relativistic (dashed curve) EDCSs with solid-atom potentials for a 2000 eV electrons scattered by the Cu atom.

Fig. 2.2 Comparison of the angular dependence of the non-relativistic (solid curve) and the relativistic (dashed curve) EDCSs with solid-atom potentials for a 2000 eV electron scattered by the Au atom.

Fig. 2.3 The energy dependence of the relativistic EMFPs for Au calculated using the solid-atom potential.

Fig. 2.4 Comparison for the energy dependence of the relativistic total elastic mean free paths for GaAs calculated based on elastic cross section (solid curve) and based on elastic mean free path (dashed curve).

Fig. 2.5 A sketch of the Rutherford-type elastic interaction between an electron of mass m and an atom of mass M . θ is the polar scattering angle defined as the angel between the electron's moving directions before and after scattering. E and E_f are the energy of the electron before and after scattering, respectively.

CHAPTER 3

Fig. 3.1 A sketch of the problem studied in this work. An electron of velocity \bar{v} moves across the interface at time $t = 0$ from medium 1 of dielectric function $\varepsilon_1(\bar{q}, \omega)$ to medium 2 of dielectric function $\varepsilon_2(\bar{q}, \omega)$ with crossing angle α . The instant position of the electron is $\bar{r} = \bar{v}t$, relative to the crossing point at the interface.

Fig. 3.2 Calculated results of the DIIMFP in vacuum for a 500 eV escaping electron from Cu to vacuum with different crossing angles and distances from the crossing point at the surface.

Fig. 3.3 Calculated results of the DIIMFP in Cu for a 500 eV escaping electron from Cu to vacuum with different crossing angles and distances from the crossing point at the surface.

Fig. 3.4 Calculated results of the DIIMFP in vacuum for a 500 eV incident electron from vacuum to Cu with different crossing angles and distances from the crossing point at the surface.

Fig. 3.5 Calculated results of the DIIMFP in Cu for a 500 eV incident electron from vacuum to Cu with different crossing angles and distances from the crossing point at the surface.

Fig. 3.6 A plot of the inverse IMFP for a 500 eV escaping electron from Cu to vacuum with different crossing angles as a function of electron distance from the crossing point at the surface.

Fig. 3.7 A plot of the inverse IMFP for a 500 eV incident electron from vacuum to Cu with different crossing angles as a function of electron distance from the crossing point at the surface.

Fig. 3.8 A plot of the cross-angle-dependent SEPs calculated using Eq. (3.30) for the escaping electrons of 300 eV (solid circles), 500 eV (solid squares) and 800 eV (solid triangles) moving from Cu to vacuum. The corresponding fitted values obtained from Eq. (3.32) are displayed by solid curves.

Fig. 3.9 A plot of the cross-angle-dependent SEPs calculated using Eq. (3.31) for the incident electrons of 300 eV (solid circles), 500 eV (solid squares)

and 800 eV (solid triangles) moving from vacuum to Cu. The corresponding fitted values obtained from Eq. (3.32) are displayed by solid curves.

Fig. 3.10 A plot of SEPs versus energy calculated using Eq. (3.30) for electrons escaping from Cu by the crossing angle $\alpha = 0^0$ (solid triangles) and $\alpha = 50^0$ (solid circles). The corresponding fitted values obtained from Eq. (3.32) are displayed by solid curves.

Fig. 3.11 A plot of SEPs versus energy calculated using Eq. (3.31) for electrons incident into Cu by the crossing angle $\alpha = 0^0$ (solid triangles) and $\alpha = 50^0$ (solid circles). The corresponding fitted values obtained from Eq. (3.32) are displayed by solid curves.

Fig. 3.12 A plot of the SEP for a 500 eV escaping electron from Cu to vacuum as a function of crossing angle. Symbols are the calculated results using Eq. (3.30). Solid curve is the fitting results using Eq. (3.32). Corresponding data of Chen (2002) (dashed curve) and Oswald (1997) (dotted curve) are plotted for comparisons.

Fig. 3.13 A plot of the SEP for a 500 eV incident electron from vacuum to Cu as a function of crossing angle. Symbols are the calculated results using Eq. (3.31). Solid curve is the fitting results using Eq. (3.32). Corresponding data of Oswald (1997) (dotted curve) are plotted for comparisons.

Fig. 3.14 A plot of the SEP versus energy for an electron escaping from Cu to vacuum by $\alpha = 0^0$. Symbols are the calculated results using Eq. (3.30). Solid curve is the fitting results using Eq. (3.32). Corresponding data of Chen (2002) (dashed curve) and Oswald (1997)

(dotted curve) are plotted for comparisons.

Fig. 3.15 A plot of the SEP versus energy for an electron escaping from vacuum to Cu by $\alpha = 0^\circ$. Symbols are the calculated results using Eq. (3.31). Solid curve is the fitting results using Eq. (3.32). Corresponding data of Oswald (1997) (dotted curve) are plotted for comparisons.

Fig. 3.16 A sketch of an electron of charge e and speed v moving in positive x -direction and parallel to an interface (at $z = 0$) between medium 1 of dielectric function $\varepsilon_1(\vec{q}, \omega)$ (at $z < 0$) and medium 2 of dielectric function $\varepsilon_2(\vec{q}, \omega)$ (at $z > 0$). The permeabilities of medium 1 and medium 2 are equal to 1. The electron is located in medium 1 at a distance d from the interface, and its instant position at time t is expressed as $(vt, 0, -d)$.

Fig. 3.17 A comparison of the DIIMFPs without retardation effect (solid curve) and with retardation effect (dashed curve) for electrons of energy 1000 eV moving in vacuum at depth $z = -1 \text{ \AA}$ and parallel to a Cu surface.

Fig. 3.18 A comparison of the DIIMFPs without retardation effect (solid curve) and with retardation effect (dashed curve) for electrons of energy 10^6 eV moving in vacuum at depth $z = -1 \text{ \AA}$ and parallel to a Cu surface.

Fig. 3.19 A comparison of the IMFPs without retardation effect (solid curve) and with retardation effect (dashed curve) versus energy for electrons moving in vacuum at depth $z = -1 \text{ \AA}$ and parallel to a Cu surface.

Fig. 3.20 A comparison of the stopping powers without retardation effect (solid curve) and with retardation effect (dashed curve) versus energy for electrons moving in vacuum at depth $z = -1 \text{ \AA}$ and parallel to a Cu

surface.

CHAPTER 4

Fig. 4.1 A plot of the MC simulation results on the energy distribution of electrons quasi-elastically backscattered from Si for normally incident electrons of 5000 eV. Individual contributions from one, two, three and all elastic scatterings are plotted separately.

Fig. 4.2 A plot of the MC simulation results on the energy distribution of electrons quasi-elastically backscattered from Au for normally incident electrons of 5000 eV. Individual contributions from one, two, three and all elastic scatterings are plotted separately.

Fig. 4.3 A plot of the MC simulation results on the energy distribution of electrons quasi-elastically backscattered from Si and Au for normally incident electrons of 5000 eV. The left and right longitudinal axes are for Si and Au, respectively.

Fig. 4.4 A plot of the MC results on the energy spectra of electrons quasi-elastically backscattered from Si for normally incident electrons of 5000eV mean energy and 0.3 eV (solid curve) and 0.5 eV (dashed curv) FWHM.

Fig. 4.5 A plot of the MC results on the energy spectra of electrons quasi-elastically backscattered from Au for normally incident electrons of 5000eV mean energy and 0.3 eV (solid curve) and 0.5 eV (dashed curv) FWHM.

Fig. 4.6 A plot of the MC results on the energy spectra of electrons quasi-elastically backscattered from Si for normally incident electrons of 5000eV mean energy and 0.3 eV FWHM. The spectrometer resolutions

are 0 eV (solid curve), 0.3 eV (dashed curve) and 0.5 eV (dotted curve).

Fig. 4.7 A plot of the MC results on the energy spectra of electrons quasi-elastically backscattered from Au for normally incident electrons of 5000eV mean energy and 0.3 eV FWHM. The spectrometer resolutions are 0 eV (solid curve), 0.3 eV (dashed curve) and 0.5 eV (dotted curve).

Fig. 4.8 A plot of the MC simulation results on the energy spectra of electrons quasi-elastically backscattered from Si for normally incident electrons of 5000 eV mean energy and 0.4 eV FWHM. Here electrons are incident at an angle 50° ; acceptance angles are between 0° and 3° ; the spectrometer resolution is 0.28 eV. The thermal effect of atoms is neglected (solid curve) and considered (dash-dot) by applying the single scattering model (Varga *et al.* 2001) with a FWHM of $\Delta E_T = 0.3$ eV at the room temperature. For comparison, the experimental data (dashed curve) (Varga *et al.* 2001) are also included.

Fig. 4.9 A plot of MC results on the energy distribution of electrons quasi-elastically backscattered from Si for 5000 eV normally incident electrons suffering single elastic scattering inside the solid (solid curve). The dotted curve represents the results calculated by Eqs. (4.16) and (4.17).

Fig. 4.10 A plot of MC results on the energy distribution of electrons quasi-elastically backscattered from Au for 5000 eV normally incident electrons suffering single elastic scattering inside the solid (solid curve). The dotted curve represents the results calculated by Eqs. (4.16) and (4.17).

Fig. 4.11 The intensity ratio of electrons backscattered from GaAs to those from Ni for a 50° incident angle and $0^\circ - 90^\circ$ emission angles (solid circles) and for a 0° (normally) incident angle and $36.3^\circ - 48.3^\circ$ emission angles (solid triangles). Experimental data of Krawczyk *et al.* (1998) (open circles) and Zommer *et al.* (1998) (open triangles) are plotted for comparison.

Fig. 4.12 The intensity ratio of electrons backscattered from GaAs to those from Ni calculated using the depth-independent electron IMFP (abscissa). The solid and dashed curves are, respectively, for a 50° incident angle and $0^\circ - 90^\circ$ emission angles and for a 0° incident angle and $36.3^\circ - 48.3^\circ$ emission angles. The symbols are the corresponding results obtained by MC simulations using the depth-dependent electron IMFPs and SEPs.

Fig. 4.13 The effective IMFP as a function of electron energy for a 50° incident angle and $0^\circ - 90^\circ$ emission angles (solid circles) and for a 0° incident angle and $36.3^\circ - 48.3^\circ$ emission angles (solid triangles). Also plotted are experimental data of Krawczyk *et al.* (1998) (open circles) and Zommer *et al.* (open triangles), and calculated IMFPs for volume excitations (solid curve).

CHAPTER 1

INTRODUCTION

1.1 Background

The interactions between a moving electron and a solid include elastic and inelastic interactions. The elastic interaction occurs when the electron collides with an atom in the solid. This elastic collision changes the moving direction of the electron. The inelastic interaction indicates that the induced electric fields have influence on the motion of the electron, resulting in the losses of the electron's kinetic energy. Much work has been done on such two physical phenomena in many applications. For instance, in the interpretation of the elastic peak intensity measured by elastic peak electron spectroscopy (EPES) (Gergely 1981, 1983, 1986, 1987), elastic and inelastic scatterings of electrons with solids play important roles (Jablonski *et al.* 1989, 1991). Thus, to study solid state physics, the knowledge of the elastic and inelastic interactions is necessary. Note that the atomic units were adopted unless otherwise specified in our work.

1.2 Elastic Scattering

For the elastic interaction of electrons in solids, elastic differential cross section (EDCS) and elastic mean free path (EMFP) are the most important parameters. EDCS is a distribution of the angle between the electron's moving directions before and after elastic scattering. EMFP means the average path length of the electron

between two consecutive elastic-scattering events. EDCS and EMFP can be calculated using the non-relativistic model (Joachain 1975) and the relativistic model (Mott 1929). The non-relativistic model was derived through the Schrodinger wave equation with a potential, and the relativistic model was derived through the Dirac wave equation with a potential. In our present thesis, we adopted the relativistic model to calculate the EDCSs and EMFPs for electrons moving in solids since the relativistic EDCS and EMFP are more accurate for heavy atoms. The formula to calculate EDCS in this model was depicted in chapter 2. For comparison, the formula of the non-relativistic EDCS was also described. Further, we calculated the total elastic cross section and total EMFP for a compound based on elastic cross sections and EMFPs of the individual elements. Moreover, the elastic collision of an electron with an atom can be regarded as the Rutherford-type scattering. The Rutherford-type scattering causes the recoil energy loss in each elastic scattering event (Boersch *et al.* 1967). In the end of chapter 2, we added the discussion of the recoil energy loss for elastic scattering.

1.3 Inelastic Scattering

In the research for the inelastic interaction of low-energy electrons with solids, much attention has been paid to differential inverse inelastic mean free path (DIIMFP) and inelastic mean free path (IMFP). DIIMFP is the probability density function of the energy loss per unit path length of the electron, and IMFP means the average path length between two consecutive inelastic-scattering events. DIIMFP or IMFP contains the combined effects arisen from volume and surface plasmon excitations. Volume excitation occurs only in the interior of the solid, while surface excitation

extends a distance in the order of several angstroms on both sides of the surface. Inside the solid, the decrease in volume excitations near the surface is compensated by the increase in surface excitations; accordingly, the total DIIMFPs and IMFPs inside the solid are roughly equal to the corresponding values for electrons moving in the infinite solid (Chen and Kwei 1996; Kwei *et al.* 1998b). Outside the solid, only surface excitations characterize the inelastic scattering. To evaluate this surface effect in vacuum, the surface excitation parameter (SEP) was introduced (Kwei *et al.* 1998b). Previously, based on the dielectric response theory (Tung *et al.* 1994), Kwei *et al.* (1998b) used the developed extended Drude dielectric functions (Kwei *et al.* 1993) to calculate the depth-dependent DIIMFPs, the depth-dependent IMFPs and SEPs for electrons normally crossing through solid surfaces. In this model, the SEP for other crossing angle α was calculated by multiplying the results of SEP for normally crossing angle with $(\cos\alpha)^{-1}$ (Kwei *et al.* 1998b; Chen 2002). However, momentum transfer in cylindrical coordinates with no restriction on its normal component was adopted for performing the momentum integration in the model. The conservations of energy and momentum were not completely satisfied, and the derived DIIMFP and IMFP for volume excitations at large depths did not match the DIIMFP and IMFP in an infinite solid.

In chapter 3, a similar approach as that in the previous work (Chen and Kwei 1996; Kwei *et al.* 1998b) was followed to derive DIIMFP and IMFP and SEP for electrons incident into or escaping from solids. Spherical coordinates were employed in the momentum integration to satisfy the energy and momentum conservations (Kwei *et al.* 2003). The dependences of DIIMFP and IMFP on the crossing angle and the position of electrons were established based on the dielectric response theory. The angular and energy distributions of SEP were also investigated.

Calculated results of SEPs for copper were fitted to an analytical formula. A comparison was made for our calculated SEPs with those calculated using other models (Chen 2002; Oswald 1997). Moreover, we extended the constructed inelastic-scattering model to include the retardation effect (Jackson 1975) for high-speed electrons moving parallel to solid surfaces. The calculated results for the models without and with retardation effect were compared.

1.4 Electron Quasi-elastic Peak

In many applications of surface sensitive electron spectroscopies, it is important to analyze the elastic peak spectra of electrons backscattered from solid surfaces (Kirschner and Staib 1973, 1975). Some significant information could be extracted from this analysis. For instance, in the application of elastic peak electron spectroscopies (EPES), IMFP for electrons moving in solids can be determined (Gergely 1981; Jablonski 1985; Dolinski *et al.* 1988; Gruzza and Pariset 1991; Jardin *et al.* 1992; Beilschmidt *et al.* 1994). The elastic peak spectra can be characterized by the energy distributions. The energy distribution is due to the Rutherford-type recoil energy losses as electrons scattered elastically by atomic nuclei. These energy losses in elastic scattering events are indeed very small but not negligible (Erickson and Powell 1989), and result in a small energy shift and a width broadening in the elastic peak spectra. The elastic scattering associated with the slight recoil energy loss was alternatively called the quasi-elastic scattering (Erickson and Powell *et al.* 1989). These phenomena can be observed experimentally in the works with electron spectrometers (Boersch *et al.* 1967; Erickson and Powell 1989; Laser and Seah 1993; Goto and Shimizu 1997), especially for electrons backscattered from the solid

composed of the elements of low atomic number. The quantitative interpretations of experimental results for the energy distributions in elastic peaks were available based on the simple model of the single-electron single-target-atom collision, which was suggested by Boersch *et al.* (1967). However, quasi-elastically backscattered electrons would substantially arise from the sum of a few scatterings instead of one (Chen *et al.* 1995). Additionally, the single-scattering model cannot interpret the width broadening and the shape of the elastic peak. Thus, Monte Carlo (MC) simulation considering multiple scatterings has been utilized to compute the elastic reflection coefficient and the angular distribution of backscattered electrons (Chen *et al.* 1995; Jablonski *et al.* 1992; Kwei *et al.* 1999, 2001). Since the Rutherford-type recoil energy loss was ignored in these previous simulations, the energy shift and the width broadening of the elastic peak were not attainable.

The aim of our work in chapter 4 was to simulate the energy distribution of electrons quasi-elastically backscattered from solid surfaces. We considered the recoil energy loss in our MC simulations. The energy distributions of electrons quasi-elastically backscattered from solid surfaces were calculated. Computed results revealed the peak shift and the width broadening of the elastic peak. Based on the algorithm of MC method, we also derived an analytic formula of the energy distribution of the elastic peak for backscattered electrons suffering single elastic scattering in solids. The calculated results using this formula were compared by the results computed using MC method. In addition, according to some experimental studies (Boersch *et al.* 1967; J. Tóth *et al.* 1998; Gergely *et al.* 2001; Sulyok *et al.* 2001), the spectrometer energy resolution, the energy distribution of the primary electrons and the thermal motion of atoms can also contribute to the energy spectra of quasi-elastically-backscattered electrons (Boersch *et al.* 1967; Tóth *et al.* 1998; Gergely *et al.* 2001; Sulyok *et al.* 2001). The adjustments of the energy spectra of

backscattered electrons for these effects were made in our calculation.

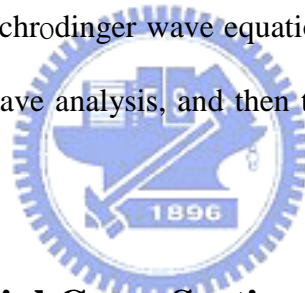
Through the electron elastic peaks, the effective IMFP for electrons moving in a solid can be extracted. In the final part of chapter 4, we discussed this method with the use of our MC simulation.



CHAPTER 2

ELASTIC SCATTERING

When an electron moves in a solid, the elastic interaction between the electron and the atoms in the solid will occur. Conventionally, the problem of elastic scattering was regarded as an electron suffering a potential with the scattering center at the atomic nucleus (Ohanian 1990). This technique simplified the complexity of the study on the elastic collision between electrons and solids. There are two wave equations that can describe the behavior of an electron affected by a potential. One is the non-relativistic Schrodinger wave equation, and the other is the relativistic Dirac wave equation. The Schrodinger wave equation and the Dirac wave equation can be solved using partial wave analysis, and then the elastic-scattering models for electrons can be carried out.



2.1 Elastic Differential Cross Section

In the research on elastic scattering, one is usually concerned about the direction of the electron after each scattering event. The scattering direction can be determined according to the elastic differential cross section (EDCS), $\frac{d\sigma_e}{d\Omega}$. EDCS is a distribution of the polar scattering angle which is defined as the angle between the electron's moving directions before and after each scattering event. Thus, the EDCS is the basic physical property in elastic scattering. There are two models can determine the EDCS. One is the non-relativistic model, and the other is the relativistic model. The non-relativistic model was derived using the Schrodinger wave equation with a potential, and the relativistic model was derived using the Dirac

wave equation with a potential. In the non-relativistic model, the formula of the non-relativistic EDCS with respect to the polar scattering angle θ is given by (Joachain 1975)

$$\frac{d\sigma_e}{d\Omega} = \frac{1}{4k^2} \left| \sum_{l=0}^{\infty} (2l+1) [\exp(2i\delta_l) - 1] P_l(\cos\theta) \right|^2, \quad (2.1)$$

where $k = \sqrt{2E}$, E is the kinetic energy of the incident electron, l is the orbital angular momentum quantum number, δ_l is the l th phase shift, $P_l(\cos\theta)$ is the Legendre polynomials of order l , σ_e is the elastic cross section, and $d\Omega = 2\pi \sin\theta d\theta$ is the differential solid angle in the direction of the scattered electron. On the other hand, the formula of the relativistic EDCS in the relativistic model is given by (Mott 1929; Kwei *et al.* 1998a)

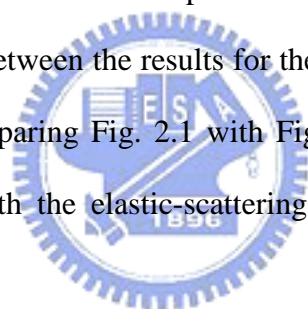
$$\begin{aligned} \frac{d\sigma_e}{d\Omega} = & \frac{1}{4K^2} \left| \sum_{l=0}^{\infty} \{ (l+1) [\exp(2i\delta_l^+) - 1] + l [\exp(2i\delta_l^-) - 1] \} P_l(\cos\theta) \right|^2, \\ & + \frac{1}{4K^2} \left| \sum_{l=1}^{\infty} [-\exp(2i\delta_l^+) + \exp(2i\delta_l^-)] P_l^1(\cos\theta) \right|^2, \end{aligned} \quad (2.2)$$

where $K = \frac{\sqrt{W^2 - c^4}}{c}$, W is the relativistic total energy, c is the speed of light, δ_l^\pm are the l th phase shifts for spin-up and spin-down states, and $P_l^1(\cos\theta)$ is the first-order Legendre polynomial.

To calculate the non-relativistic EDCS or the relativistic EDCS, the static potential that has influence on the elastic scattering interaction between the electron and the target atom in a solid must be calculated first. Two kinds of static potentials can be chosen. One is the free-atom potential, which means that the static potential

of the atom is distributed over the whole space. The other is the solid-atom potential, which means that the static potential of the atom is distributed within a limited range from the nucleus. After the static potential is determined, then the EDCS for an electron scattered by an atom in a solid can be obtained.

For a 2000 eV electron interacting elastically with a Cu atom, Fig. 2.1 shows the comparison of the non-relativistic EDCSs with the relativistic EDCSs. Here the results were calculated using the Hartree-Fock-Wigner-Seitz (HFWS) solid-atom static potential (Green and Leckey 1976; Tucker *et al.* 1969; Kwei 1984; Kwei *et al.* 1998a). In this figure, the difference between the non-relativistic and the relativistic EDCSs is slight. For Au, a similar comparison between the non-relativistic EDCS and the relativistic EDCS with HFWS static potentials was plotted in Fig. 2.2. It can be found that the difference between the results for the non-relativistic and relativistic models is obvious. By comparing Fig. 2.1 with Fig. 2.2, it is clear that using the relativistic model to deal with the elastic-scattering problem is more accurate for heavy atoms.



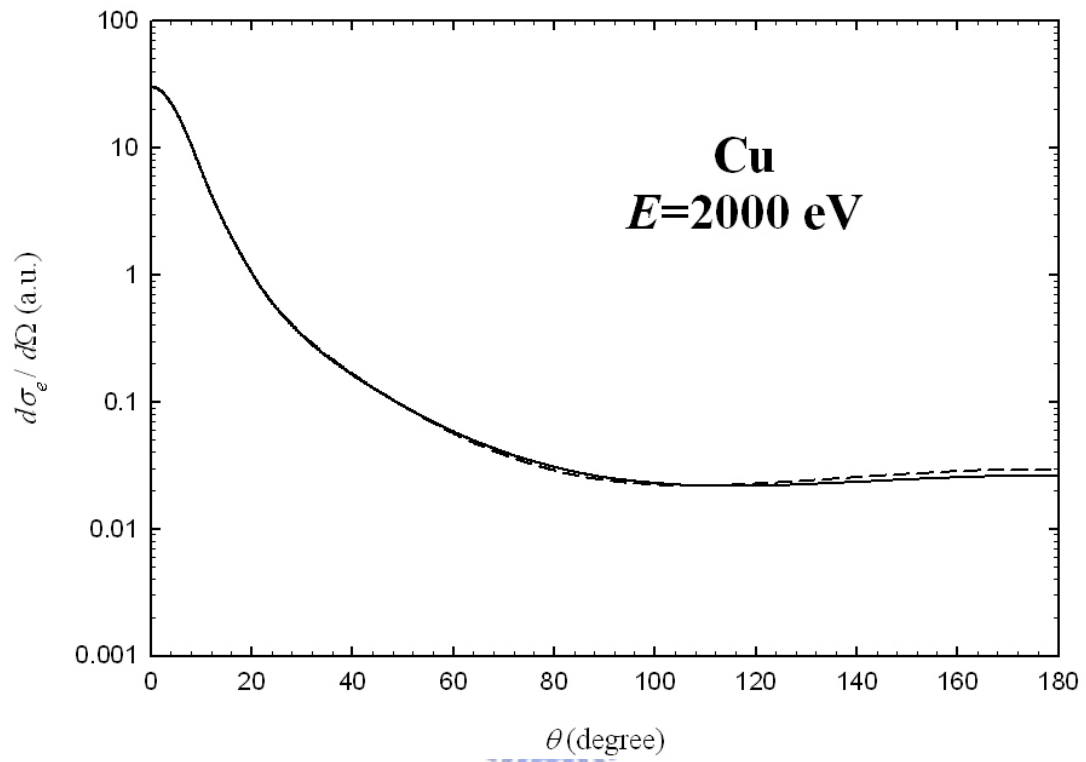


Fig. 2.1 Comparison of the angular dependence of the non-relativistic (solid curve) and the relativistic (dashed curve) EDCSs with solid-atom potentials for a 2000 eV electrons scattered by the Cu atom.

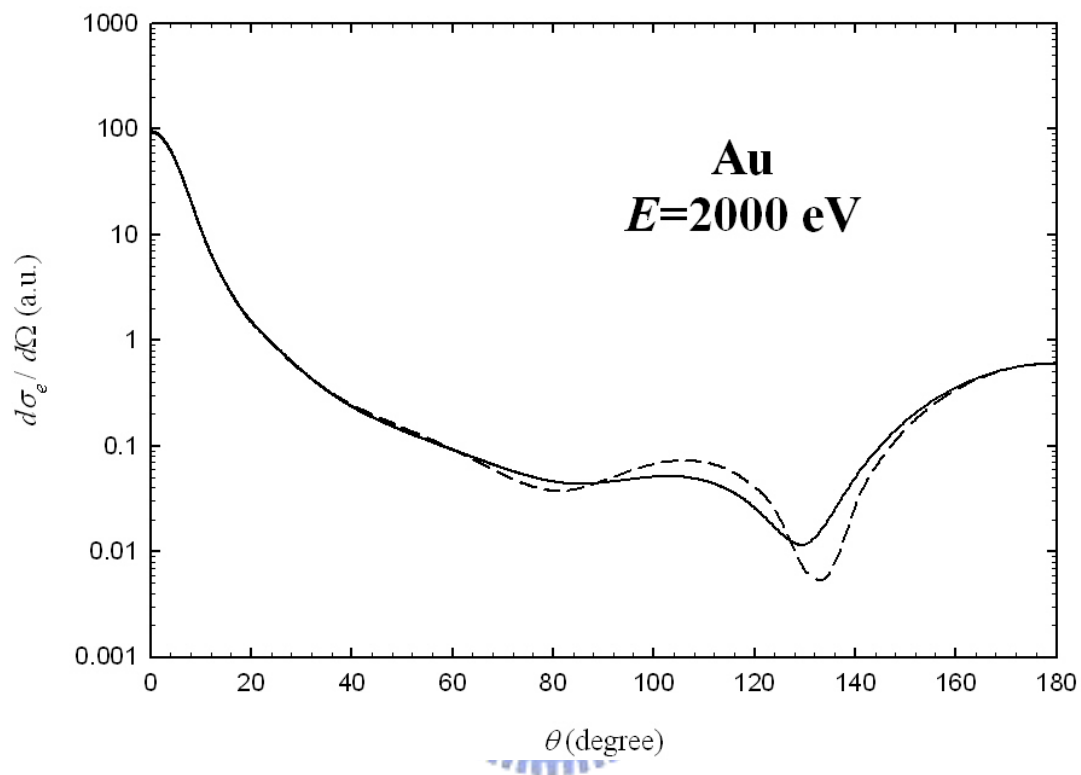


Fig. 2.2 Comparison of the angular dependence of the non-relativistic (solid curve) and the relativistic (dashed curve) EDCSs with solid-atom potentials for a 2000 eV electron scattered by the Au atom.

2.2 Elastic Mean Free Path

The EDCS has been used to indicate the distribution of the scattering angle θ after the electron being scattered by the target atom. Based on the EDCS, another important physical parameter for elastic scattering can be determined. Such parameter is elastic mean free path (EMFP), which means the average distance between two consecutive elastic scatterings. The EMFP $\lambda_e(E)$ of electrons moving in a condensed medium is defined as

$$\frac{1}{\lambda_e(E)} = N\sigma_e = N \int \left(\frac{d\sigma_e}{d\Omega} \right) d\Omega = 2\pi N \int_0^\pi \left(\frac{d\sigma_e}{d\Omega} \right) \sin\theta d\theta, \quad (2.3)$$

where N is the number of atoms per unit volume in the condensed medium. Due to $\frac{d\sigma_e}{d\Omega}$ is as a function of the electron moving energy E , λ_e is also in terms of E .

Figure 2.3 shows the relativistic EMFP as a function of the electron's energy calculated by employing the HFWS solid-atom static potentials for Au. It can be seen that EMFP increase with the increasing of the electron's energy. Higher energy implies faster speed. Then the probability of the faster electron colliding with the atom is smaller, which means that the faster electron experiences a longer path length before a collision. As a consequence, EMFP increase with the increasing of the electron's energy.

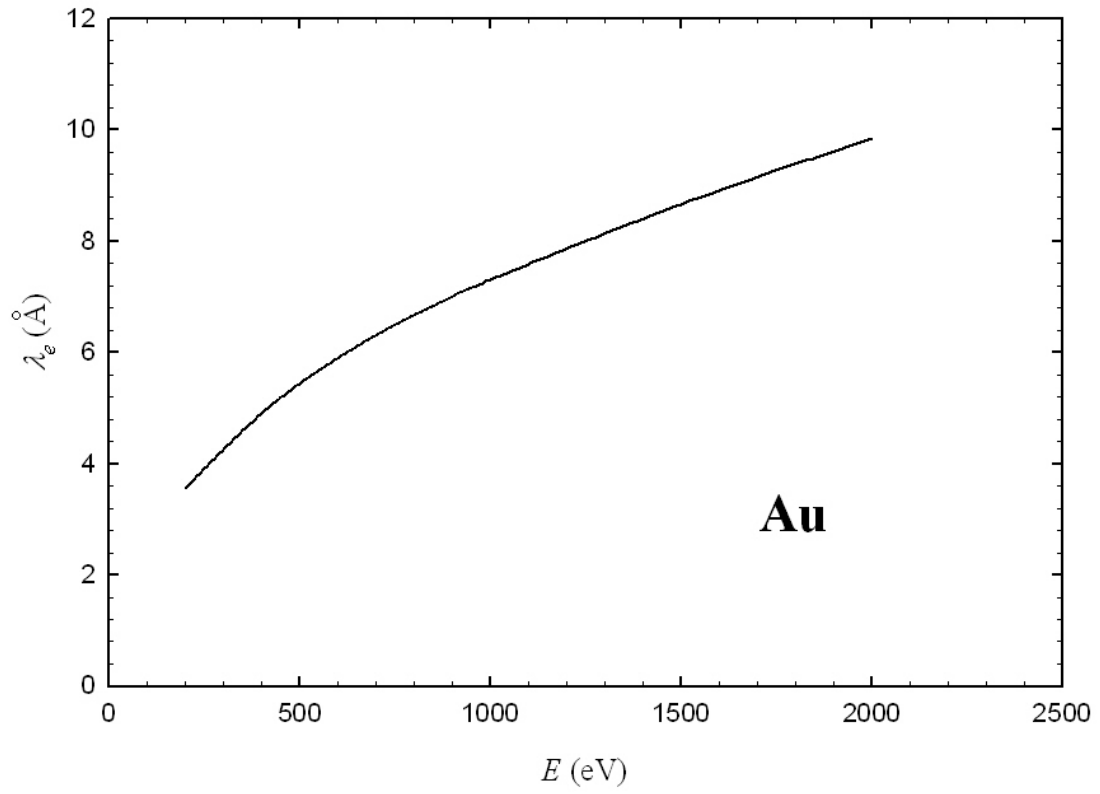


Fig. 2.3 The energy dependence of the relativistic EMFPs for Au calculated using the solid-atom potential.

2.3 Elastic Scattering Model for Compounds

So far, we have concentrated on the theoretical elastic scattering model for electrons interacting with the medium composed of one kind of elements. Much research has frequently been devoted to the interaction between electrons and compound mediums in the experiments of electron energy spectra (Krawczyk *et al.* 1998; Zommer *et al.* 1998; Lesiak *et al.* 1999; Gergely *et al.* 1999). The elastic scattering model for one-element medium is no longer suitable for the studies of compound mediums. Therefore, the elastic scattering model for compounds should be constructed. Two points of view have been proposed to establish the elastic scattering model for compounds. These two methods are depicted in the following two sections.

2.3.1 Total Elastic Cross Section and Total Elastic Mean Free Path for a Compound Based on Elastic Cross Section

Consider a compound medium composed of n kinds of elements. The total elastic cross section for the compound, $\sigma_{e,T}$, can be calculated from the sum of the fractions of the individual element elastic cross sections, $\sigma_{e,j}$, using the following formula (Herrmann and Reimer 1984; Gauvin *et al.* 1992; Murata *et al.* 1995):

$$\sigma_{e,T} = \sum_{j=1}^n a_j \sigma_{e,j} . \quad (2.4)$$

Here a_j is the atomic fraction, and defined by

$$a_j = \frac{N_j}{N}, \quad (2.5)$$

where N_j is the total number of the j th element per unit volume, and N denotes the total number of atoms per unit volume. According to Eqs. (2.3) and (2.4), the total EMFP $\lambda_{e,T}$ for a compound medium can be obtained by

$$\begin{aligned} \frac{1}{\lambda_{e,T}} &= N\sigma_{e,T} \\ &= \sum_{j=1}^n Na_j\sigma_{e,j} . \\ &= \sum_{j=1}^n N_j\sigma_{e,j} \end{aligned} \quad (2.6)$$

When the elastic scattering occurs in a compound, the EDCS is necessary for determining the electron moving direction after each scattering event. This can be done based on the probability that decides which element scatters the electron in each elastic scattering event. Using Eq. (2.4), the probability, $P_\sigma(j)$, for an electron being scattered by the j th element in a compound is given by (Howell and Boyde 1998)

$$P_{\sigma_e}(j) = \frac{a_j\sigma_{e,j}}{\sigma_{e,T}} . \quad (2.7)$$

By means of the expression (2.7), the scattering angle can be determined through the EDCS for electrons being scattered by the j th element in the compounds.

2.3.2 Total Elastic Cross Section and Total Elastic Mean Free Path for a Compound Based on Elastic Mean Free Path

On the other hand, the total EMFP, $\lambda_{e,T}$, for electrons moving in a compound can be determined from the sum of the fractions of the individual element EMFPs $\lambda_{e,j}$ according to the idea of the scattering probability, $\frac{1}{\lambda_e}$. Then the total EMFP is given by (Shimizu and Ding 1992; Ding and Shimizu 1996)

$$\frac{1}{\lambda_{e,T}} = \sum_{j=1}^n \frac{a_j}{\lambda_{e,j}}. \quad (2.8)$$

With the help of Eq. (2.3) and using Eq. (2.8), the total elastic cross section can be written as

$$\begin{aligned} \sigma_{e,T} &= \frac{1}{N\lambda_{e,T}} \\ &= \sum_{j=1}^n \frac{a_j}{N\lambda_{e,j}}. \end{aligned} \quad (2.9)$$

As mentioned in section 2.3.1, the selection of the elastic EDCS for each scattering event is according to which element is the scattering center. The probability $P_{\lambda}(j)$ of the electron being scattered by the j th element of the compound is given by (Howell and Boyde 1998)

$$P_{\lambda_e}(j) = \frac{a_j / \lambda_{e,j}}{1 / \lambda_{e,T}}. \quad (2.10)$$

This expression is the other probability to decide the scattering angle after the electron being scattered by the j th element in a compounds.

2.3.3 Comparisons for Total Elastic Mean Free Paths between The Method Based on Elastic Cross Section and The Method Based on Elastic Mean Free Path

Using Eqs. (2.6) and (2.8), the total EMFPs for electrons scattered in a medium composed of multiple components can be computed. Here we take a binary compound such as GaAs for the example. In this case, note that we used the Roothaan-Hartree-Fock free-atom potentials (Clementi and Roetti 1974) to calculate the relativistic EDCSs and EMFPs of the individual elements, i.e. Ga and As. Figure 2.4 shows the comparison between the elastic mean free path calculated through Eq. (2.6) (solid curve) and that calculated through Eq. (2.8) (dashed curve). We can see that the difference can be seen between the total EMFPs calculated using the method based on elastic cross section and the total EMFPs calculated using the method based on elastic mean free path.

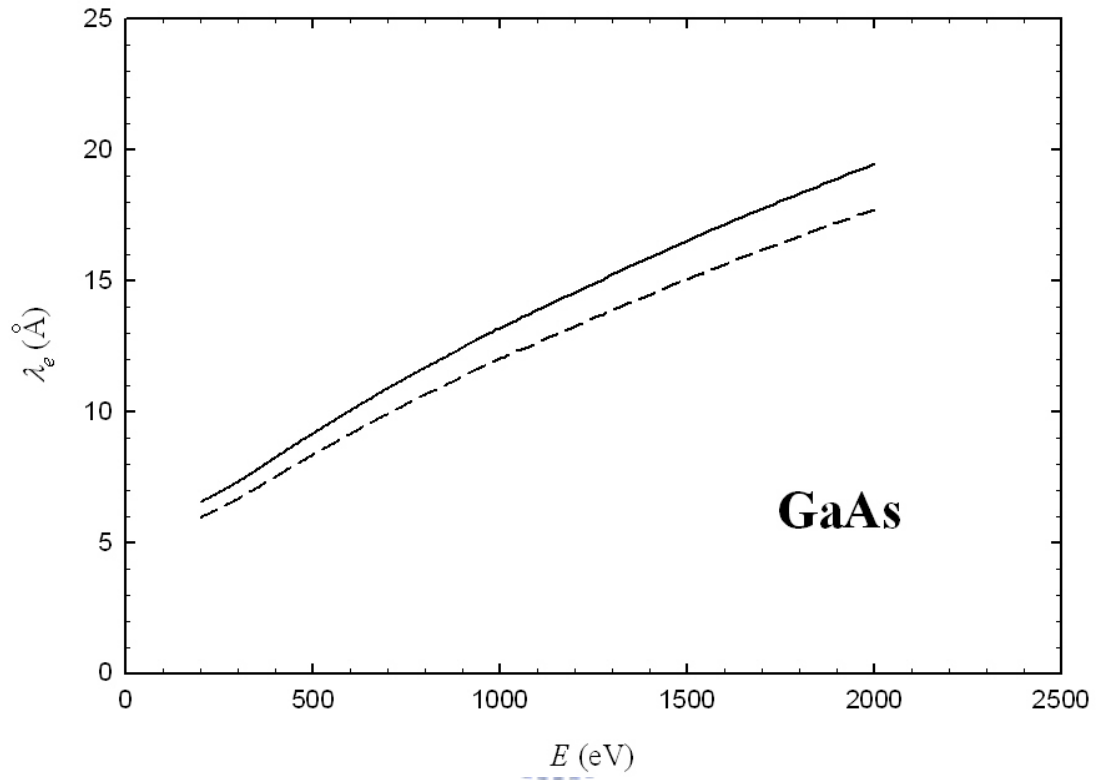


Fig. 2.4 Comparison for the energy dependence of the relativistic total elastic mean free paths for GaAs calculated based on elastic cross section (solid curve) and based on elastic mean free path (dashed curve).

2.4 Energy Loss in Elastic Scattering

While a moving electron colliding with one atom in a solid, the electron loses some energy. This effect is called the recoil effect. There were studies available on such energy transfer or energy loss of electrons in elastic scattering (Boersch *et al.* 1967; Erickson and Powell *et al.* 1989). This recoil effect can be regarded as the result of the classical Rutherford-type scattering between two charged particles. Hence, the remaining energy of the electron after scattering can be found by the conservations of energy and momentum.

The Rutherford-type elastic scattering between the electron and the atom is illustrated in Fig. 2.5. After an elastic scattering event, the energy loss of the electron, ΔE , is given by (Boersch *et al.* 1967)

$$\Delta E = \frac{4m}{M} E \sin^2 \frac{\theta}{2}, \quad (2.11)$$



where m and M are the masses of the electron and the atom, respectively. Thus, the remaining energy of the electron after scattering E_f can be obtained by

$$E_f = E - \Delta E = E \left(1 - \frac{4m}{M} \sin^2 \frac{\theta}{2} \right). \quad (2.12)$$

In Eq. (2.11), the recoil energy loss is slight due to the fact that $\frac{m}{M}$ is very small. The remaining energy of the electron is almost the same as its initial energy. Besides, the energy loss decreases with the increasing of the mass of the atom. Hence, the energy losses for heavy atoms are smaller.

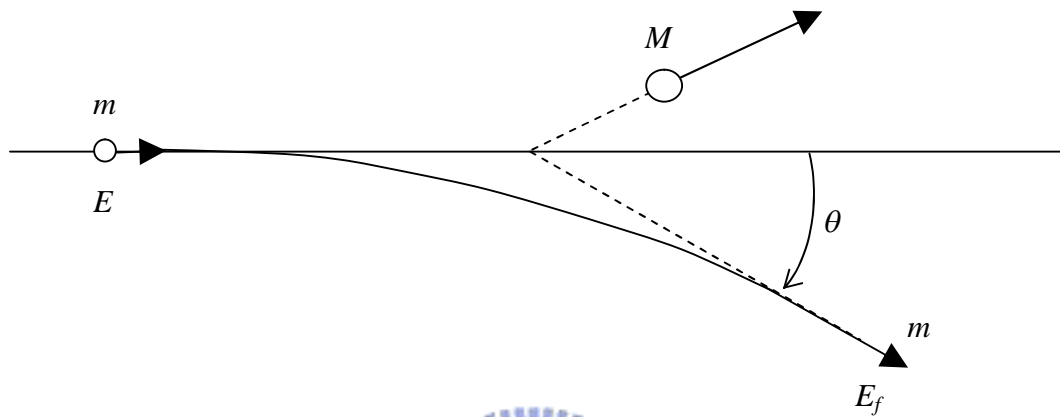


Fig. 2.5 A sketch of the Rutherford-type elastic interaction between an electron of mass m and an atom of mass M . θ is the polar scattering angle defined as the angle between the electron's moving directions before and after scattering. E and E_f are the energy of the electron before and after scattering, respectively.

CHAPTER 3

INELASTIC SCATTERING

In addition to the elastic interaction, inelastic interaction also occurs when an electron crossing an solid surface. Many theoretical (Tanuma *et al.* 1988, 1991a, 1991b; Chen and Kwei 1996; Kwei *et al.* 1998b, 1999, 2003) and experimental (Krawczyk *et al.* 1998; Zommer *et al.* 1998; Gergely *et al.* 1999; Lesiak *et al.* 1999; Tanuma *et al.* 2000) studies have been concerned about some properties of inelastic interaction between electrons and solids, such as stopping power, differential inverse inelastic mean free path (DIIMFP), inelastic mean free path (IMFP) and surface excitation parameter (SEP). In the theoretical approaches, these parameters were calculated based on the dielectric response theory with the use of the extended dielectric functions (Kwei *et al.* 1993). In this chapter, also by applying the dielectric response theory, we constructed a general model of inelastic scattering for electrons moving across solid surfaces. After that, the constructed model was further modified to include the retardation effect on the inelastic interaction for high-speed or high-energy electrons moving parallel to solid surfaces.

3.1 The Basic Knowledge

When a charged particle is located internal or external to a medium, significant interaction like fields and potentials is induced. Such interactions can be fully governed by Maxwell equations. The Maxwell equations for time-varying fields in the presence of matter are given by (Jackson 1975)

$$\nabla \cdot \vec{\mathbf{B}} = 0, \quad (3.1a)$$

$$\nabla \times \vec{\mathbf{E}} + \frac{1}{c} \frac{\partial \vec{\mathbf{B}}}{\partial t} = 0, \quad (3.1b)$$

$$\nabla \cdot \vec{\mathbf{D}} = 4\pi\rho, \quad (3.1c)$$

and

$$\nabla \times \vec{\mathbf{H}} - \frac{1}{c} \frac{\partial \vec{\mathbf{D}}}{\partial t} = \frac{4\pi}{c} \vec{\mathbf{J}}, \quad (3.1d)$$

where c is the speed of light. $\vec{\mathbf{E}}$ and $\vec{\mathbf{B}}$ are the electric field and the magnetic induction, respectively. $\vec{\mathbf{D}}$ and $\vec{\mathbf{H}}$ are the electric displacement and the magnetic field, respectively. ρ and $\vec{\mathbf{J}}$ are the charge density and the current density. The Fourier transform of Eq. (3.1c) is given by (Dressel and Grüner 2002)

$$i\vec{q} \cdot \vec{\mathbf{D}}(\vec{q}, \omega) = 4\pi\rho(\vec{q}, \omega), \quad (3.2)$$

where \vec{q} is the momentum transfer, and ω is the energy transfer, $\vec{\mathbf{D}}(\vec{q}, \omega) = \varepsilon(\vec{q}, \omega)\vec{\mathbf{E}}(\vec{q}, \omega)$, $\varepsilon(\vec{q}, \omega)$ is the dielectric function of the matter of interest, and $\vec{\mathbf{E}}(\vec{q}, \omega)$ and $\vec{\mathbf{D}}(\vec{q}, \omega)$ are the Fourier component of the electric field and the electric displacement, respectively. The Fourier components of the electric field $\vec{\mathbf{E}}(\vec{q}, \omega)$ can be related to the scalar potential $\Phi(\vec{q}, \omega)$ by (Dressel and Grüner 2002)

$$\vec{\mathbf{E}}(\vec{q}, \omega) = -i\vec{q}\Phi(\vec{q}, \omega). \quad (3.3)$$

By means of Eqs. (3.2) and (3.3), the Poisson equation for the scalar potential $\Phi(\vec{q}, \omega)$ in Fourier transformed form can be written as

$$q^2 \varepsilon(\vec{q}, \omega) \Phi(\vec{q}, \omega) = 4\pi \rho(\vec{q}, \omega). \quad (3.4)$$

In electrodynamics, we usually want to realize the fields or the potentials for mediums accompanied by boundary surfaces. To deal with this problem, the boundary conditions are necessary. Take consideration of an infinite plan boundary located at $z = 0$ between medium 1 and medium 2. Then the normal component of the electric displacement at the interface is continuous, and so are the tangential components of the electric field at the interface (Jackson 1975).

In our work, we used the Poisson equation shown in Eq. (3.4) to deal with the problem of the inelastic scattering for electrons of low and intermediate energies moving across an infinite interface. Again, the atomic units are used unless otherwise specified in this chapter.

3.2 The Dielectric Response Theory

3.2.1 Induced Potential

The problem to be solved is illustrated in Fig. 3.1, in which an electron of charge e and velocity \vec{v} moving obliquely across an interface (at time $t = 0$) from medium 1 of dielectric function $\varepsilon_1(\vec{q}, \omega)$ to medium 2 of dielectric function $\varepsilon_2(\vec{q}, \omega)$ by a crossing angle. The crossing angle α is defined as the angle between the interface normal and the electron moving direction, and $\vec{r} = \vec{v}t$ is the instant location of the electron relative to the crossing point at the interface. The charge density of the

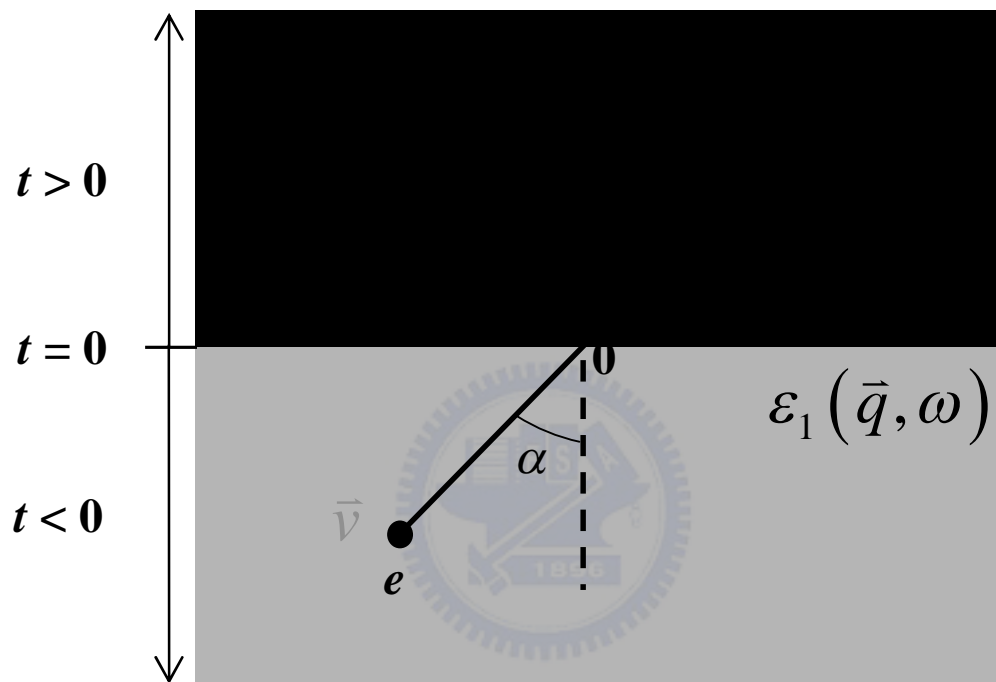


Fig. 3.1 A sketch of the problem studied in this work. An electron of velocity \bar{v} moves across the interface at time $t = 0$ from medium 1 of dielectric function $\epsilon_1(\vec{q}, \omega)$ to medium 2 of dielectric function $\epsilon_2(\vec{q}, \omega)$ with crossing angle α . The instant position of the electron is $\vec{r} = \bar{v}t$, relative to the crossing point at the interface.

electron $\rho_f(\vec{r}, t)$ is given by

$$\rho_f(\vec{r}, t) = -\delta(x - vt \sin \alpha) \delta(y) \delta(z - vt \cos \alpha). \quad (3.5)$$

The Fourier components of this electron charge density can be given by

$$\begin{aligned} \rho_f(\vec{q}, \omega) &= \int_{-\infty}^{\infty} \int_{-\infty}^{\infty} \rho_f(\vec{r}, t) \exp\{-i(\vec{q} \cdot \vec{r} - \omega t)\} dt d\vec{r} \\ &= -2\pi \delta(\omega - \vec{q} \cdot \vec{v}) \end{aligned} \quad (3.6)$$

To solve the boundary-value problem presented in Fig. 3.1, we applied the method of images (Jackson 1975). By introducing image charge densities on both sides of the interface, then the Fourier components of the scalar potentials in medium 1 and medium 2 can be determined from Poisson equation expressed in Eq. (3.4); that is,

$$\Phi_1(\vec{q}, \omega) = \frac{4\pi}{q^2 \varepsilon_1(\vec{q}, \omega)} [\rho_f(\vec{q}, \omega) + \rho_{s1}(\vec{Q}, \omega)], \quad \text{when } t < 0, \quad (3.7)$$

and

$$\Phi_2(\vec{q}, \omega) = \frac{4\pi}{q^2 \varepsilon_2(\vec{q}, \omega)} [\rho_f(\vec{q}, \omega) + \rho_{s2}(\vec{Q}, \omega)], \quad \text{when } t > 0, \quad (3.8)$$

where \vec{Q} is the parallel component of \vec{q} . $\rho_{s1}(\vec{Q}, \omega)$ and $\rho_{s2}(\vec{Q}, \omega)$ are the fictitious surface charge densities right on the surface facing to medium 2 and right on

the surface facing to medium 1, respectively. According to the boundary conditions, the fictitious surface charge densities be carried out by

$$\rho_{s1}(\vec{Q}, \omega) = -\rho_{s2}(\vec{Q}, \omega) = -2\pi \frac{\int_{-\infty}^{\infty} \frac{\delta(\omega - \vec{q} \cdot \vec{v})}{q^2} \left[\frac{1}{\varepsilon_2(\vec{q}, \omega)} - \frac{1}{\varepsilon_1(\vec{q}, \omega)} \right] dq_z}{\int_{-\infty}^{\infty} \frac{1}{q^2} \left[\frac{1}{\varepsilon_2(\vec{q}, \omega)} + \frac{1}{\varepsilon_1(\vec{q}, \omega)} \right] dq_z}. \quad (3.9)$$

By inserting Eqs. (3.6) and (3.9) into Eqs. (3.7) and (3.8), then the Fourier components of scalar potentials, $\phi^{(1)}(\vec{q}, \omega)$ and $\phi^{(2)}(\vec{q}, \omega)$, on either side of the interface are performed.

After that, we need to determine the induced scalar potentials before the later derivation of our model for inelastic scattering. The induced scalar potential on either side is defined as the scalar potential on either side removing the scalar potential for electrons moving in vacuum. The Fourier component of the scalar potential for electrons moving in vacuum can be calculated by letting $\varepsilon(\vec{q}, \omega) = 1$ in Eq. (3.4), i.e.

$$\Phi_{ref}(\vec{q}, \omega) = \frac{4\pi}{q^2} \rho_f(\vec{q}, \omega), \quad (3.10)$$

Consequently, the Fourier components of the induced scalar potentials in medium 1 and medium 2 can be given by, respectively,

$$\Phi_{ind,1}(\vec{q}, \omega) = \frac{-8\pi^2}{q^2} \left[\frac{1}{\varepsilon_1(\vec{q}, \omega)} - 1 \right] \delta(\omega - \vec{q} \cdot \vec{v}) + \frac{-8\pi^2}{q^2} \frac{1}{\varepsilon_1(\vec{q}, \omega)} \frac{\int_{-\infty}^{\infty} \frac{\delta(\omega - \vec{q} \cdot \vec{v})}{q^2} \left[\frac{1}{\varepsilon_2(\vec{q}, \omega)} - \frac{1}{\varepsilon_1(\vec{q}, \omega)} \right] dq_z}{\int_{-\infty}^{\infty} \frac{1}{q^2} \left[\frac{1}{\varepsilon_2(\vec{q}, \omega)} + \frac{1}{\varepsilon_1(\vec{q}, \omega)} \right] dq_z}, \quad (3.11)$$

and

$$\Phi_{ind,2}(\vec{q}, \omega) = \frac{-8\pi^2}{q^2} \left[\frac{1}{\varepsilon_2(\vec{q}, \omega)} - 1 \right] \delta(\omega - \vec{q} \cdot \vec{v}) - \frac{-8\pi^2}{q^2} \frac{1}{\varepsilon_2(\vec{q}, \omega)} \frac{\int_{-\infty}^{\infty} \frac{\delta(\omega - \vec{q} \cdot \vec{v})}{q^2} \left[\frac{1}{\varepsilon_2(\vec{q}, \omega)} - \frac{1}{\varepsilon_1(\vec{q}, \omega)} \right] dq_z}{\int_{-\infty}^{\infty} \frac{1}{q^2} \left[\frac{1}{\varepsilon_2(\vec{q}, \omega)} + \frac{1}{\varepsilon_1(\vec{q}, \omega)} \right] dq_z}. \quad (3.12)$$

The first terms in Eqs. (3.11) and (3.12) denote the induced scalar potentials for electrons moving in an infinite solid, which means that the momentum transfer \vec{q} is cylindrical symmetric with respect to the moving direction of the electron, i.e. the direction of \vec{v} . Accordingly, the term $\delta(\omega - \vec{q} \cdot \vec{v})$ in the first term can be converted into $\delta(\omega - qv\cos\beta)$, where β is the angle between \vec{q} and \vec{v} . Besides, we apply the assumption of $\varepsilon(\vec{q}, \omega) \approx \varepsilon(\vec{Q}, \omega)$ (Yubero and Tougaard 1992; Yubero *et al.* 1996) in the second terms of Eqs. (3.11) and (3.12) for the integration with respect to dq_z . Then the second terms in Eqs. (3.11) and (3.12) can be further performed by

$$\frac{-8\pi}{q^2} \frac{Qv_{\perp}}{(\omega - \vec{Q} \cdot \vec{v}_{\parallel})^2 + Q^2 v_{\perp}^2} \frac{\varepsilon_1(\vec{Q}, \omega) - \varepsilon_2(\vec{Q}, \omega)}{\varepsilon_j(\vec{Q}, \omega) [\varepsilon_1(\vec{Q}, \omega) + \varepsilon_2(\vec{Q}, \omega)]}, \quad \text{for } j = 1 \text{ and } 2, \quad (3.13)$$

where v_{\perp} and v_{\parallel} are the normal and parallel components of \vec{v} with respect to the plane boundary, respectively. After the above mentioned transformations for the first and second terms in Eqs. (3.11) and (3.12), the induced potentials in real space in medium 1 and 2 can be presented by means of the inverse Fourier transforms for Eqs. (3.11) and (3.12). That is,

$$\begin{aligned}
\Phi_{ind,1}(\vec{r},t) = & -\frac{1}{\pi} \iiint \delta(\omega - qv\cos\beta) \left[\frac{1}{\varepsilon_1(\vec{q},\omega)} - 1 \right] e^{i(qv\cos\beta - \omega t)} \sin\beta d\beta dq d\omega \\
& - \frac{1}{2\pi^2} \iiint \frac{1}{q^2} \frac{Qv_{\perp}}{(\omega - \vec{Q} \cdot \vec{v}_{\parallel})^2 + Q^2v_{\perp}^2} \frac{\varepsilon_1(\vec{Q},\omega) - \varepsilon_2(\vec{Q},\omega)}{\varepsilon_1(\vec{Q},\omega)[\varepsilon_1(\vec{Q},\omega) + \varepsilon_2(\vec{Q},\omega)]} \\
& \times \exp[i(\vec{Q} \cdot \vec{R} - \omega t)] \exp(iq_z z) \sin\theta d\phi d\theta dq d\omega, \\
& \text{when } t < 0, \tag{3.14}
\end{aligned}$$

and

$$\begin{aligned}
\Phi_{ind,2}(\vec{r},t) = & -\frac{1}{\pi} \iiint \delta(\omega - qv\cos\beta) \left[\frac{1}{\varepsilon_2(\vec{q},\omega)} - 1 \right] e^{i(qv\cos\beta - \omega t)} \sin\beta d\beta dq d\omega \\
& + \frac{1}{2\pi^2} \iiint \frac{1}{q^2} \frac{Qv_{\perp}}{(\omega - \vec{Q} \cdot \vec{v}_{\parallel})^2 + Q^2v_{\perp}^2} \frac{\varepsilon_1(\vec{Q},\omega) - \varepsilon_2(\vec{Q},\omega)}{\varepsilon_2(\vec{Q},\omega)[\varepsilon_1(\vec{Q},\omega) + \varepsilon_2(\vec{Q},\omega)]} \\
& \times \exp[i(\vec{Q} \cdot \vec{R} - \omega t)] \exp(iq_z z) \sin\theta d\phi d\theta dq d\omega, \\
& \text{when } t > 0, \tag{3.15}
\end{aligned}$$

where R and z are the parallel and the normal components of r with respect to the plane boundary. Note that here we use the spherical coordinates for the integration of momentum transfer q in Eqs. (3.14) and (3.15).

3.2.2 Stopping Power

The stopping power means the average energy loss per unit path length of a charged particle. It is the basic physical parameter for the study of the inelastic interaction between electrons and solids. The stopping power $-\frac{dW}{ds}$ of the electron can be related to the induced potential $\phi_{ind}(\vec{r},t)$ as (Flores and García-Moliner 1979)

$$-\frac{dW}{ds} = \frac{1}{v} \left[\frac{\partial \phi_{ind}(\vec{r}, t)}{\partial t} \right]_{\vec{r}=\vec{v}t}, \quad (3.16)$$

where the derivative of $\phi_{ind}(\vec{r}, t)$ is evaluated at the electron's position $\vec{r} = \vec{v}t$. By inserting Eqs. (3.14) and (3.15) into Eq. (3.16), then the stopping powers for electrons moving in medium 1 and medium 2 can be obtained by

$$\begin{aligned} -\frac{dW_1}{ds} = & \frac{i}{v\pi} \iiint \omega \delta(\omega - qv \cos \beta) \left[\frac{1}{\varepsilon_1(\vec{q}, \omega)} - 1 \right] e^{i(qvt \cos \beta - \omega t)} \sin \beta d\beta dq d\omega \\ & + \frac{i}{2v\pi^2} \iiint \frac{\omega}{q^2} \frac{Qv_{\perp}}{(\omega - \vec{Q} \cdot \vec{v}_{\parallel})^2 + Q^2 v_{\perp}^2} \frac{\varepsilon_1(\vec{Q}, \omega) - \varepsilon_2(\vec{Q}, \omega)}{\varepsilon_1(\vec{Q}, \omega) [\varepsilon_1(\vec{Q}, \omega) + \varepsilon_2(\vec{Q}, \omega)]} \\ & \times \exp[i(\vec{Q} \cdot \vec{R} - \omega t)] \exp(iq_z z) \sin \theta d\theta d\phi dq d\omega, \\ & \text{when } t < 0, \end{aligned} \quad (3.17)$$

and

$$\begin{aligned} -\frac{dW_2}{ds} = & \frac{i}{v\pi} \iiint \omega \delta(\omega - qv \cos \beta) \left[\frac{1}{\varepsilon_2(\vec{q}, \omega)} - 1 \right] e^{i(qvt \cos \beta - \omega t)} \sin \beta d\beta dq d\omega \\ & - \frac{i}{2v\pi^2} \iiint \frac{\omega}{q^2} \frac{Qv_{\perp}}{(\omega - \vec{Q} \cdot \vec{v}_{\parallel})^2 + Q^2 v_{\perp}^2} \frac{\varepsilon_1(\vec{Q}, \omega) - \varepsilon_2(\vec{Q}, \omega)}{\varepsilon_2(\vec{Q}, \omega) [\varepsilon_1(\vec{Q}, \omega) + \varepsilon_2(\vec{Q}, \omega)]} \\ & \times \exp[i(\vec{Q} \cdot \vec{R} - \omega t)] \exp(iq_z z) \sin \theta d\theta d\phi dq d\omega. \\ & \text{when } t > 0. \end{aligned} \quad (3.18)$$

For the integration over the energy loss ω in the second integrals of Eqs. (3.17) and (3.18), the contour integration is closed in the upper half plane (UHP) and the lower half plane (LHP) for $t < 0$ and $t > 0$, respectively. Meanwhile, in order to calculate the contour integration in the LHP in Eq. (3.18), it is convenient to convert the integration into the UHP due to the dielectric function is an analytic function of ω only in the UHP. In consequence, $\exp[i(\vec{Q} \cdot \vec{R} - \omega t)]$ in Eq. (3.18) can be

replaced according to $\exp[i(\bar{Q} \cdot R - \omega t)] = 2\cos(\omega t - \bar{Q} \cdot R) - \exp[-i(\bar{Q} \cdot R - \omega t)]$.

After that, the stopping powers in medium 1 and 2 can be further obtained by

$$\begin{aligned}
-\frac{dW_1}{ds} &= \frac{2}{\pi v^2} \int_{\omega=0}^E \omega d\omega \int_{q_-}^{q_+} dq \frac{1}{q} \operatorname{Im} \left[\frac{-1}{\varepsilon_1(\bar{q}, \omega)} \right] \\
&\quad - \frac{2\cos\alpha}{\pi^3} \int_{\omega=0}^E \omega d\omega \int_{q_-}^{q_+} dq \int_{\theta=0}^{\pi/2} d\theta \int_{\phi=0}^{2\pi} d\phi \frac{q \sin^2 \theta \cos(q_z r \cos\alpha) \exp(-|r|Q \cos\alpha)}{\tilde{\omega}^2 + Q^2 v_{\perp}^2} \\
&\quad \times \operatorname{Im} \left\{ \frac{\varepsilon_1(\bar{Q}, \omega) - \varepsilon_2(\bar{Q}, \omega)}{\varepsilon_1(\bar{Q}, \omega) [\varepsilon_1(\bar{Q}, \omega) + \varepsilon_2(\bar{Q}, \omega)]} \right\} \Theta(-r), \tag{3.19}
\end{aligned}$$

and

$$\begin{aligned}
-\frac{dW_2}{ds} &= \frac{2}{\pi v^2} \int_{\omega=0}^E \omega d\omega \int_{q_-}^{q_+} dq \frac{1}{q} \operatorname{Im} \left[\frac{-1}{\varepsilon_2(\bar{q}, \omega)} \right] \\
&\quad + \frac{2\cos\alpha}{\pi^3} \int_{\omega=0}^E \omega d\omega \int_{q_-}^{q_+} dq \int_{\theta=0}^{\pi/2} d\theta \int_{\phi=0}^{2\pi} d\phi \frac{q \sin^2 \theta \exp(-|r|Q \cos\alpha)}{\tilde{\omega}^2 + Q^2 v_{\perp}^2} \\
&\quad \times \left[2\cos\left(\frac{\tilde{\omega}r}{v}\right) - \exp(-|r|Q \cos\alpha) \right] \operatorname{Im} \left\{ \frac{\varepsilon_1(\bar{Q}, \omega) - \varepsilon_2(\bar{Q}, \omega)}{\varepsilon_2(\bar{Q}, \omega) [\varepsilon_1(\bar{Q}, \omega) + \varepsilon_2(\bar{Q}, \omega)]} \right\} \Theta(r), \tag{3.20}
\end{aligned}$$

where $\tilde{\omega} = \omega - qv \sin\theta \cos\phi \sin\alpha$, $Q = q \sin\theta$, $q_z = q \cos\theta$, $v_{\perp} = v \cos\alpha$, $E = \frac{v^2}{2}$,

and $\Theta(r)$ is the Heaviside step function. By applying the conservations of energy and momentum, the upper and the lower limits of q are given by

$$q_{\pm} = \sqrt{2E} \pm \sqrt{2(E - \omega)}. \tag{3.21}$$

3.2.3 Differential Inverse Inelastic Mean Free Path and Inelastic Mean Free Path

The DIIMFP is an important physical parameter for the inelastic interaction between electrons and mediums, and indicates the probability density for an electron losing energy ω as moving along a unit path length. The DIIMFP for an electron of energy E can be determined from the stopping power using the following relation:

$$-\frac{dW}{ds} = \int_0^E \omega u(\alpha, E, \omega, r) d\omega, \quad (3.22)$$

where we can see that the DIIMFP $u(\alpha, E, \omega, r)$ is as a function of the electron crossing angle α and the distance r of the electron relative to the crossing point at the interface. By comparing Eqs. (3.19) and (3.20) to Eq. (3.22), the DIIMFPs for electrons moving in medium 1 and medium 2 can be obtained by, respectively,

$$\begin{aligned} u_1(\alpha, E, \omega, r) = & \frac{2}{\pi v^2} \int_{q_-}^{q_+} dq \frac{1}{q} \operatorname{Im} \left[\frac{-1}{\varepsilon_1(\bar{q}, \omega)} \right] \\ & - \frac{2 \cos \alpha}{\pi^3} \int_{q_-}^{q_+} dq \int_{\theta=0}^{\pi/2} d\theta \int_{\phi=0}^{2\pi} d\phi \frac{q \sin^2 \theta \cos(q_z r \cos \alpha) \exp(r Q \cos \alpha)}{\tilde{\omega}^2 + Q^2 v_{\perp}^2} \\ & \times \operatorname{Im} \left\{ \frac{\varepsilon_1(\bar{Q}, \omega) - \varepsilon_2(\bar{Q}, \omega)}{\varepsilon_1(\bar{Q}, \omega) [\varepsilon_1(\bar{Q}, \omega) + \varepsilon_2(\bar{Q}, \omega)]} \right\} \Theta(-r), \end{aligned} \quad (3.23)$$

and

$$\begin{aligned}
u_2(\alpha, E, \omega, r) = & \frac{2}{\pi v^2} \int_{q_-}^{q_+} dq \frac{1}{q} \operatorname{Im} \left[\frac{-1}{\varepsilon_2(\bar{q}, \omega)} \right] \\
& + \frac{2 \cos \alpha}{\pi^3} \int_{q_-}^{q_+} dq \int_{\theta=0}^{\pi/2} d\theta \int_{\phi=0}^{2\pi} d\phi \frac{q \sin^2 \theta \exp(-rQ \cos \alpha)}{\tilde{\omega}^2 + Q^2 v_{\perp}^2} \\
& \times \left[2 \cos \left(\frac{\tilde{\omega} r}{v} \right) - \exp(-rQ \cos \alpha) \right] \operatorname{Im} \left\{ \frac{\varepsilon_1(\bar{Q}, \omega) - \varepsilon_2(\bar{Q}, \omega)}{\varepsilon_2(\bar{Q}, \omega) [\varepsilon_1(\bar{Q}, \omega) + \varepsilon_2(\bar{Q}, \omega)]} \right\} \Theta(r).
\end{aligned} \tag{3.24}$$

Another important physical parameter is IMFP, which can be derived by the integration of DIIMFP over all energy losses, that is,

$$\frac{1}{\lambda_i(\alpha, E, r)} = \int_0^E u(\alpha, E, \omega, r) d\omega, \tag{3.25}$$

where $\lambda_i(\alpha, E, r)$ is the IMFP. By inserting Eqs. (3.23) and (3.24) into Eq. (3.25), then the IMFPs for electrons moving in medium 1 and medium 2 can be determined.

3.2.4 Differential Inverse Inelastic Mean Free Path and Inelastic Mean Free Path for an Electron Crossing a Solid Surface

For the case of an electron emitted from a solid to vacuum (i.e. $s \rightarrow v$), let $\varepsilon_1(\bar{q}, \omega)$ and $\varepsilon_2(\bar{q}, \omega)$ in Eqs. (3.23) and (3.24) be replaced by $\varepsilon(\bar{q}, \omega)$ and 1, respectively. Then the electron DIIMFP in this case is given by

$$\begin{aligned}
u^{s \rightarrow v}(\alpha, E, \omega, r) = & \\
& \frac{2}{\pi v^2} \int_{q_-}^{q_+} dq \frac{1}{q} \operatorname{Im} \left(\frac{-1}{\varepsilon(q, \omega)} \right) \Theta(-r) \\
& - \frac{2 \cos \alpha}{\pi^3} \int_{q_-}^{q_+} dq \int_0^{\pi/2} d\theta \int_0^{2\pi} d\phi \frac{q \sin^2 \theta \cos(q_z r \cos \alpha) \exp(-|r|Q \cos \alpha)}{\tilde{\omega}^2 + Q^2 v_{\perp}^2} \operatorname{Im} \left(\frac{-1}{\varepsilon(Q, \omega)} \right) \Theta(-r) \\
& + \frac{4 \cos \alpha}{\pi^3} \int_{q_-}^{q_+} dq \int_0^{\pi/2} d\theta \int_0^{2\pi} d\phi \frac{q \sin^2 \theta \cos(q_z r \cos \alpha) \exp(-|r|Q \cos \alpha)}{\tilde{\omega}^2 + Q^2 v_{\perp}^2} \operatorname{Im} \left(\frac{-1}{\varepsilon(Q, \omega) + 1} \right) \Theta(-r) \\
& + \frac{4 \cos \alpha}{\pi^3} \int_{q_-}^{q_+} dq \int_0^{\pi/2} d\theta \int_0^{2\pi} d\phi \frac{q \sin^2 \theta \exp(-|r|Q \cos \alpha)}{\tilde{\omega}^2 + Q^2 v_{\perp}^2} \operatorname{Im} \left(\frac{-1}{\varepsilon(Q, \omega) + 1} \right) \\
& \quad \times \left[2 \cos \left(\frac{\tilde{\omega} r}{v} \right) - \exp(-|r|Q \cos \alpha) \right] \Theta(r)
\end{aligned} \tag{3.26}$$

A similar calculation can be performed for the case of electrons entering a semi-infinite solid by taking $\varepsilon_1(\vec{q}, \omega) = 1$ and $\varepsilon_2(\vec{q}, \omega) = \varepsilon(\vec{q}, \omega)$ in Eqs. (3.23) and (3.24). Then the DIIMFP for incident electrons (i.e. $v \rightarrow s$) is given by

$$\begin{aligned}
u^{v \rightarrow s}(\alpha, E, \omega, r) = & \\
& \frac{4 \cos \alpha}{\pi^3} \int_{q_-}^{q_+} dq \int_0^{\pi/2} d\theta \int_0^{2\pi} d\phi \frac{q \sin^2 \theta \cos(q_z r \cos \alpha) \exp(-|r|Q \cos \alpha)}{\tilde{\omega}^2 + Q^2 v_{\perp}^2} \operatorname{Im} \left(\frac{-1}{\varepsilon(Q, \omega) + 1} \right) \Theta(-r) \\
& + \frac{2}{\pi v^2} \int_{q_-}^{q_+} dq \frac{1}{q} \operatorname{Im} \left(\frac{-1}{\varepsilon(q, \omega)} \right) \Theta(r) \\
& - \frac{2 \cos \alpha}{\pi^3} \int_{q_-}^{q_+} dq \int_0^{\pi/2} d\theta \int_0^{2\pi} d\phi \frac{q \sin^2 \theta \exp(-|r|Q \cos \alpha)}{\tilde{\omega}^2 + Q^2 v_{\perp}^2} \operatorname{Im} \left(\frac{-1}{\varepsilon(Q, \omega)} \right) \\
& \quad \times \left[2 \cos \left(\frac{\tilde{\omega} r}{v} \right) - \exp(-|r|Q \cos \alpha) \right] \Theta(r) \\
& + \frac{4 \cos \alpha}{\pi^3} \int_{q_-}^{q_+} dq \int_0^{\pi/2} d\theta \int_0^{2\pi} d\phi \frac{q \sin^2 \theta \exp(-|r|Q \cos \alpha)}{\tilde{\omega}^2 + Q^2 v_{\perp}^2} \operatorname{Im} \left(\frac{-1}{\varepsilon(Q, \omega) + 1} \right) \\
& \quad \times \left[2 \cos \left(\frac{\tilde{\omega} r}{v} \right) - \exp(-|r|Q \cos \alpha) \right] \Theta(r)
\end{aligned} \tag{3.27}$$

In Eqs. (3.26) and (3.27), the terms involving $\text{Im}\left(\frac{-1}{\varepsilon+1}\right)$ are the contribution from the surface excitation, whereas the terms involving $\text{Im}\left(\frac{-1}{\varepsilon}\right)$ are the contribution from the volume excitation. These two equations reveal that only surface excitation occurs outside the solid, while both volume and surface excitations occur inside the solid. Since the term $\exp(-|r|Q\cos\alpha)$ exists in Eqs. (3.26) and (3.27), the contribution of the surface excitation exponentially decreases with the increasing distance from the surface, whereas the reduction in the contribution of the volume excitation increases rapidly near the surface. Besides, when $r \rightarrow -\infty$ in Eq. (3.26) or $r \rightarrow \infty$ in Eq. (3.27), i.e. deep inside the solid, it is seen that the forms of these two equations are consistent with the form for electrons moving in an infinite solid.

Letting $\alpha = 0^0$ in Eqs. (3.26) and (3.27), formulas for normally escaping and incident electrons exhibit similarities between present and previous works (Kwei *et al.* 1998b). The difference between these works is attributed to the application of momentum-energy conservations. In the previous work, the integration over the normal component of the momentum transfer, q_z , was not restricted by the conservation relations. In the present work, however, these relations are completely satisfied due to the adoption of spherical coordinates in momentum integration.

According to Eq. (3.25), then the IMFP for escaping and incident electrons can be derived from Eqs. (3.26) and (3.27). They are given by, respectively,

$$\frac{1}{\lambda_i^{s \rightarrow v}(\alpha, E, r)} = \int_0^E u^{s \rightarrow v}(\alpha, E, \omega, r) d\omega, \quad (3.28)$$

and

$$\frac{1}{\lambda_i^{v \rightarrow s}(\alpha, E, r)} = \int_0^E u^{v \rightarrow s}(\alpha, E, \omega, r) d\omega. \quad (3.29)$$

Using Eqs. (3.26) ~ (3.29) and adopting the extended Drude dielectric function (Kwei *et al.* 1993), we can calculate the DIIMFPs and IMFPs for an electron incident into or escaping from a solid surface. The fitting parameters of the model dielectric functions were taken from the previous work of Kwei *et al.* (1993).

Figures 3.2 and 3.3 show the results of electron DIIMFPs outside and inside the solid at various distances relative to the crossing angle point at the surface, respectively, for a 500 eV escaping electron moving from Cu to vacuum in several directions. It is seen that the DIIMFPs vary with the distance in both figures. In Fig. 3.2, the DIIMFP on the vacuum side is entirely contributed by the surface excitations. As the electron is closer to the surface, the DIIMFP curves for fixed crossing angles are getting wider and their peak values are getting larger due to the increasing surface excitations. Meanwhile, the surface excitations increase for larger crossing angles at the fixed distance from the crossing point because of the shorter distance to the surface. It is also found that the characteristic surface plasmon energy, corresponding to the peak energy loss, is nearly independent of the crossing angle and the electron distance from the crossing point. In Fig. 3.3, the DIIMFPs inside the solid vary with the distances from the crossing point. The DIIMFP is a broad function of the energy loss due to the overlapping between the contributions of surface and volume excitations. It is seen that the dependence of DIIMFP on the crossing angle is rather weak inside the solid and is getting weaker as the electron is farther away from the surface. Slightly inside the solid, the DIIMFP quickly approaches to the value of the electron moving in an infinite solid, which reveals that

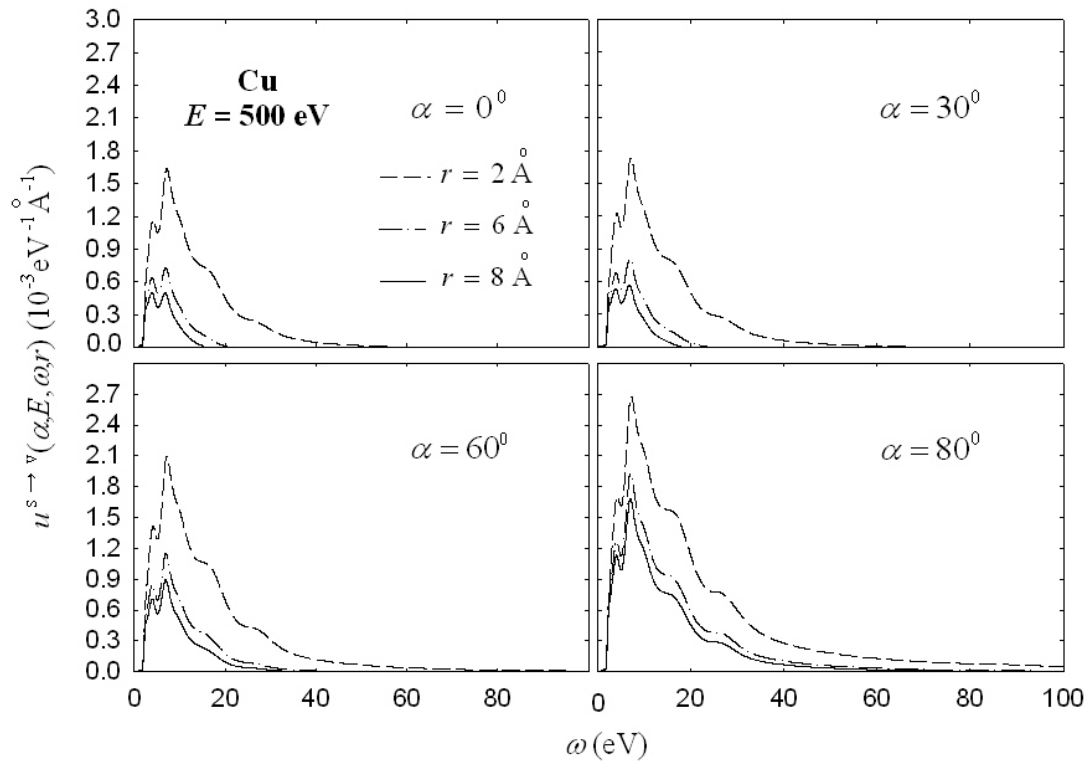


Fig. 3.2 Calculated results of the DIIMFP in vacuum for a 500 eV escaping electron from Cu to vacuum with different crossing angles and distances from the crossing point at the surface.

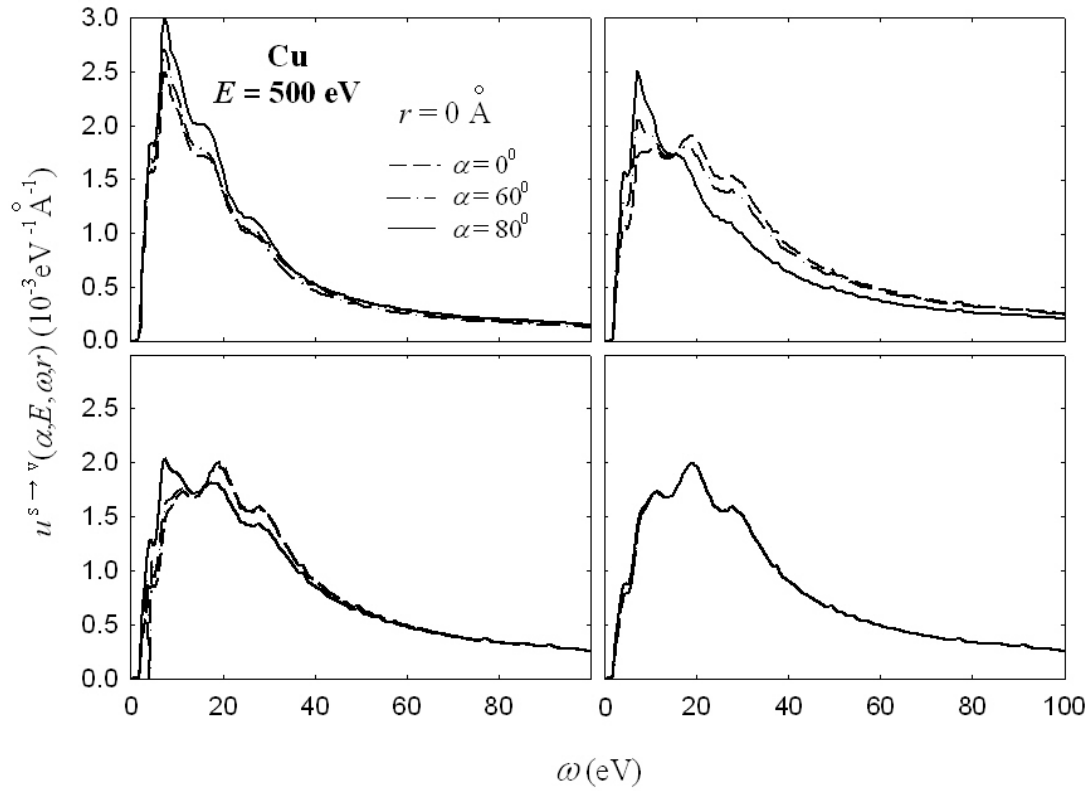


Fig. 3.3 Calculated results of the DIIMFP in Cu for a 500 eV escaping electron from Cu to vacuum with different crossing angles and distances from the crossing point at the surface.

surface excitations are restricted to a limited region near the surface. For a 500 eV incident electron moving from vacuum to Cu, similar results outside and inside the solid are respectively plotted in Figs. 3.4 and 3.5. Again, surface excitations are important as the electron moves near the surface. The DIIMFP on the vacuum side is enhanced for larger crossing angle, while the angular dependence of DIIMFP inside the solid is weak.

Using Eq. (3.28), we have calculated the IMFPs for a 500 eV escaping electron moving from Cu to vacuum as a function of electron position relative to the crossing point. These results are shown in Fig. 3.6 for several crossing angles. Outside the solid, the IMFPs do not fall off to zero abruptly. In addition, the IMFP outside the solid decays more rapidly for smaller crossing angle. This indicates that electrons have more probability to excite surface plasmons for larger crossing angles at the same relative distance to the crossing point. Inside the solid, the IMFPs are roughly independent of relative distance and crossing angle due to the approximate compensation of volume and surface excitations. Therefore, the IMFP inside the solid can be approximated as a constant equal to the IMFP for electrons moving in an infinite solid. A similar plot of IMFPs for 500 eV incident electrons moving from vacuum to Cu in several directions is shown in Fig. 3.7. Here the IMFP of the incident electron in vacuum is lowered as compared to the result of the escaping electron. This is because the attractive force acting on the incident electron by induced surface charges is parallel to the moving direction of the electron and accelerates the electron in vacuum. However, the attractive force on escaping electron in vacuum is antiparallel to the moving direction of the electron and decelerates the electron. Therefore, the time is spent less for incident electron than that for escaping electron, and surface excitation is less probable for incident electron.

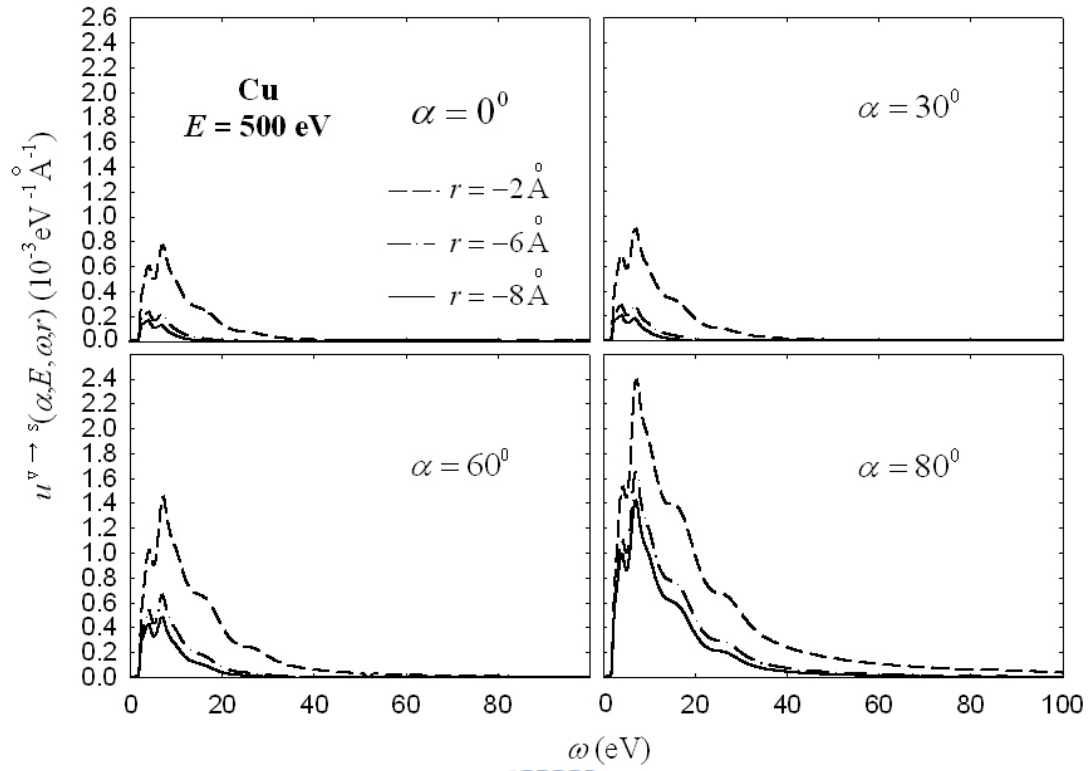


Fig. 3.4 Calculated results of the DIIMFP in vacuum for a 500 eV incident electron from vacuum to Cu with different crossing angles and distances from the crossing point at the surface.

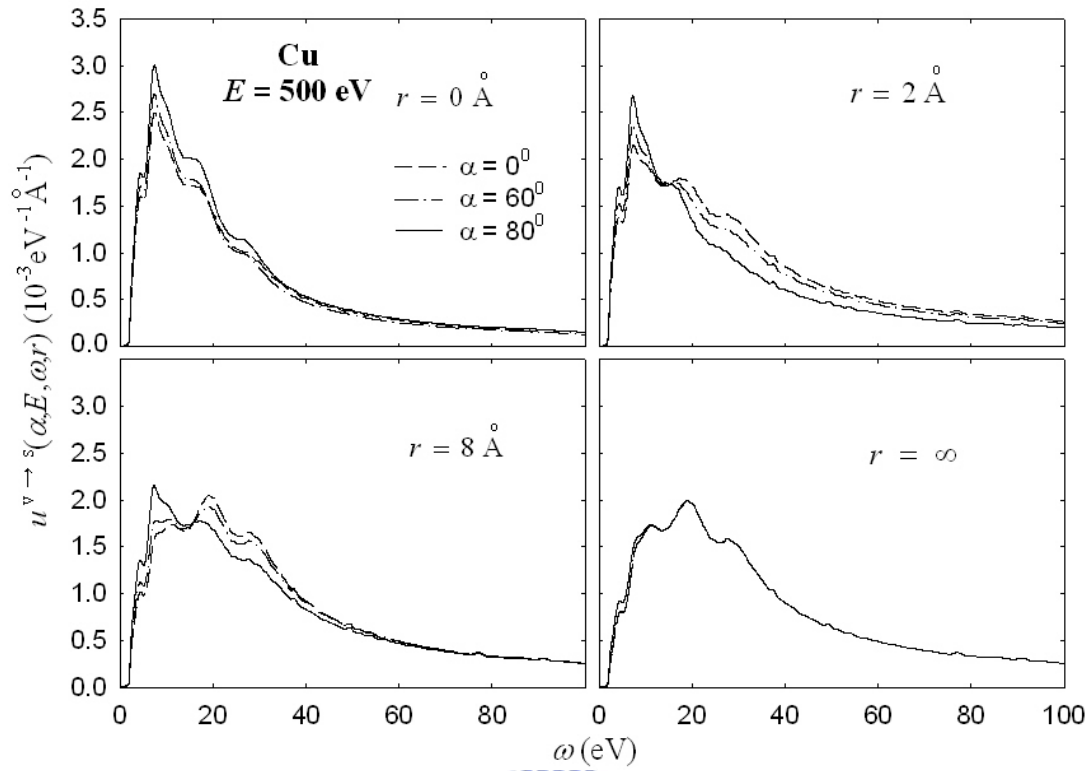


Fig. 3.5 Calculated results of the DIIMFP in Cu for a 500 eV incident electron from vacuum to Cu with different crossing angles and distances from the crossing point at the surface.

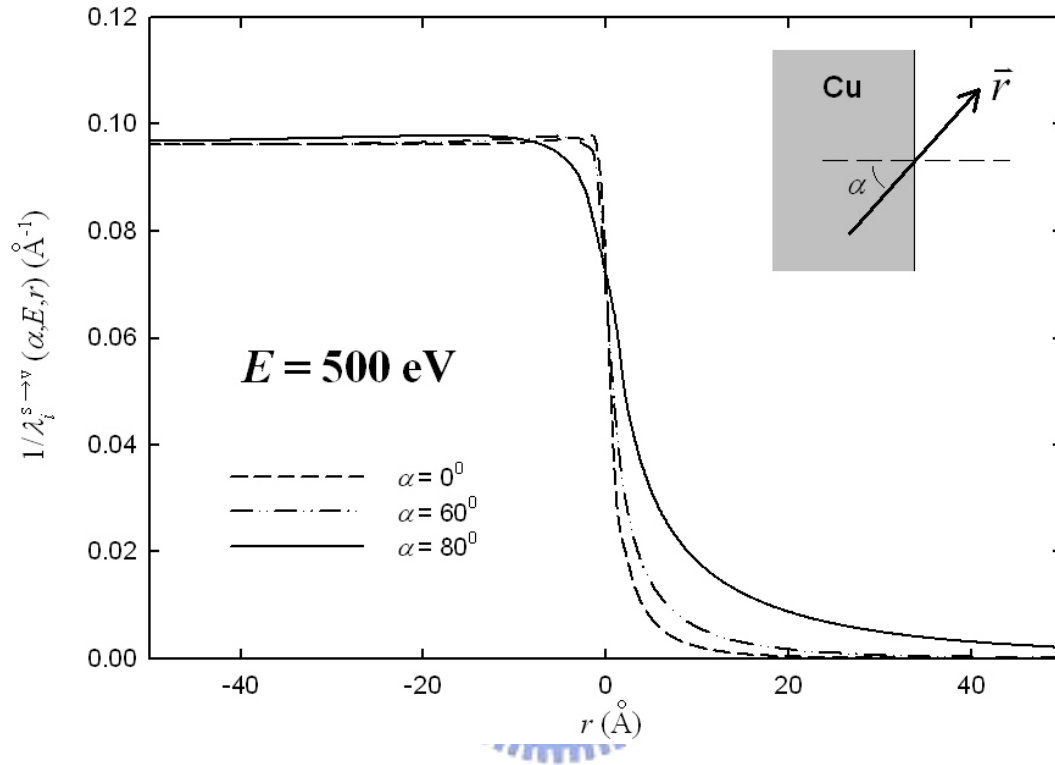


Fig. 3.6 A plot of the inverse IMFP for a 500 eV escaping electron from Cu to vacuum with different crossing angles as a function of electron distance from the crossing point at the surface.

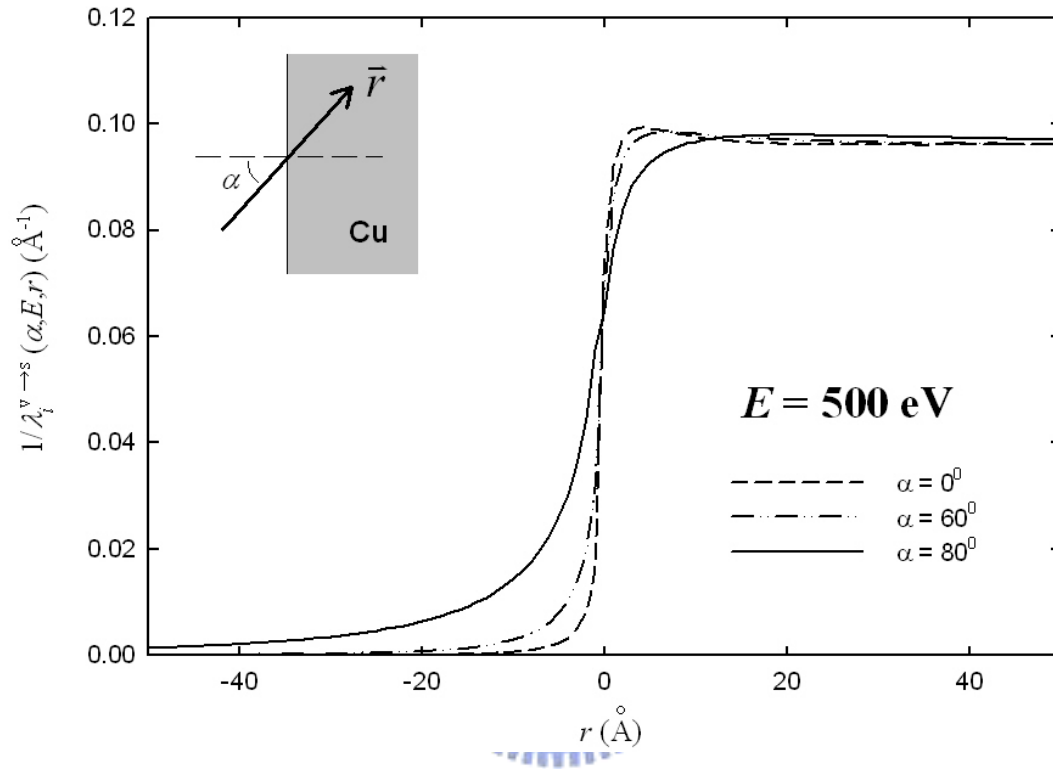


Fig. 3.7 A plot of the inverse IMFP for a 500 eV incident electron from vacuum to Cu with different crossing angles as a function of electron distance from the crossing point at the surface.

3.3 Surface Excitation Parameter

The surface excitation parameter (SEP) was introduced to indicate the mean number of excited surface plasmons as electrons moving across a solid surface. At an earlier time, SEP was determined by the integration of the inverse IMFP contributed by the surface excitation with respect to the whole path length of the electron moving on both sides of the surface (Chen and Kwei 1996). By this definition, the excitations inside the solid were separated into individual surface excitation and volume excitation. However, inside the solid, it is more convenient to deal with surface and volume excitations together rather than separately due to the fact that the approximate compensation of surface and volume excitations makes the IMFPs roughly being constants (Kwei *et al.* 1998b). Therefore, we applied the recent calculation of SEP suggested by Kwei *et al.* (1998b), who calculated SEP by the integration of inverse IMFP over the whole path length of the electron in vacuum. By means of Eqs. (3.28) and (3.29), the SEPs for electrons escaping from and incident into a solid surface are obtained by

$$P_s^{s \rightarrow v}(\alpha, E) = \int_0^{\infty} \frac{dr}{\lambda_i^{s \rightarrow v}(\alpha, E, r)}, \quad (3.30)$$

and

$$P_s^{v \rightarrow s}(\alpha, E) = \int_{-\infty}^0 \frac{dr}{\lambda_i^{v \rightarrow s}(\alpha, E, r)}. \quad (3.31)$$

Figure 3.8 shows the cross-angle-dependent SEPs calculated using Eq. (3.30) for

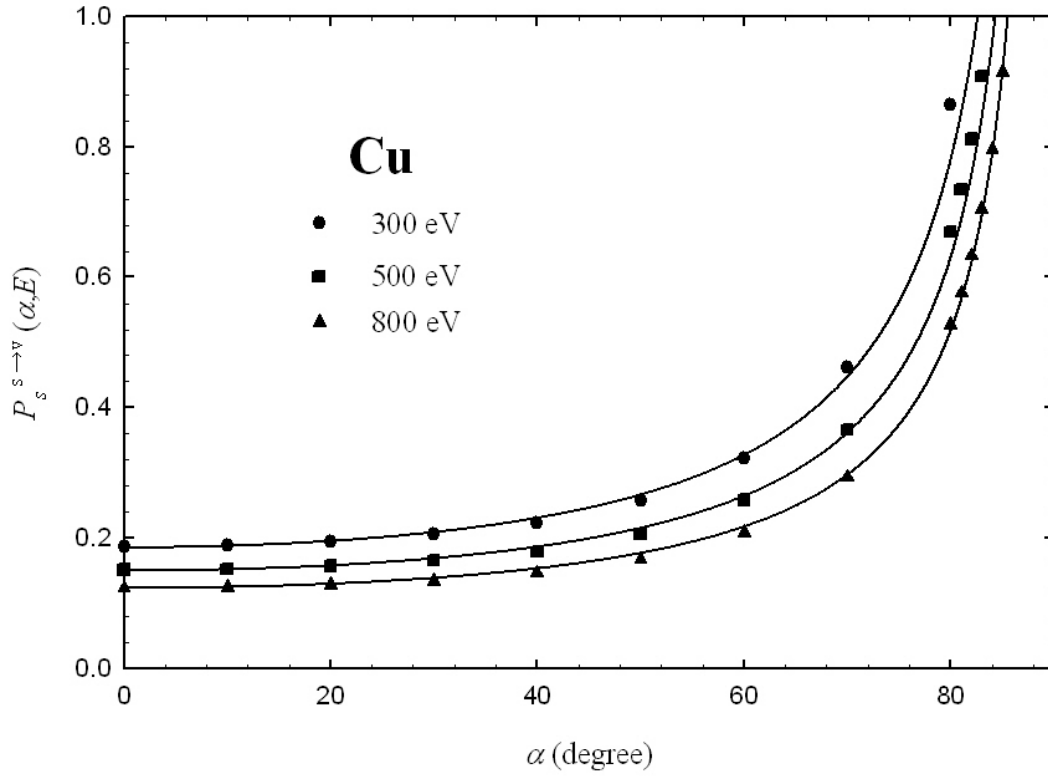


Fig. 3.8 A plot of the crossing-angle-dependent SEPs calculated using Eq. (3.30) for the escaping electrons of 300 eV (solid circles), 500 eV (solid squares) and 800 eV (solid triangles) moving from Cu to vacuum. The corresponding fitted values obtained from Eq. (3.32) are displayed by solid curves.

the escaping electrons of 300 eV (solid circles), 500 eV (solid squares) and 800 eV (solid triangles) moving from Cu to vacuum. Similar results calculated using Eq. (3.31) for incident electrons moving from vacuum to Cu are plotted in Fig. 3.9. It can be seen that the SEPs, for both cases, increase with the increasing of the crossing angle α . When $\alpha > 70^\circ$, the increase of SEP is rapid. Thus, the surface excitations are more probable for larger crossing angle. Besides, at fixed α , we can see that the SEP values decrease with the increasing energy of electrons. To investigate this phenomenon, we plotted the calculated SEPs versus various electron's energies with $\alpha = 0^\circ$ and $\alpha = 50^\circ$ in Fig. 3.10 for escaping electrons and in Fig. 3.11 for incident electrons. The reason for larger SEP value at lower energy is that the electron of lower energy moves in vacuum for more time. Then surface plasmon are excited more. By comparing Figs. 3.8 with 3.9 or Figs. 3.10 with 3.11, the SEP for the incident electron is lower than the result for the escaping electron. This finding and its explanation are the same as the preceding mention for inverse IMFP. Thus the surface excitation is more probable for escaping electrons. Examining these computed results of SEP in Figs. 3.8 ~ 3.11, we found that the SEP follows the equation:

$$P_s^{s \rightarrow v}(\alpha, E) \text{ or } P_s^{v \rightarrow s}(\alpha, E) = \frac{aE^{-b}}{\cos^c \alpha}. \quad (3.32)$$

The best-fitted values of the parameters for electrons moving from Cu to vacuum and for electrons moving from vacuum to Cu are listed in Table 1 and Table 2, respectively. The curves versus crossing angle and energy of the fittings are also plotted (solid curves) in Figs. 3.8 ~ 3.11. For Au and Ag, we list the fitted values of the parameters in Table 3.1 and Table 3.2 for escaping and incident electrons.

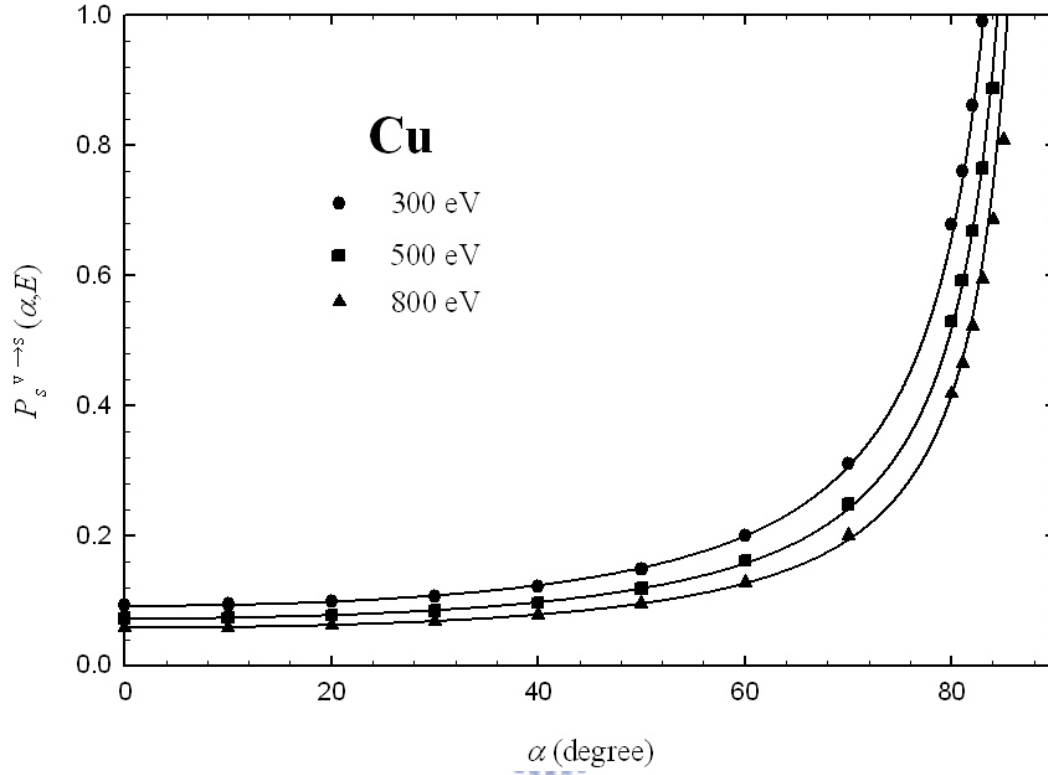


Fig. 3.9 A plot of the crossing-angle-dependent SEPs calculated using Eq. (3.31) for the incident electrons of 300 eV (solid circles), 500 eV (solid squares) and 800 eV (solid triangles) moving from vacuum to Cu. The corresponding fitted values obtained from Eq. (3.32) are displayed by solid curves.

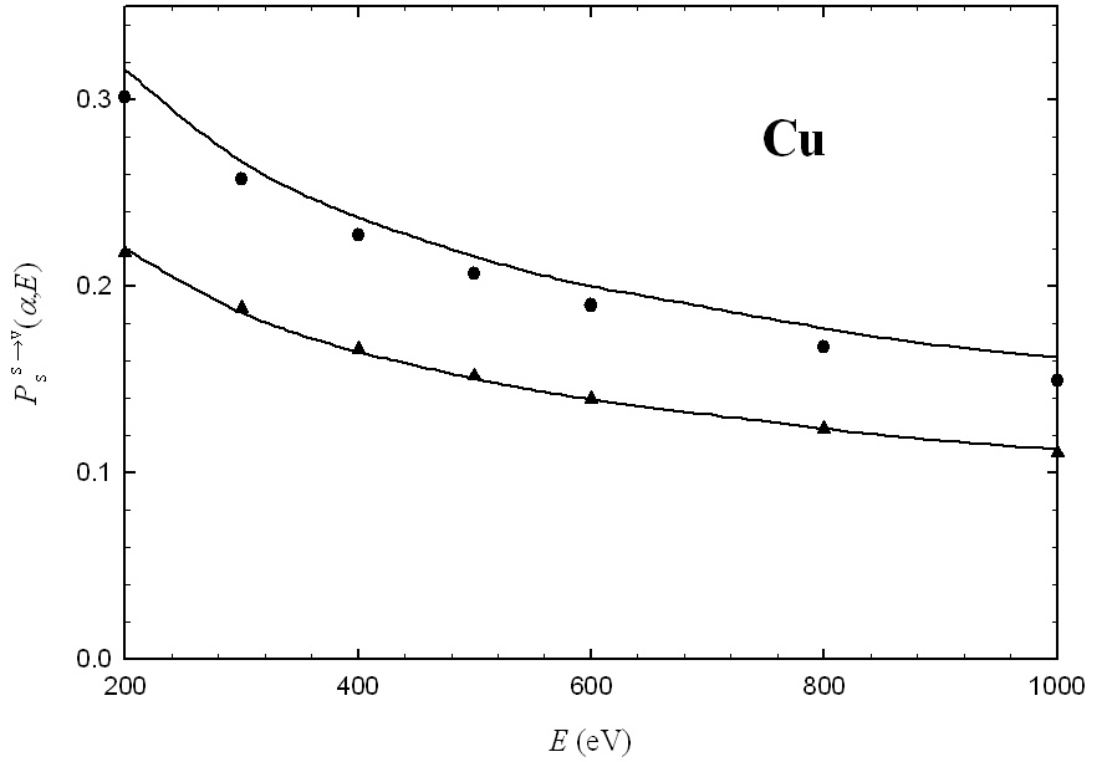


Fig. 3.10 A plot of SEPs versus energy calculated using Eq. (3.30) for electrons escaping from Cu by the crossing angle $\alpha = 0^\circ$ (solid triangles) and $\alpha = 50^\circ$ (solid circles). The corresponding fitted values obtained from Eq. (3.32) are displayed by solid curves.

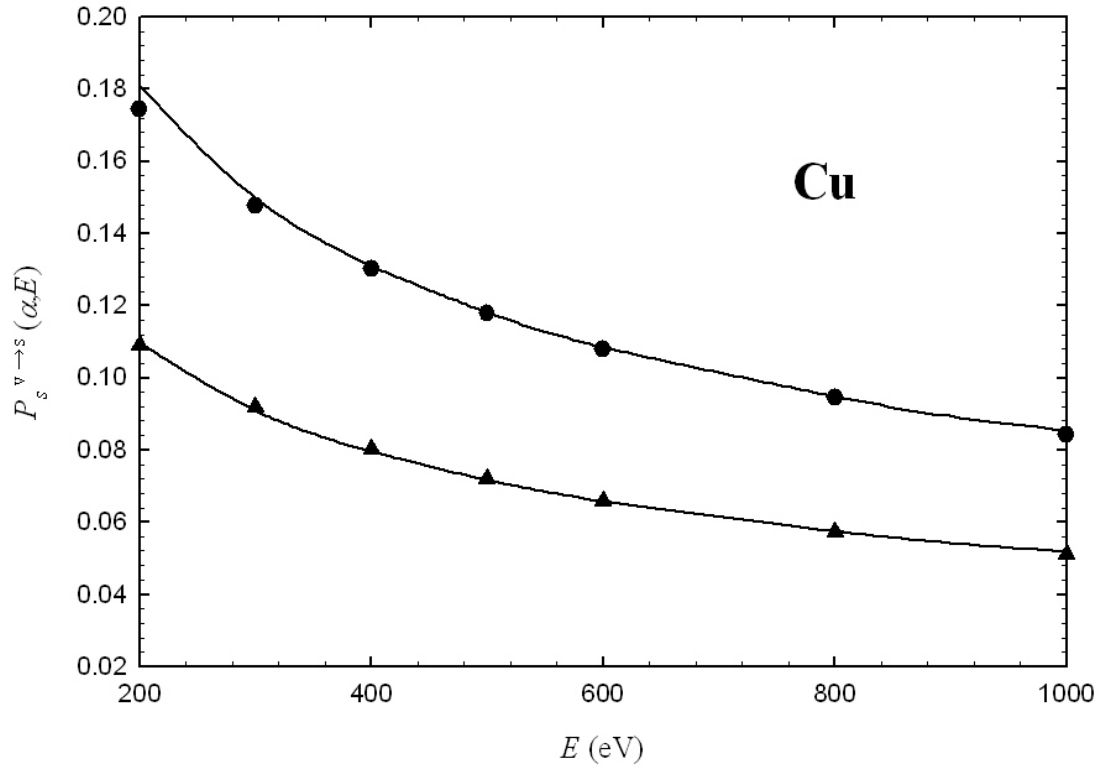
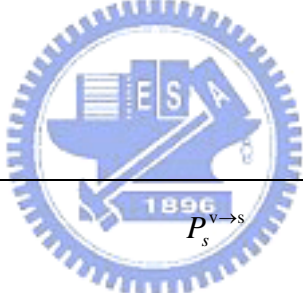


Fig. 3.11 A plot of SEPs versus energy calculated using Eq. (3.31) for electrons incident into Cu by the crossing angle $\alpha = 0^\circ$ (solid triangles) and $\alpha = 50^\circ$ (solid circles). The corresponding fitted values obtained from Eq. (3.32) are displayed by solid curves.

	$P_s^{s \rightarrow v}$		
	a	b	c
Au	1.8695	0.4052	0.80
Ag	2.1203	0.4260	0.74
Cu	1.9994	0.4166	0.82

Table 3.1 Fitted values of parameters a , b and c in Eq. (3.32) for escaping electrons



	$P_s^{v \rightarrow s}$		
	a	b	c
Au	1.88476	0.50601	1.06
Ag	1.42601	0.48209	1.05
Cu	1.2999	0.4664	1.13

Table 3.2 Fitted values of parameters a , b and c in Eq. (3.32) for incident electrons

Moreover, in Figs. 3.12 ~ 3.15, we compared our fitted values and calculated results of SEPs versus crossing angle and energy with the results of Oswald's fitting formula (1997) (dotted curves) for incident and escaping electrons and with the results of Chen's fitting formula (2002) (dashed curves) using cylindrical coordinates in momentum integration for escaping electrons. A substantial difference between our results and Oswald's results was found, especially for incident electrons. For escaping electrons, a discrepancy between the crossing-angle-dependent SEP values of Chen and our results can be seen, and the difference between our and Chen's results of SEP versus energy are also seen. The fitted formula of Chen (2002) for the calculation of SEP is only applicable for escaping electrons, but not for incident electrons. Our calculations have been made for both incident and escaping electrons.



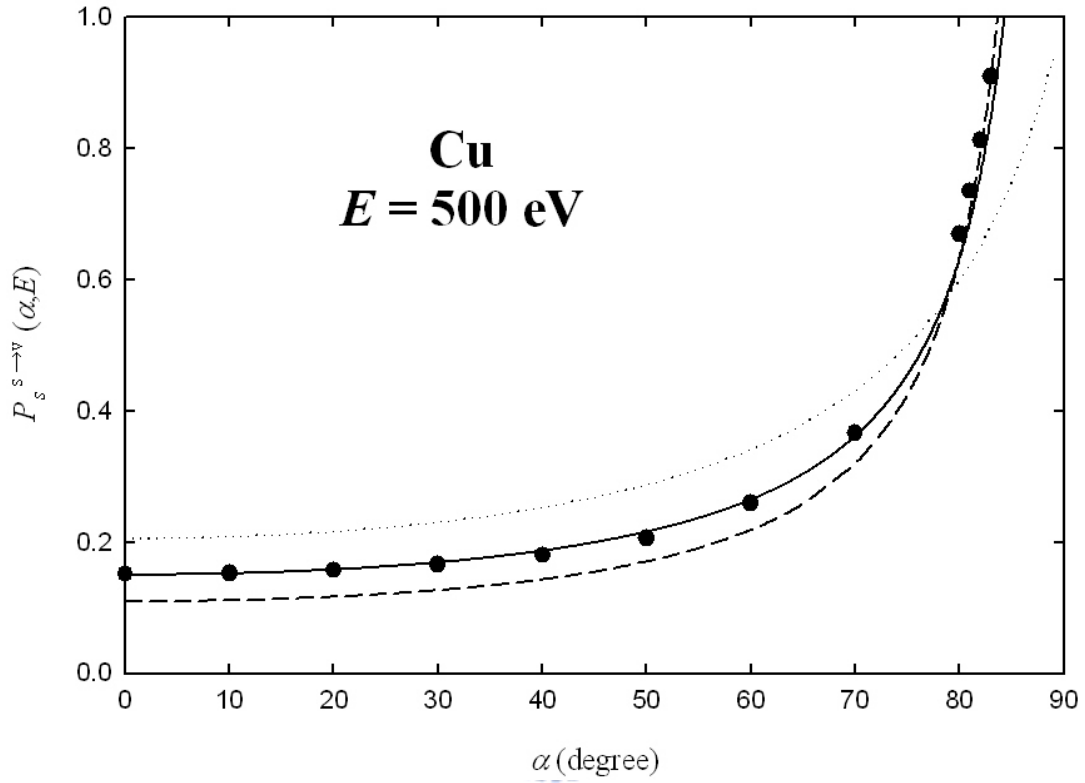


Fig. 3.12 A plot of the SEP for a 500 eV escaping electron from Cu to vacuum as a function of crossing angle. Symbols are the calculated results using Eq. (3.30). Solid curve is the fitting results using Eq. (3.32). Corresponding data of Chen (2002) (dashed curve) and Oswald (1997) (dotted curve) are plotted for comparisons.

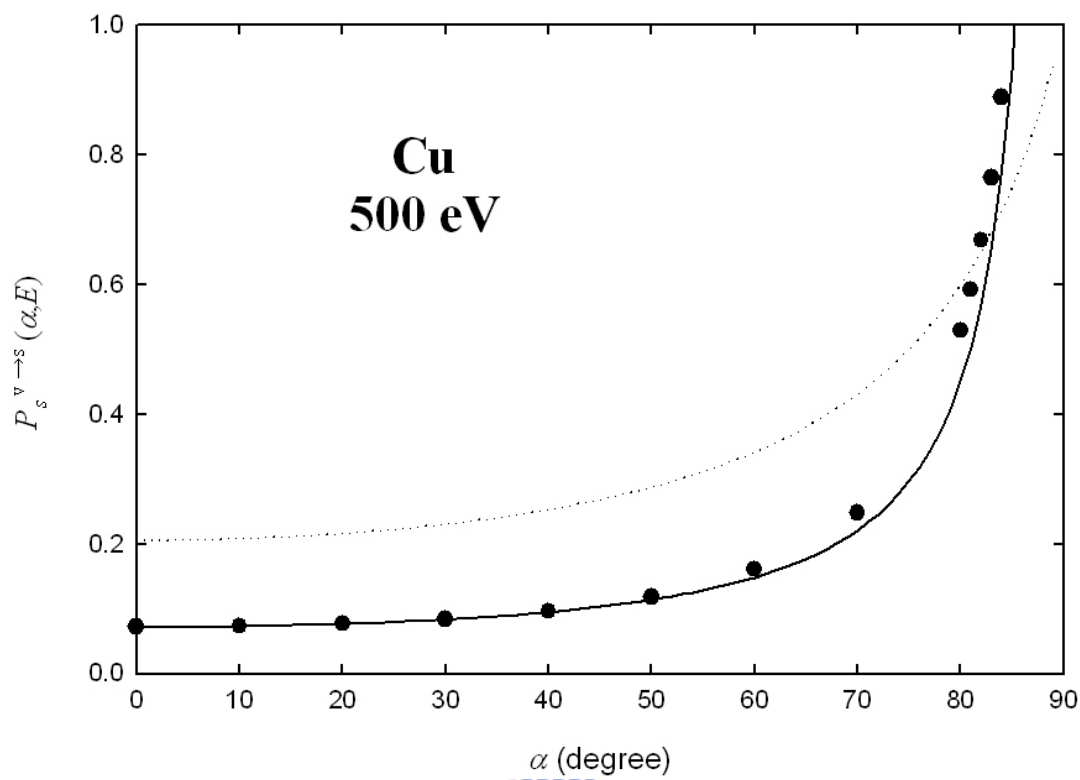


Fig. 3.13 A plot of the SEP for a 500 eV incident electron from vacuum to Cu as a function of crossing angle. Symbols are the calculated results using Eq. (3.31). Solid curve is the fitting results using Eq. (3.32). Corresponding data of Oswald (1997) (dotted curve) are plotted for comparisons.

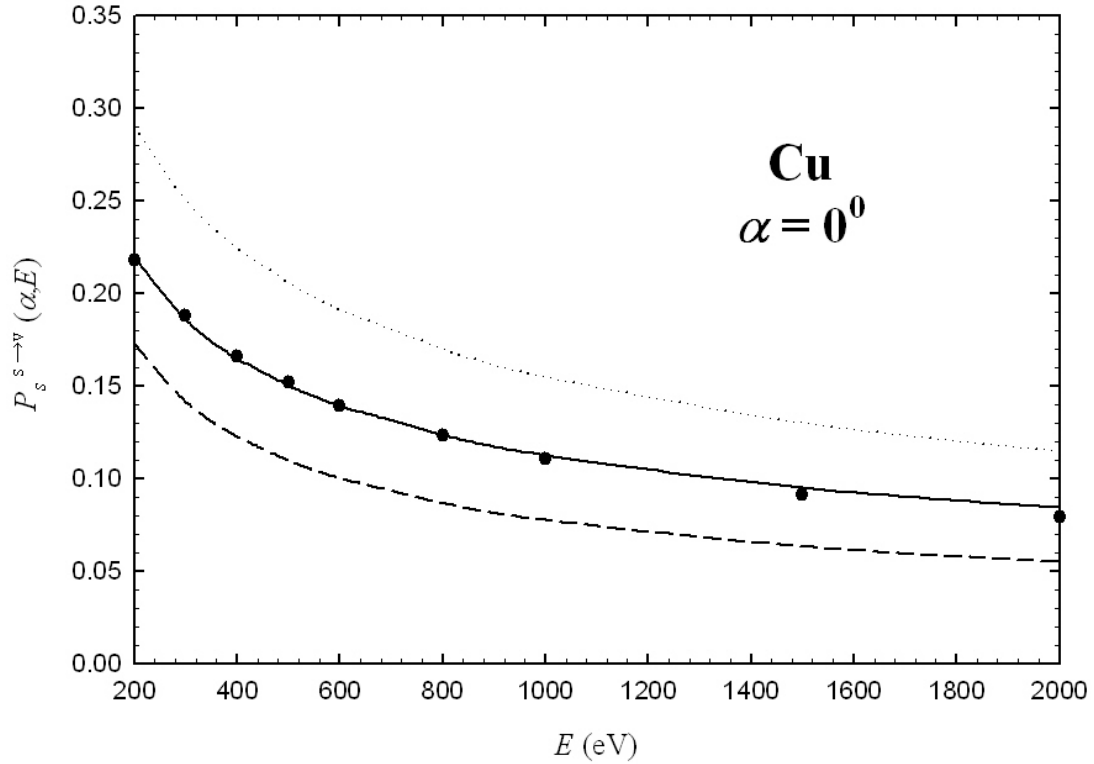


Fig. 3.14 A plot of the SEP versus energy for an electron escaping from Cu to vacuum by $\alpha = 0^0$. Symbols are the calculated results using Eq. (3.30). Solid curve is the fitting results using Eq. (3.32). Corresponding data of Chen (2002) (dashed curve) and Oswald (1997) (dotted curve) are plotted for comparisons.

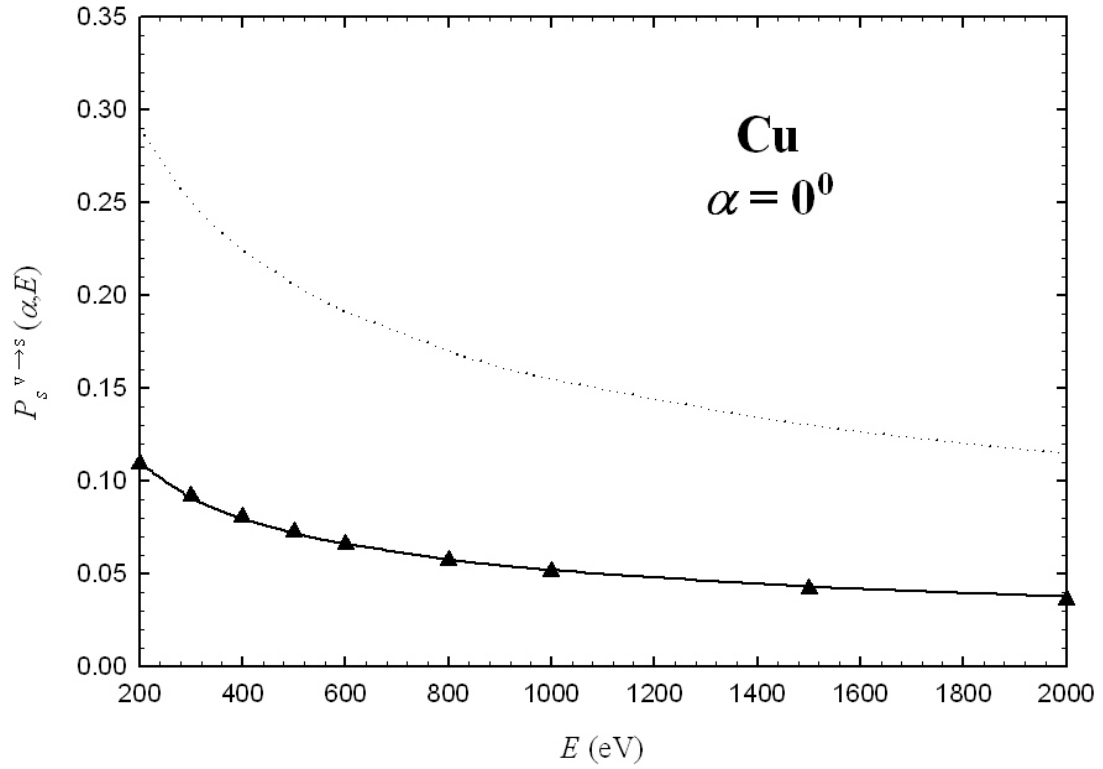


Fig. 3.15 A plot of the SEP versus energy for an electron escaping from vacuum to Cu by $\alpha = 0^0$. Symbols are the calculated results using Eq. (3.31). Solid curve is the fitting results using Eq. (3.32). Corresponding data of Oswald (1997) (dotted curve) are plotted for comparisons.

3.4 The Inelastic-Scattering Model with Retardation Effect

When an electron moves near a solid, the electric field is induced. The induced electric field has influence on the electron's motion. Conventionally, the induced electric field can be calculated by solving the Poisson equation. In this approach, it was assumed that the induced electric field propagated to the electron simultaneously. Actually, the induced electric field needs propagation time to influence the motion of the electron. In other words, the effect observed on the electron is caused by the action of the induced electric field at earlier or retarded time. This phenomenon is called the retardation effect (Jackson 1975). For the electron of low and intermediate speed, the retardation effect can be ignored so that the Poisson equation is applicable in the calculation of electric fields. However, if the speed of the electron is very high, the Poisson equation is not adequate since the retardation effect becomes significant (Marks 1982; Cowley 1982a, 1982b; Moreau *et al.* 1997). The aim of the present study in this section is to establish a model with the retardation effect. By employing the extended Drude dielectric function with spatial dispersion (Kwei *et al.* 1993) in the dielectric response theory, we modify the preceding inelastic-scattering model to include the retardation effect in the derivation for the inelastic interaction of high-energy electrons moving parallel to solid surfaces.

3.4.1 The Basic Knowledge

As mentioned in section 3.1, the Maxwell equations, Eq. (3.1), govern the electromagnetic interaction between a charged particle and a medium. To derive the inelastic-scattering model with retardation effect, the Maxwell equations are therefore the starting points in this section. The Maxwell equations in Eqs. (3.1a), (3.1b),

(3.1c) and (3.1d) in Fourier transformed forms are given by (Dressel and Grüner 2002)

$$\bar{q} \cdot \bar{\mathbf{B}}(\bar{q}, \omega) = 0, \quad (3.33a)$$

$$\bar{q} \times \bar{\mathbf{E}}(\bar{q}, \omega) - \frac{\omega}{c} \bar{\mathbf{B}}(\bar{q}, \omega) = 0, \quad (3.33b)$$

$$i\bar{q} \cdot \bar{\mathbf{D}}(\bar{q}, \omega) = 4\pi\rho(\bar{q}, \omega), \quad (3.33c)$$

and

$$i\bar{q} \times \bar{\mathbf{H}}(\bar{q}, \omega) + \frac{i\omega}{c} \bar{\mathbf{D}}(\bar{q}, \omega) = \frac{4\pi}{c} \bar{\mathbf{J}}(\bar{q}, \omega), \quad (3.33d)$$

where $\bar{\mathbf{H}}(\bar{q}, \omega)$ and $\bar{\mathbf{B}}(\bar{q}, \omega)$ are the Fourier components of the magnetic field and the magnetic induction, respectively. The solutions of $\bar{\mathbf{B}}(\bar{r}, t)$ and $\bar{\mathbf{E}}(\bar{r}, t)$ in Eqs. (3.1a) and (3.1b) can be defined in terms of a vector potential $\bar{\mathbf{A}}(\bar{r}, t)$ and a scalar potential $\Phi(\bar{r}, t)$ (Jackson 1975); that is,

$$\bar{\mathbf{B}}(\bar{r}, t) = \nabla \times \bar{\mathbf{A}}(\bar{r}, t), \quad (3.34)$$

and

$$\bar{\mathbf{E}}(\bar{r}, t) = -\nabla\Phi(\bar{r}, t) - \frac{1}{c} \frac{\partial \bar{\mathbf{A}}(\bar{r}, t)}{\partial t}. \quad (3.35)$$

The Fourier components of Eqs. (3.34) and (3.35) are given by (Dressel and Grüner

2002)

$$\bar{\mathbf{B}}(\bar{q}, \omega) = i\bar{q} \times \bar{\mathbf{A}}(\bar{q}, \omega), \quad (3.36)$$

and

$$\bar{\mathbf{E}}(\bar{q}, \omega) = -i\bar{q}\Phi(\bar{q}, \omega) + i\frac{\omega}{c}\bar{\mathbf{A}}(\bar{q}, \omega). \quad (3.37)$$

Substituting Eqs. (3.36) and (3.37) and the relations, $\bar{\mathbf{D}}(\bar{q}, \omega) = \varepsilon(\bar{q}, \omega)\bar{\mathbf{E}}(\bar{q}, \omega)$ and $\bar{\mathbf{B}}(\bar{q}, \omega) = \mu\bar{\mathbf{H}}(\bar{q}, \omega)$, into Eqs. (3.33c) and (3.33d), the Maxwell equations can be reduced to

$$q^2\bar{\mathbf{A}}(\bar{q}, \omega) - \frac{\omega^2\mu\varepsilon(\bar{q}, \omega)}{c^2}\bar{\mathbf{A}}(\bar{q}, \omega) + \bar{q}\left[-\bar{q} \cdot \bar{\mathbf{A}}(\bar{q}, \omega) + \frac{\omega\mu\varepsilon(\bar{q}, \omega)}{c}\Phi(\bar{q}, \omega)\right], \quad (3.38)$$

$$= \frac{4\pi\mu}{c}\bar{\mathbf{J}}(\bar{q}, \omega)$$

and

$$q^2\Phi(\bar{q}, \omega) - \frac{\omega}{c}\bar{q} \cdot \bar{\mathbf{A}}(\bar{q}, \omega) = \frac{4\pi\rho(\bar{q}, \omega)}{\varepsilon(\bar{q}, \omega)}, \quad (3.39)$$

where μ is the permeability. However, Eqs. (3.38) and (3.39) are still coupled equations. To uncouple them, the Lorentz gauge (Jackson 1975)

$$\nabla \cdot \bar{\mathbf{A}}(\bar{r}, t) + \frac{\mu\varepsilon}{c} \frac{\partial\Phi(\bar{r}, t)}{\partial t} = 0 \quad (3.40)$$

is employed. Here the Lorentz gauge in Fourier transformed form can be obtained by

$$-\vec{q} \cdot \vec{A}(\vec{q}, \omega) + \frac{\omega \mu \varepsilon(\vec{q}, \omega)}{c} \Phi(\vec{q}, \omega) = 0. \quad (3.41)$$

Using Eq. (3.41), then Eqs. (3.38) and (3.39) can be uncoupled and become

$$q^2 \vec{A}(\vec{q}, \omega) - \frac{\omega^2 \mu \varepsilon(\vec{q}, \omega)}{c^2} \vec{A}(\vec{q}, \omega) = \frac{4\pi\mu}{c} \vec{J}(\vec{q}, \omega), \quad (3.42)$$

and

$$q^2 \Phi(\vec{q}, \omega) - \frac{\omega^2 \mu \varepsilon(\vec{q}, \omega)}{c^2} \Phi(\vec{q}, \omega) = \frac{4\pi\rho(\vec{q}, \omega)}{\varepsilon(\vec{q}, \omega)}. \quad (3.43)$$

These two equations are the Fourier components of the wave equations for \vec{A} and Φ .

As mentioned in section 3.1, boundary conditions must be satisfied to solve the electromagnetic boundary-value problems. To solve the differential wave equations of Eqs. (3.42) and (3.43), the boundary conditions mentioned in section 3.1 for the normal component of the electric displacement and for the tangential components of the electric field are not enough. The other boundary conditions for the normal components of the magnetic induction and for the tangential components of magnetic field are necessary (Jackson 1975). That is, the normal component of the magnetic induction and the tangential components of the magnetic field are continuous on the boundary.

3.4.2 The Induced Vector and Scalar Potentials for Electrons Moving Parallel to an Interface

With the help of the boundary conditions and based on the dielectric response theory, we use the wave equations shown in Eq. (3.42) to derive the inelastic-scattering model with retardation effect for high-speed electrons moving parallel to an infinite interface. This problem to be solved is illustrated in Fig. 3.16, where an electron of charge e and speed v moving in positive x -direction and parallel to an interface (at $z = 0$) between medium 1 of dielectric function $\varepsilon_1(\vec{q}, \omega)$ (at $z < 0$) and medium 2 of dielectric function $\varepsilon_2(\vec{q}, \omega)$ (at $z > 0$). The electron is located in medium 1 at a distance d from the interface, and its instant position at time t is expressed as $(vt, 0, -d)$. In our work, since we are interested in the inelastic interaction between electrons and non-magnetic media, both permeabilities of medium 1 and medium 2 are equal to 1.

Again, the atomic units are used unless otherwise specified in this section. Then the charge density of the electron $\rho_f(\vec{r}, t)$ is given by

$$\rho_f(\vec{r}, t) = -\delta(x - vt)\delta(y)\delta(z + d). \quad (3.44)$$

Using the principles of Fourier transform, the Fourier component of this electron charge density can be given by

$$\begin{aligned} \rho_f(\vec{q}, \omega) &= \int_{-\infty}^{\infty} \int_{-\infty}^{\infty} \rho_f(\vec{r}, t) \exp[-i(\vec{q} \cdot \vec{r} - \omega t)] dt d\vec{r} \\ &= - \int_{-\infty}^{\infty} \int_{-\infty}^{\infty} \delta(x - vt)\delta(y)\delta(z + d) \exp[-i(\vec{q} \cdot \vec{r} - \omega t)] dt d\vec{r} . \\ &= -2\pi\delta(\omega - q_x v) \exp(iq_z d) \end{aligned} \quad (3.45)$$

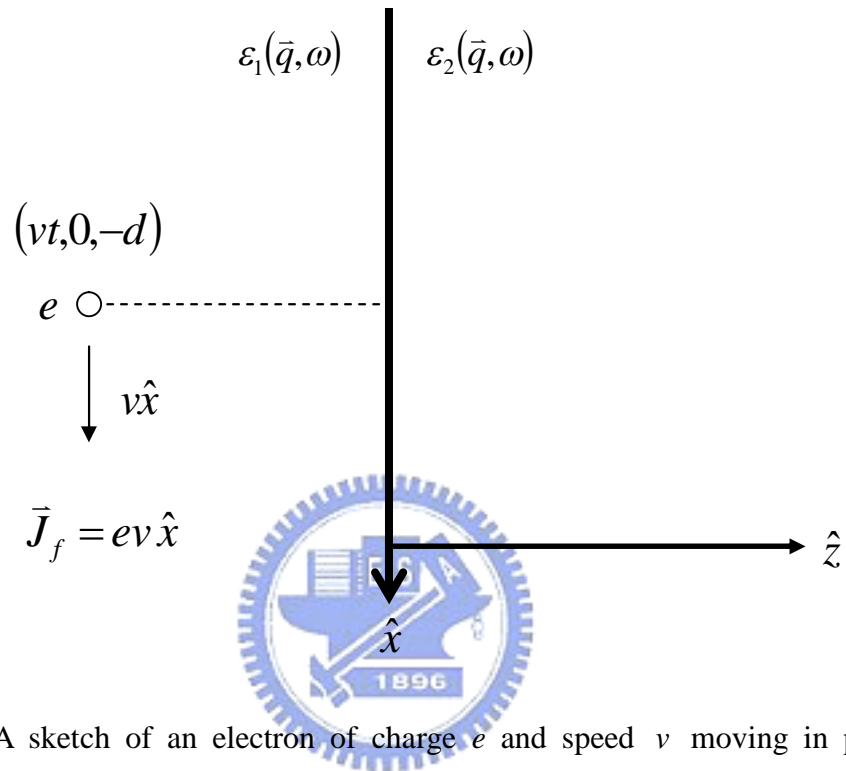


Fig. 3.16 A sketch of an electron of charge e and speed v moving in positive x -direction and parallel to an interface (at $z=0$) between medium 1 of dielectric function $\varepsilon_1(\vec{q}, \omega)$ (at $z < 0$) and medium 2 of dielectric function $\varepsilon_2(\vec{q}, \omega)$ (at $z > 0$). The permeabilities of medium 1 and medium 2 are equal to 1. The electron is located in medium 1 at a distance d from the interface, and its instant position at time t is expressed as $(vt, 0, -d)$.

Besides, the moving electron can also be regarded as a current. Hence the current density arising from $\rho_f(\vec{r}, t)$ can be determined by (Cheng 1989)

$$\vec{J}_f(\vec{r}, t) = -v\delta(x - vt)\delta(y)\delta(z + d)\hat{x}, \quad (3.46)$$

whre \hat{x} is the unit vector along x -direction. Accordingly, the Fourier components of $\vec{J}_f(\vec{r}, t)$ can be obtained by

$$\begin{aligned} \vec{J}_f(\vec{q}, \omega) &= \int_{-\infty}^{\infty} \int_{-\infty}^{\infty} \vec{J}_f(\vec{r}, t) \exp[-i(\vec{q} \cdot \vec{r} - \omega t)] dt d\vec{r} \\ &= \int_{-\infty}^{\infty} \int_{-\infty}^{\infty} \hat{x} v \delta(x - vt) \delta(y) \delta(z + d) \exp[-i(\vec{q} \cdot \vec{r} - \omega t)] dt d\vec{r} . \\ &= -2\pi v \delta(\omega - q_x v) \exp(iq_z d) \hat{x} \\ &= \rho_f(\vec{q}, \omega) v \hat{x} \end{aligned} \quad (3.47)$$

As mentioned in section 3.2.1, the method of images was applied to solve the boundary-value problem. Here we use this method again. By introducing image current densities on both sides of the interface, the Fourier components of the vector potentials in media 1 and 2, $\vec{A}_1(\vec{q}, \omega)$ and $\vec{A}_2(\vec{q}, \omega)$, can be determined from the wave equation for vector potential presented in Eq. (3.42); that is,

$$\begin{aligned}
& \bar{A}_1(\bar{q}, \omega) \\
&= \frac{4\pi [\bar{J}_f(\bar{q}, \omega) + \bar{J}_{s1}(\bar{q}, \omega)]}{c \left[q^2 - \frac{\omega^2 \mu_1 \varepsilon_1(\bar{q}, \omega)}{c^2} \right]} \\
&= \frac{4\pi [\bar{J}_f(\bar{q}, \omega) + \bar{J}_{s1}(\bar{Q}, \omega)]}{cq_1'^2}, \quad \text{when } z < 0, \quad (3.48) \\
&= \frac{4\pi}{cq_1'^2} [\hat{x} \quad \hat{y} \quad \hat{z}] \begin{bmatrix} J_f(\bar{q}, \omega) + J_{s1,x}(\bar{Q}, \omega) \\ J_{s1,y}(\bar{Q}, \omega) \\ 0 \end{bmatrix}
\end{aligned}$$

and

$$\begin{aligned}
& \bar{A}_2(\bar{q}, \omega) \\
&= \frac{4\pi [\bar{J}_f(\bar{q}, \omega) + \bar{J}_{s2}(\bar{Q}, \omega)]}{c \left[q^2 - \frac{\omega^2 \varepsilon_2(\bar{q}, \omega)}{c^2} \right]} \\
&= \frac{4\pi [\bar{J}_f(\bar{q}, \omega) + \bar{J}_{s2}(\bar{Q}, \omega)]}{cq_2'^2}, \quad \text{when } z > 0, \quad (3.49) \\
&= \frac{4\pi}{cq_2'^2} [\hat{x} \quad \hat{y} \quad \hat{z}] \begin{bmatrix} J_f(\bar{q}, \omega) + J_{s2,x}(\bar{Q}, \omega) \\ J_{s2,y}(\bar{Q}, \omega) \\ 0 \end{bmatrix}
\end{aligned}$$

where $q_1'^2 = q^2 - \frac{\omega^2 \varepsilon_1(\bar{q}, \omega)}{c^2}$, $q_2'^2 = q^2 - \frac{\omega^2 \varepsilon_2(\bar{q}, \omega)}{c^2}$, \hat{y} is the unit vector along y -direction, and \hat{z} is the unit vector along z -direction. $\bar{J}_{s1}(\bar{Q}, \omega)$ and $\bar{J}_{s2}(\bar{Q}, \omega)$ are the fictitious surface current densities right on the surface facing to medium 2 and right on the surface facing to medium 1, respectively. $J_{s1,x}(\bar{Q}, \omega)$ and $J_{s1,y}(\bar{Q}, \omega)$ are the parallel components of $\bar{J}_{s1}(\bar{Q}, \omega)$ in x -direction and y -direction, respectively; the corresponding components of $\bar{J}_{s2}(\bar{Q}, \omega)$ are $J_{s2,x}(\bar{Q}, \omega)$ and

$J_{s2,y}(\bar{Q}, \omega)$. Through the Lorentz gauge shown in Eq. (3.41) with the help of Eqs. (3.48) and (3.49), the Fourier components of the scalar potentials in media 1 and 2 can be determined by

$$\begin{aligned}
& \Phi_1(\bar{q}, \omega) \\
&= \frac{c}{\omega \varepsilon_1(\bar{q}, \omega)} \bar{q} \bullet \bar{A}_1(\bar{q}, \omega) \\
&= \frac{c}{\omega \varepsilon_1(\bar{q}, \omega)} [q_x A_{1,x}(\bar{q}, \omega) + q_y A_{1,y}(\bar{q}, \omega)] \quad , \\
&= \frac{4\pi}{\omega \varepsilon_1(\bar{q}, \omega) q_1'^2} [q_x J_f(\bar{q}, \omega) + q_x J_{s1,x}(\bar{Q}, \omega) + q_y J_{s1,y}(\bar{Q}, \omega)]
\end{aligned} \tag{3.50}$$

and

$$\begin{aligned}
& \Phi_2(\bar{q}, \omega) \\
&= \frac{c}{\omega \varepsilon_2(\bar{q}, \omega)} \bar{q} \bullet \bar{A}_2(\bar{q}, \omega) \\
&= \frac{c}{\omega \varepsilon_2(\bar{q}, \omega)} [q_x A_{2,x}(\bar{q}, \omega) + q_y A_{2,y}(\bar{q}, \omega)] \quad . \\
&= \frac{4\pi}{\omega \varepsilon_2(\bar{q}, \omega) q_2'^2} [q_x J_f(\bar{q}, \omega) + q_x J_{s2,x}(\bar{Q}, \omega) + q_y J_{s2,y}(\bar{Q}, \omega)]
\end{aligned} \tag{3.51}$$

where $\bar{q} = (q_x, q_y, q_z) = (\bar{Q}, q_z)$, and q_x and q_y are the parallel components of \bar{q} in x -direction and in y -direction, respectively. After substituting Eqs. (3.48) ~ (3.51) into Eqs. (3.36) and (3.37), the Fourier components of the magnetic inductions and the electric fields on both sides of the boundary, i.e. $\bar{B}_1(\bar{q}, \omega)$, $\bar{B}_2(\bar{q}, \omega)$, $\bar{E}_1(\bar{q}, \omega)$ and $\bar{E}_2(\bar{q}, \omega)$, can be carried out. By meeting the boundary conditions, then the forms of the fictitious surface current densities, $J_{s1,x}(\bar{Q}, \omega)$, $J_{s1,y}(\bar{Q}, \omega)$, $J_{s2,x}(\bar{Q}, \omega)$ and $J_{s2,y}(\bar{Q}, \omega)$, can be written as, respectively,

$$\begin{aligned}
& J_{s1,x}(\bar{Q}, \omega) \\
& = \left[q_x + \frac{q_y^2}{q_x} - \frac{\omega^2}{c^2 q_x} \left(\int \frac{1}{q_1'^2} d\bar{q}_z + \frac{\int \frac{q_z}{q_1'^2} d\bar{q}_z}{\int \frac{q_z}{q_2'^2} d\bar{q}_z} \int \frac{1}{q_2'^2} d\bar{q}_z \right) \right]^{-1} \\
& \quad \times \left[\frac{q_x \int J_f(\bar{q}, \omega) \left(\frac{1}{q_1'^2} - \frac{1}{q_2'^2} \right) d\bar{q}_z}{\int \frac{1}{q_1'^2} d\bar{q}_z + \frac{\int \frac{q_z}{q_1'^2} d\bar{q}_z}{\int \frac{q_z}{q_2'^2} d\bar{q}_z} \int \frac{1}{q_2'^2} d\bar{q}_z} + \frac{q_x \int J_f(\bar{q}, \omega) q_z \left(\frac{1}{q_2'^2} - \frac{1}{q_1'^2} \right) d\bar{q}_z}{\int \frac{q_z}{q_2'^2} d\bar{q}_z \frac{\int \frac{1}{q_1'^2} d\bar{q}_z}{\int \frac{1}{q_2'^2} d\bar{q}_z} + \int \frac{q_z}{q_1'^2} d\bar{q}_z} \right. \\
& \quad + \frac{q_x \int J_f(\bar{q}, \omega) \left(\frac{1}{\varepsilon_2(\bar{q}, \omega) q_2'^2} - \frac{1}{\varepsilon_1(\bar{q}, \omega) q_1'^2} \right) d\bar{q}_z}{\int \frac{1}{\varepsilon_1(\bar{q}, \omega) q_1'^2} d\bar{q}_z + \frac{\int \frac{q_z}{q_1'^2} d\bar{q}_z}{\int \frac{q_z}{q_2'^2} d\bar{q}_z} \int \frac{1}{\varepsilon_2(\bar{q}, \omega) q_2'^2} d\bar{q}_z} \\
& \quad \left. - \frac{q_x \int J_f(\bar{q}, \omega) q_z \left(\frac{1}{q_2'^2} - \frac{1}{q_1'^2} \right) d\bar{q}_z}{\int \frac{q_z}{q_2'^2} d\bar{q}_z \frac{\int \frac{1}{\varepsilon_1(\bar{q}, \omega) q_1'^2} d\bar{q}_z}{\int \frac{1}{\varepsilon_2(\bar{q}, \omega) q_2'^2} d\bar{q}_z} + \int \frac{q_z}{q_1'^2} d\bar{q}_z} \right. \\
& \quad \left. - \frac{\int J_f(\bar{q}, \omega) \left(\frac{1}{q_1'^2} - \frac{1}{q_2'^2} \right) d\bar{q}_z}{\int \frac{1}{q_1'^2} d\bar{q}_z + \frac{\int \frac{q_z}{q_1'^2} d\bar{q}_z}{\int \frac{q_z}{q_2'^2} d\bar{q}_z} \int \frac{1}{q_2'^2} d\bar{q}_z} - \frac{\int J_f(\bar{q}, \omega) q_z \left(\frac{1}{q_2'^2} - \frac{1}{q_1'^2} \right) d\bar{q}_z}{\int \frac{q_z}{q_2'^2} d\bar{q}_z \frac{\int \frac{1}{q_1'^2} d\bar{q}_z}{\int \frac{1}{q_2'^2} d\bar{q}_z} + \int \frac{q_z}{q_1'^2} d\bar{q}_z} \right],
\end{aligned}$$

(3.52)

$$\begin{aligned}
& J_{s1,y}(\bar{Q}, \omega) \\
&= \left[q_x + \frac{q_y^2}{q_x} - \frac{\omega^2 \left(\int \frac{1}{q_1'^2} d\bar{q}_z + \frac{\int \frac{q_z}{q_1'^2} d\bar{q}_z}{\int \frac{q_z}{q_2'^2} d\bar{q}_z} \int \frac{1}{q_2'^2} d\bar{q}_z \right)}{\int \frac{1}{\varepsilon_1(\bar{q}, \omega) q_1'^2} d\bar{q}_z + \frac{\int \frac{q_z}{q_1'^2} d\bar{q}_z}{\int \frac{q_z}{q_2'^2} d\bar{q}_z} \int \frac{1}{\varepsilon_2(\bar{q}, \omega) q_2'^2} d\bar{q}_z} \right]^{-1} \\
&\times \left[\frac{q_y \int J_f(\bar{q}, \omega) \left(\frac{1}{q_1'^2} - \frac{1}{q_2'^2} \right) d\bar{q}_z}{\int \frac{1}{q_1'^2} d\bar{q}_z + \frac{\int \frac{q_z}{q_1'^2} d\bar{q}_z}{\int \frac{q_z}{q_2'^2} d\bar{q}_z} \int \frac{1}{q_2'^2} d\bar{q}_z} + \frac{q_y \int J_f(\bar{q}, \omega) q_z \left(\frac{1}{q_2'^2} - \frac{1}{q_1'^2} \right) d\bar{q}_z}{\int \frac{1}{q_1'^2} d\bar{q}_z + \frac{\int \frac{q_z}{q_1'^2} d\bar{q}_z}{\int \frac{q_z}{q_2'^2} d\bar{q}_z} \int \frac{1}{q_2'^2} d\bar{q}_z} \right. \\
&+ \frac{q_y \int J_f(\bar{q}, \omega) \left(\frac{1}{\varepsilon_2(\bar{q}, \omega) q_2'^2} - \frac{1}{\varepsilon_1(\bar{q}, \omega) q_1'^2} \right) d\bar{q}_z}{\int \frac{1}{\varepsilon_1(\bar{q}, \omega) q_1'^2} d\bar{q}_z + \frac{\int \frac{q_z}{q_1'^2} d\bar{q}_z}{\int \frac{q_z}{q_2'^2} d\bar{q}_z} \int \frac{1}{\varepsilon_2(\bar{q}, \omega) q_2'^2} d\bar{q}_z} \\
&\left. - \frac{q_y \int J_f(\bar{q}, \omega) q_z \left(\frac{1}{q_2'^2} - \frac{1}{q_1'^2} \right) d\bar{q}_z}{\int \frac{q_z}{q_2'^2} d\bar{q}_z \frac{\int \frac{1}{\varepsilon_1(\bar{q}, \omega) q_1'^2} d\bar{q}_z}{\int \frac{1}{\varepsilon_2(\bar{q}, \omega) q_2'^2} d\bar{q}_z} + \int \frac{q_z}{q_1'^2} d\bar{q}_z} \right], \tag{3.53}
\end{aligned}$$

$$J_{s2,x}(\bar{Q}, \omega) = -J_{s1,x}(\bar{Q}, \omega) \frac{\int \frac{q_z}{q_1'^2} d\bar{q}_z}{\int \frac{q_z}{q_2'^2} d\bar{q}_z} - \frac{\int J_f(\bar{q}, \omega) q_z \left(\frac{1}{q_2'^2} - \frac{1}{q_1'^2} \right) d\bar{q}_z}{\int \frac{q_z}{q_2'^2} d\bar{q}_z}, \tag{3.54}$$

and

$$J_{s2,y}(\bar{Q}, \omega) = -\frac{\int \frac{q_z}{q_1'^2} d\bar{q}_z}{\int \frac{q_z}{q_2'^2} d\bar{q}_z} J_{s1,y}(\bar{Q}, \omega), \quad (3.55)$$

where $J_f(\bar{q}, \omega)$ is given by Eq. (3.47). Again, in order to simplify the integrations in Eqs. (3.52) and (3.53), the assumption of $\varepsilon(\bar{q}, \omega) \approx \varepsilon(\bar{Q}, \omega)$ (Yubero and Tougaard 1992; Yubero *et al.* 1996) is applied. Then Eqs. (3.52) ~ (3.55) can be re-expressed as, respectively,

$$J_{s1,x}(\bar{Q}, \omega) = 2\pi v \delta(\omega - q_x v) \exp(-d\tilde{Q}_1) \Lambda, \quad (3.56)$$

$$J_{s1,y}(\bar{Q}, \omega) = 2\pi v \delta(\omega - q_x v) \exp(-d\tilde{Q}_1) \Gamma, \quad (3.57)$$

$$J_{s2,x}(\bar{Q}, \omega) = -J_{s1,x}(\bar{Q}, \omega) - 2\pi v \delta(\omega - q_x v) [\exp(-d\tilde{Q}_2) - \exp(-d\tilde{Q}_1)], \quad (3.58)$$

and

$$J_{s2,y}(\bar{Q}, \omega) = -J_{s1,y}(\bar{Q}, \omega), \quad (3.59)$$

where

$$\Lambda = \frac{\frac{1}{\tilde{Q}_1} - \frac{1}{\tilde{Q}_2} + \frac{1}{\varepsilon_2(\bar{Q}, \omega)\tilde{Q}_2} - \frac{1}{\varepsilon_1(\bar{Q}, \omega)\tilde{Q}_1}}{\frac{1}{\tilde{Q}_1} + \frac{1}{\tilde{Q}_2} + \frac{1}{\varepsilon_1(\bar{Q}, \omega)\tilde{Q}_1} + \frac{1}{\varepsilon_2(\bar{Q}, \omega)\tilde{Q}_2}} - \frac{\frac{1}{\tilde{Q}_1} - \frac{1}{\tilde{Q}_2}}{1 + \frac{q_y^2}{q_x^2} - \frac{\frac{\omega^2}{c^2 q_x^2} \left(\frac{1}{\tilde{Q}_1} + \frac{1}{\tilde{Q}_2} \right)}{\frac{1}{\varepsilon_1(\bar{Q}, \omega)\tilde{Q}_1} + \frac{1}{\varepsilon_2(\bar{Q}, \omega)\tilde{Q}_2}}}, \quad (3.60)$$

and

$$\Gamma = \frac{\frac{1}{\tilde{Q}_1} - \frac{1}{\tilde{Q}_2} + \frac{1}{\varepsilon_2(\bar{Q}, \omega)\tilde{Q}_2} - \frac{1}{\varepsilon_1(\bar{Q}, \omega)\tilde{Q}_1}}{\frac{1}{\tilde{Q}_1} + \frac{1}{\tilde{Q}_2} + \frac{1}{\varepsilon_1(\bar{Q}, \omega)\tilde{Q}_1} + \frac{1}{\varepsilon_2(\bar{Q}, \omega)\tilde{Q}_2}} - \frac{\frac{q_x}{q_y} + \frac{q_y}{q_x} - \frac{\frac{\omega^2}{c^2 q_x q_y} \left(\frac{1}{\tilde{Q}_1} + \frac{1}{\tilde{Q}_2} \right)}{\left(\frac{1}{\varepsilon_1(\bar{Q}, \omega)\tilde{Q}_1} + \frac{1}{\varepsilon_2(\bar{Q}, \omega)\tilde{Q}_2} \right)}}{1}. \quad (3.61)$$

Here we let $\tilde{Q}_1 = \sqrt{Q^2 - \frac{\omega^2 \varepsilon_1(\bar{Q}, \omega)}{c^2}}$ and $\tilde{Q}_2 = \sqrt{Q^2 - \frac{\omega^2 \varepsilon_2(\bar{Q}, \omega)}{c^2}}$. By inserting Eqs. (3.56) ~ (3.59) into Eqs. (3.48) ~ (3.51), then the vector potentials and scalar potentials in media 1 and 2 can be obtained.

3.4.3 The Stopping Power and DIIMFP with Retardation Effect for Electrons Moving Parallel to an Interface

To calculate the stopping power with retardation effect of the electron, we have to calculate the induced vector and scalar potentials first. The induced vector and scalar potentials of interest can be obtained by removing the corresponding potentials for electrons moving in vacuum. The Fourier components of the vector potential in

vacuum can be determined using Eq. (3.42) with $\mu = 1$ and $\varepsilon(\bar{q}, \omega) = 1$, and then it is given by

$$\begin{aligned}\bar{A}_{ref}(\bar{q}, \omega) &= \frac{4\pi \bar{J}_f(\bar{q}, \omega)}{c \left(q^2 - \frac{\omega^2}{c^2} \right)} \\ &= \frac{4\pi \bar{J}_f(\bar{q}, \omega)}{cq_0'^2} \quad , \\ &= \frac{4\pi}{cq_0'^2} \begin{bmatrix} \hat{x} & \hat{y} & \hat{z} \end{bmatrix} \begin{bmatrix} J_f(\bar{q}, \omega) \\ 0 \\ 0 \end{bmatrix}\end{aligned}\quad (3.62)$$

where we let $q_0'^2 = q^2 - \frac{\omega^2}{c^2}$. Substituting Eq. (3.62) into Eq. (3.41), the Fourier components of the scalar potential in vacuum can be given by

$$\begin{aligned}\Phi_{ref}(\bar{q}, \omega) &= \frac{c}{\omega} \bar{q} \cdot \bar{A}_{ref}(\bar{q}, \omega) \\ &= \frac{4\pi q_x}{\omega q_0'^2} J_f(\bar{q}, \omega)\end{aligned}\quad (3.63)$$

Through Eqs. (3.48) and (3.62), thus the Fourier component of the induced vector potential in medium 1, can be given by

$$\begin{aligned}\bar{A}_{ind}(\bar{q}, \omega) &= \bar{A}_1(\bar{q}, \omega) - \bar{A}_{ref}(\bar{q}, \omega) \quad . \\ &= \frac{4\pi}{cq_1'^2} \begin{bmatrix} \hat{x} & \hat{y} & \hat{z} \end{bmatrix} \begin{bmatrix} J_f(\bar{q}, \omega) + (\bar{Q}, \omega) \\ J_{s1,y}(\bar{Q}, \omega) \\ 0 \end{bmatrix} - \frac{4\pi}{cq_0'^2} \begin{bmatrix} \hat{x} & \hat{y} & \hat{z} \end{bmatrix} \begin{bmatrix} J_f(\bar{q}, \omega) \\ 0 \\ 0 \end{bmatrix}\end{aligned}\quad (3.64)$$

Likewise, through Eqs. (3.50) and (3.63), the induced scalar potential in medium 1

can be given by

$$\begin{aligned}
& \Phi_{ind}(\vec{q}, \omega) \\
&= \Phi_1(\vec{q}, \omega) - \Phi_{ref}(\vec{q}, \omega) \quad . \quad (3.65) \\
&= \frac{4\pi}{\omega \varepsilon_1(\vec{q}, \omega) q_1'^2} \left[q_x J_f(\vec{q}, \omega) + q_x J_{s1,x}(\vec{Q}, \omega) + q_y J_{s1,y}(\vec{Q}, \omega) \right] - \frac{4\pi q_x}{\omega q_0'^2} J_f(\vec{q}, \omega)
\end{aligned}$$

Through Eqs. (3.64) and (3.65), we can obtain the Fourier component of the induced electric field in x -direction according to Eq. (3.37). That is,

$$\begin{aligned}
& E_{ind,x}(\vec{q}, \omega) \\
&= -iq_x \Phi_{ind}(\vec{q}, \omega) + i \frac{\omega}{c} A_{ind,x}(\vec{q}, \omega) \\
&= -iq_x \left\{ \frac{4\pi}{\omega \varepsilon_1(\vec{q}, \omega) q_1'^2} \left[q_x J_f(\vec{q}, \omega) + q_x J_{s1,x}(\vec{Q}, \omega) + q_y J_{s1,y}(\vec{Q}, \omega) \right] - \frac{4\pi q_x}{\omega q_0'^2} J_f(\vec{q}, \omega) \right\} \\
&+ i \frac{\omega}{c} \left\{ \frac{4\pi}{c q_1'^2} \left[J_f(\vec{q}, \omega) + J_{s1,x}(\vec{Q}, \omega) \right] - \frac{4\pi}{c q_0'^2} \left[J_f(\vec{q}, \omega) \right] \right\} \\
&= i4\pi J_f(\vec{q}, \omega) \left\{ -\frac{q_x^2}{\omega q_1'^2 \varepsilon_1(\vec{q}, \omega)} + \frac{\omega}{c^2 q_1'^2} - \frac{\omega}{c^2 q_0'^2} + \frac{q_x^2}{\omega q_0'^2} \right\} \\
&+ i4\pi J_{s1,x}(\vec{Q}, \omega) \left\{ -\frac{q_x^2}{\omega q_1'^2 \varepsilon_1(\vec{q}, \omega)} + \frac{\omega}{c^2 q_1'^2} \right\} \\
&- i4\pi J_{s1,y}(\vec{Q}, \omega) \frac{q_x q_y}{\omega q_1'^2 \varepsilon_1(\vec{q}, \omega)} \quad (3.66)
\end{aligned}$$

where $J_f(\vec{q}, \omega)$, $J_{s1,x}(\vec{Q}, \omega)$ and $J_{s1,y}(\vec{Q}, \omega)$ are given by Eqs. (3.47), (3.56) and (3.57), respectively. In section 3.2.2, we have used Eq. (3.16) to calculate the stopping power of the moving electron. However, this expression for stopping power does not consider the contribution of the induced vector potential. Thus we applied the relation between the induced electric field and the stopping power. That

is, the stopping power can be determined from the induced electric force, parallel to the electron's moving direction, acting on the electron (Ritchie 1957; Abril *et al.* 1998; García-Molina *et al.* 1985), i.e.

$$-\frac{dW}{ds} = \mathbf{E}_{ind,x}(\vec{r}, t) \Big|_{\vec{r}=(vt,0,-d)}, \quad (3.67)$$

Then through Eqs. (3.66) and (3.67) and the principles of the inverse Fourier transform, the stopping power with retardation effect for the electron moving in medium 1 and parallel to the interface is given by

$$\begin{aligned} & -\frac{dW}{ds} \\ &= \frac{1}{(2\pi)^4} \iint \bar{\mathbf{E}}_{ind,x}(\vec{q}, \omega) \exp[i(q_x v - \omega)t] \exp[-iq_z d] d\omega d\vec{q} \\ &= \frac{-iv}{2\pi^2} \iiint \int \omega q^2 \sin \theta \exp[i(qv \sin \theta \cos \phi - \omega)t] \delta(\omega - qv \sin \theta \cos \phi) \\ & \times \left\{ \exp[-iqd \cos \theta] \exp(-d\tilde{Q}_1) \left[\Lambda \left(-\frac{q^2 \sin^2 \theta \cos^2 \phi}{\omega^2 q_1'^2 \varepsilon_1(\vec{q}, \omega)} + \frac{1}{c^2 q_1'^2} \right) - \Gamma \frac{q^2 \sin^2 \theta \cos \phi \sin \phi}{\omega^2 q_1'^2 \varepsilon_1(\vec{q}, \omega)} \right] \right. \\ & \quad \left. - \frac{q^2 \sin^2 \theta \cos^2 \phi}{\omega^2 q_1'^2 \varepsilon_1(\vec{q}, \omega)} + \frac{1}{c^2 q_1'^2} - \frac{1}{c^2 q_0'^2} + \frac{q^2 \sin^2 \theta \cos^2 \phi}{\omega^2 q_0'^2} \right\} d\omega dq d\theta d\phi \end{aligned} \quad (3.68)$$

where the spherical coordinates are adopted for the integration of the momentum transfer \vec{q} , and thus, with $Q = q \sin \theta$, the forms of Λ and Γ for momentum transfer in spherical coordinates become

$$\Lambda = \frac{\frac{1}{\tilde{Q}_1} - \frac{1}{\tilde{Q}_2} + \frac{1}{\varepsilon_2(\bar{Q}, \omega)\tilde{Q}_2} - \frac{1}{\varepsilon_1(\bar{Q}, \omega)\tilde{Q}_1}}{\frac{1}{\tilde{Q}_1} + \frac{1}{\tilde{Q}_2} - \frac{1}{\varepsilon_1(\bar{Q}, \omega)\tilde{Q}_1} + \frac{1}{\varepsilon_2(\bar{Q}, \omega)\tilde{Q}_2}} - \frac{\frac{1}{\tilde{Q}_1} - \frac{1}{\tilde{Q}_2}}{1 + \frac{\sin^2 \phi}{\cos^2 \phi} - \frac{c^2 q^2 \sin^2 \theta \cos^2 \phi \left(\frac{1}{\tilde{Q}_1} + \frac{1}{\tilde{Q}_2} \right)}{\frac{1}{\varepsilon_1(\bar{Q}, \omega)\tilde{Q}_1} + \frac{1}{\varepsilon_2(\bar{Q}, \omega)\tilde{Q}_2}}}, \quad (3.69)$$

and

$$\Gamma = \frac{\frac{1}{\tilde{Q}_1} - \frac{1}{\tilde{Q}_2} + \frac{1}{\varepsilon_2(\bar{Q}, \omega)\tilde{Q}_2} - \frac{1}{\varepsilon_1(\bar{Q}, \omega)\tilde{Q}_1}}{\frac{1}{\tilde{Q}_1} + \frac{1}{\tilde{Q}_2} - \frac{1}{\varepsilon_1(\bar{Q}, \omega)\tilde{Q}_1} + \frac{1}{\varepsilon_2(\bar{Q}, \omega)\tilde{Q}_2}} \cdot \frac{\cos \phi}{\sin \phi} + \frac{\sin \phi}{\cos \phi} - \frac{\omega^2}{c^2 q^2 \sin^2 \theta \cos \phi \sin \phi} \left(\frac{1}{\tilde{Q}_1} + \frac{1}{\tilde{Q}_2} \right) \left(\frac{1}{\varepsilon_1(\bar{Q}, \omega)\tilde{Q}_1} + \frac{1}{\varepsilon_2(\bar{Q}, \omega)\tilde{Q}_2} \right)}. \quad (3.70)$$

After the integration with respect to ϕ and some algebra, Eq. (3.68) is further given

by

$$-\frac{dW}{ds} = \frac{4v}{\pi^2} \int_0^E d\omega \int_{q=q_-}^{q_+} dq \int_{\theta=\sin^{-1} \frac{\omega}{qv}}^{\frac{\pi}{2}} d\theta \frac{\omega q^2 \sin \theta}{\sqrt{q^2 v^2 \sin^2 \theta - \omega^2}} \operatorname{Im} \left\{ -\frac{1}{v^2 q_1'^2 \varepsilon_1(\bar{q}, \omega)} + \frac{1}{c^2 q_1'^2} + \cos(qd \cos \theta) \exp(-d\tilde{Q}_1) \left[\Lambda \left(-\frac{1}{v^2 q_1'^2 \varepsilon_1(\bar{q}, \omega)} + \frac{1}{c^2 q_1'^2} \right) - \Gamma \frac{\sqrt{q^2 \frac{v^2}{\omega^2} \sin^2 \theta - 1}}{v^2 q_1'^2 \varepsilon_1(\bar{q}, \omega)} \right] \right\}. \quad (3.71)$$

where Λ and Ψ are also further given by, respectively,

$$\Lambda = \frac{\frac{\frac{1}{\tilde{Q}_1} - \frac{1}{\tilde{Q}_2}}{\frac{1}{\tilde{Q}_1} + \frac{1}{\tilde{Q}_2}} + \frac{\frac{1}{\varepsilon_2(\bar{Q}, \omega)\tilde{Q}_2} - \frac{1}{\varepsilon_1(\bar{Q}, \omega)\tilde{Q}_1}}{\frac{1}{\varepsilon_1(\bar{Q}, \omega)\tilde{Q}_1} + \frac{1}{\varepsilon_2(\bar{Q}, \omega)\tilde{Q}_2}}}{1 + \frac{q^2 v^2 \sin^2 \theta - \omega^2}{\omega^2} - \frac{\frac{v^2 \left(\frac{1}{\tilde{Q}_1} + \frac{1}{\tilde{Q}_2} \right)}{c^2}}{\left(\frac{1}{\varepsilon_1(\bar{Q}, \omega)\tilde{Q}_1} + \frac{1}{\varepsilon_2(\bar{Q}, \omega)\tilde{Q}_2} \right)}} - \frac{\frac{1}{\tilde{Q}_1} - \frac{1}{\tilde{Q}_2}}{\frac{1}{\tilde{Q}_1} + \frac{1}{\tilde{Q}_2}}, \quad (3.72)$$

and

$$\Gamma = \frac{\frac{\frac{1}{\tilde{Q}_1} - \frac{1}{\tilde{Q}_2}}{\frac{1}{\tilde{Q}_1} + \frac{1}{\tilde{Q}_2}} + \frac{\frac{1}{\varepsilon_2(\bar{Q}, \omega)\tilde{Q}_2} - \frac{1}{\varepsilon_1(\bar{Q}, \omega)\tilde{Q}_1}}{\frac{1}{\varepsilon_1(\bar{Q}, \omega)\tilde{Q}_1} + \frac{1}{\varepsilon_2(\bar{Q}, \omega)\tilde{Q}_2}}}{\frac{1}{\sqrt{q^2 \frac{v^2}{\omega^2} \sin^2 \theta - 1}} + \sqrt{q^2 \frac{v^2}{\omega^2} \sin^2 \theta - 1} - \frac{\frac{v^2}{c^2} \sqrt{q^2 \frac{v^2}{\omega^2} \sin^2 \theta - 1} \left(\frac{1}{\tilde{Q}_1} + \frac{1}{\tilde{Q}_2} \right)}{\left(\frac{1}{\varepsilon_1(\bar{Q}, \omega)\tilde{Q}_1} + \frac{1}{\varepsilon_2(\bar{Q}, \omega)\tilde{Q}_2} \right)}}. \quad (3.73)$$

By obeying the mass-energy and momentum conservations (Beiser 2003), the upper and lower limits of the integration with respect to q in Eq. (3.71) can be obtained by

$$q_{\pm} = \frac{\sqrt{E(E + 2c^2)} \pm \sqrt{(E - \omega)(E + 2c^2 - \omega)}}{c}. \quad (3.74)$$

The symbol E in Eqs. (3.71) and (3.74) denotes the relativistic kinetic energy of the electron. According to the relativistic theory, the relativistic kinetic energy is given by (Beiser 2003)

$$E = \frac{c^2}{\sqrt{1 - \frac{v^2}{c^2}}} - c^2. \quad (3.75)$$

Here this relation is utilized in Eqs. (3.71) and (3.74). After the stopping power $-\frac{dW}{ds}$ being derived, the corresponding DIIMFP with retardation effect can be determined according to Eq. (3.22). That is,

$$\begin{aligned} u(E, \omega, d) &= \frac{4v}{\pi^2} \int_{q=q_-}^{q_+} \int_{\theta=\sin^{-1} \frac{\omega}{qv}}^{\frac{\pi}{2}} \frac{q^2 \sin \theta}{\sqrt{q^2 v^2 \sin^2 \theta - \omega^2}} \operatorname{Im} \left\{ \frac{1}{v^2 q_1'^2 \varepsilon_1(\bar{q}, \omega)} + \frac{1}{c^2 q_1'^2} \right. \\ &\quad \left. + \cos(qd \cos \theta) \exp(-d\tilde{Q}_1) \left[\Lambda \left(-\frac{1}{v^2 q_1'^2 \varepsilon_1(\bar{q}, \omega)} + \frac{1}{c^2 q_1'^2} \right) - \Gamma \frac{\sqrt{q^2 \frac{v^2}{\omega^2} \sin^2 \theta - 1}}{v^2 q_1'^2 \varepsilon_1(\bar{q}, \omega)} \right] \right\} dq d\theta \end{aligned} \quad (3.76)$$

The non-retarded limit of Eq. (3.71) can be determined by letting $c \rightarrow \infty$. Then the stopping power without retardation effect for electrons moving parallel to an interface can be given by

$$\begin{aligned}
& u(E, \omega, d) \Big|_{c \rightarrow \infty} \\
&= \frac{-4}{\pi^2 v} \int_{q=q_-}^{q_+} dq \int_{\theta=\sin^{-1} \frac{|\omega|}{qv}}^{\frac{\pi}{2}} d\theta \frac{\sin \theta}{\sqrt{q^2 v^2 \sin^2 \theta - \omega^2}} \operatorname{Im} \left\{ \frac{1}{\varepsilon_1(\bar{q}, \omega)} \right. \\
&\quad \left. + \frac{\cos(qd \cos \theta) \exp(-dQ)}{\varepsilon_1(\bar{q}, \omega)} \frac{\frac{1}{\varepsilon_2(\bar{q}, \omega)} - \frac{1}{\varepsilon_1(\bar{q}, \omega)}}{\frac{1}{\varepsilon_2(\bar{q}, \omega)} + \frac{1}{\varepsilon_1(\bar{q}, \omega)}} \right\}, \tag{3.77}
\end{aligned}$$

where $q_{\pm} = \sqrt{2E} \pm \sqrt{2E - 2\omega}$ and E is given by Eq. (3.75). This obtained expression is the same as the formula derived previously for electrons of low and intermediate energies moving parallel to a solid surface (Kwei *et al.* 2003; Hsu 2003).

3.4.4 Comparisons between the Model without Retardation Effect and the Model with Retardation Effect for Electrons Moving Parallel to a Solid Surface

Figure 3.17 shows the comparison of the DIIMFPs without retardation effect (solid curve) and with retardation effect (dashed curve) for electrons of energy 1000 eV moving in vacuum at depth $z = -1 \overset{\circ}{\text{A}}$ and parallel to a Cu surface. The same comparison for electrons of energy 10^6 eV is plotted in Fig. 3.18. Here these results were calculated using Eqs. (3.76) and (3.77) with the extended dielectric functions of vacuum and Cu (Kwei *et al.* 1993) substituted respectively for $\varepsilon_1(\bar{q}, \omega)$ and $\varepsilon_2(\bar{q}, \omega)$. In Figs. 3.17 and 3.18, it is found that the DIIMFPs without and with retardation effect for 1000 eV electrons can not be distinguished, whereas the difference is substantial for 10^6 eV electrons, which indicates that the model with retardation effect should be applied to deal with the problem of inelastic interaction between high-energy electrons and solids.

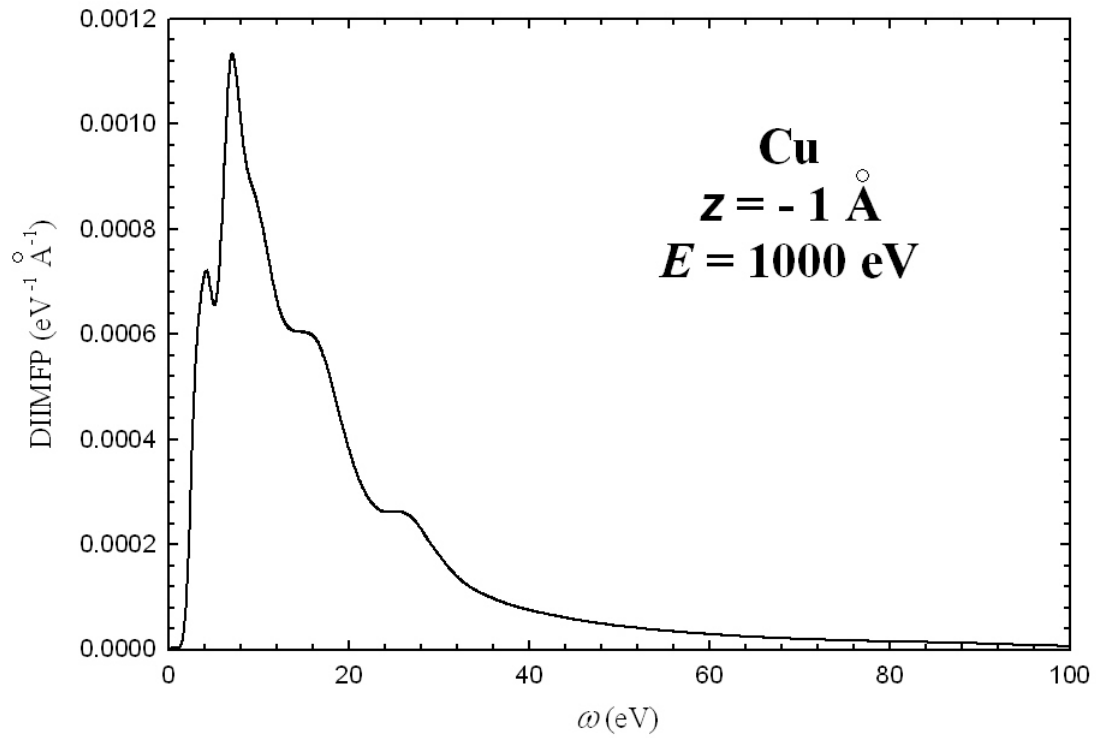


Fig. 3.17 A comparison of the DIIMFPs without retardation effect (solid curve) and with retardation effect (dashed curve) for electrons of energy 1000 eV moving in vacuum at depth $z = -1 \text{ \AA}$ and parallel to a Cu surface.

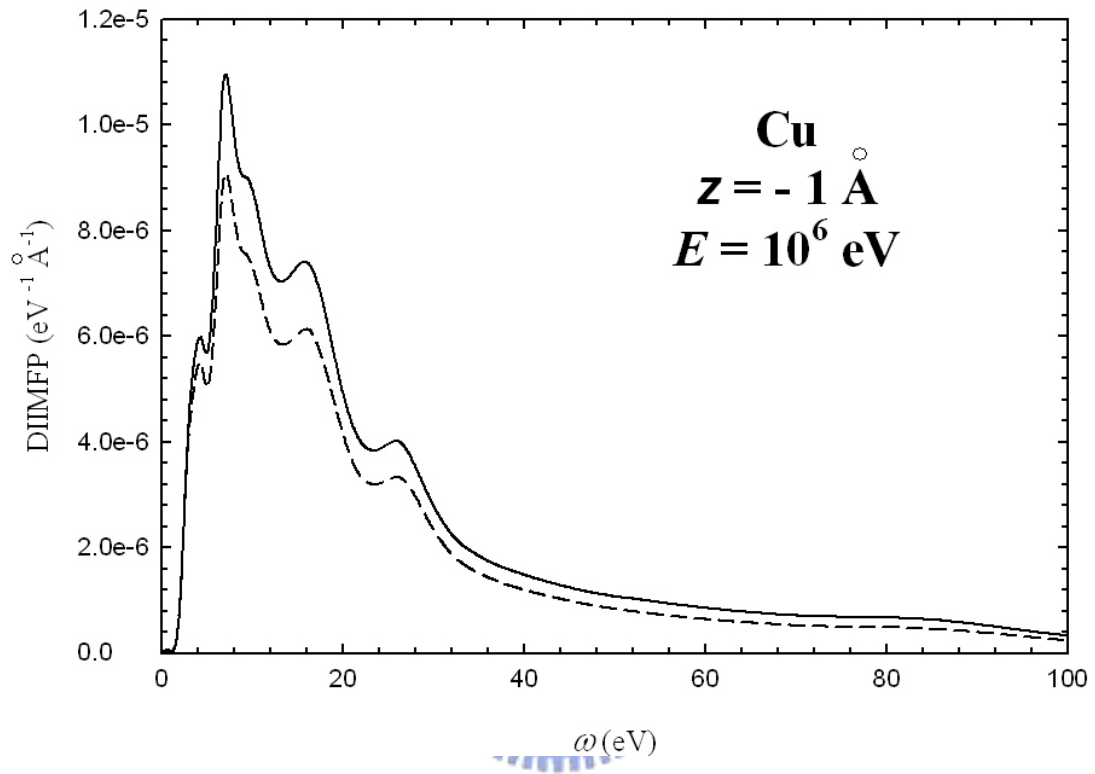


Fig. 3.18 A comparison of the DIIMFPs without retardation effect (solid curve) and with retardation effect (dashed curve) for electrons of energy 10^6 eV moving in vacuum at depth $z = -1 \text{ \AA}$ and parallel to a Cu surface.

Through the integration of the DIIMFP with respect to the energy loss ω , the IMFP can be determined. In Fig 3.19, we displayed the calculated IMFPs without retardation effect (solid curve) and with retardation effect (dashed curve) versus electron energy for electrons moving in vacuum at depth $z = -1\text{\AA}$ and parallel to a Cu surface. It can be seen that the values of the IMFP with retardation effect are reduced to the results of the IMFP without retardation effect for smaller electron energy. The difference between the IMFPs without and with retardation effect increases with increasing energy. Thus, the retardation effect becomes significant for high-energy electrons. Moreover, the curves of the IMFPs without and with retardation effect tend to saturate at very high energy. This is due to the fact that the velocity of the electron is close to the velocity of light. No matter how large the kinetic energy of the electron is, the velocity of the electron never exceeds the velocity of light. As a consequence, the value of IMFP gradually approaches to the value for electrons moving with velocity of light.

Using Eq. (3.71), we calculated the stopping powers with retardation effect for the electron of various energies moving in vacuum at $z = -1\text{\AA}$ and parallel to a Cu surface. The calculated results are plotted in Fig. 3.20. For comparison, the stopping powers without retardation effect are also included in this figure. It can be found that the stopping powers without and with retardation effect agree with each other for energy less than 10^5 eV, while the discrepancy can be seen for larger energy. Besides, both curves saturates at very high energy, as the same effect seen in Figs. 3.19 for IMFPs. It also can be found that the stopping powers decrease with the increasing energy of the electron. This is due to the induced excitations are less probable for higher energy.

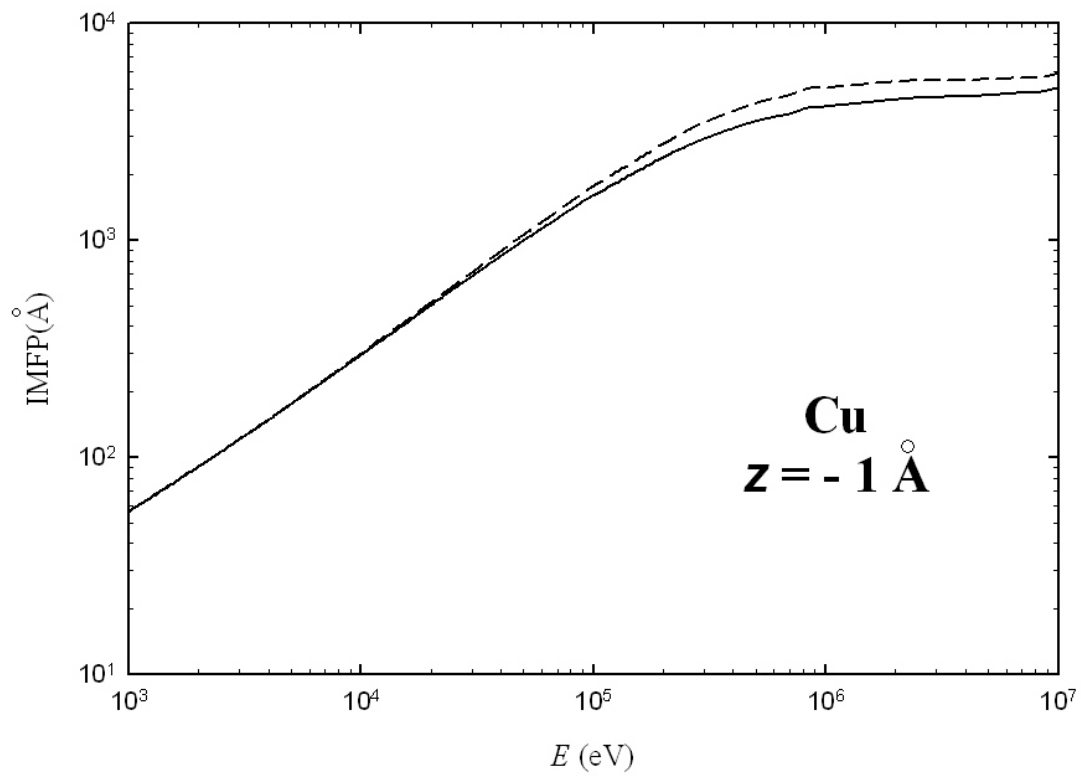


Fig. 3.19 A comparison of the IMFPs without retardation effect (solid curve) and with retardation effect (dashed curve) versus energy for electrons moving in vacuum at depth $z = -1 \text{ \AA}$ and parallel to a Cu surface.

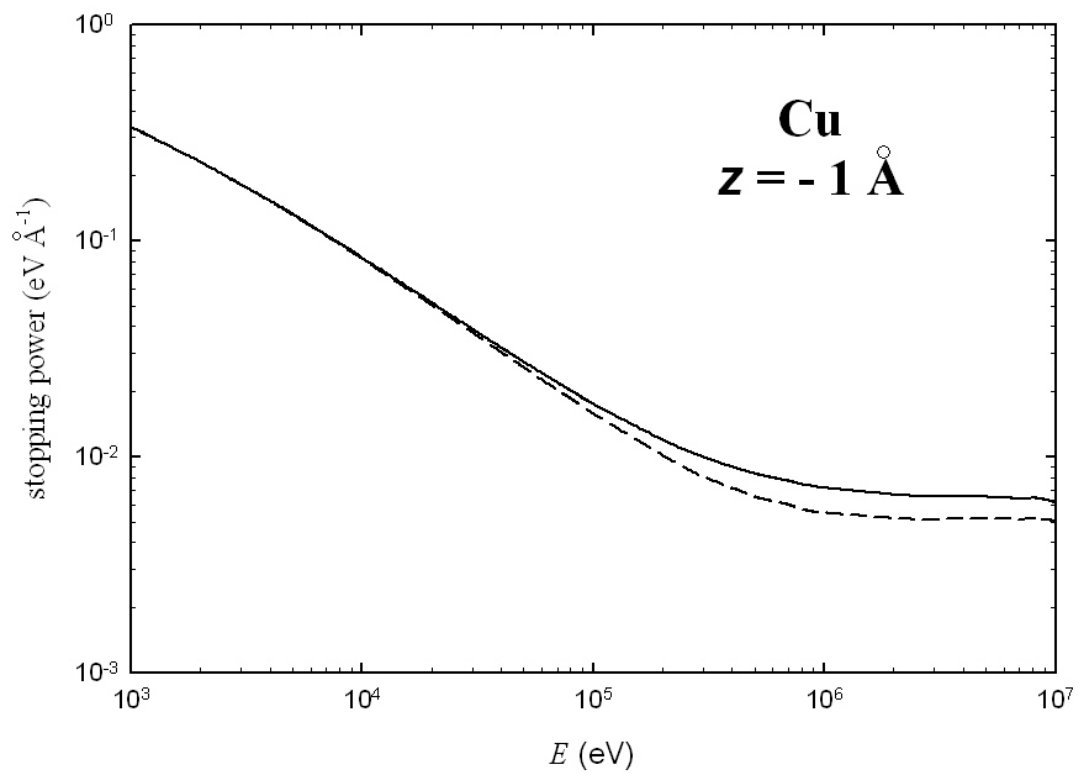


Fig. 3.20 A comparison of the stopping powers without retardation effect (solid curve) and with retardation effect (dashed curve) versus energy for electrons moving in vacuum at depth $z = -1 \text{ \AA}$ and parallel to a Cu surface.

CHAPTER 4

ELECTRON QUASI-ELASTIC PEAK

Elastic peak electron spectroscopy (EPES) has been frequently used to investigate the elastic peak spectra of electrons backscattered from solid surfaces. Some significant information like IMFP of electrons could be extracted from the analysis of the elastic peaks (Krawczyk *et al.* 1998; Zommer *et al.* 1998; Gergely *et al.* 1981, 1999; Lesiak *et al.* 1999; Tanuma *et al.* 2000). The energy distribution of the elastic peak spectra were also observed experimentally in the work with electron spectrometers (Boersch *et al.* 1967; Erickson and Powell 1989; Laser and Seah 1993; Goto and Shimizu 1997). This energy distribution is due to the fact that the Rutherford-type recoil energy loss occurs after each elastic interaction between the electron and the atom in a solid (Boersch *et al.* 1967). The aim of this chapter is to simulate the energy distribution of the elastic peak spectra of electrons quasi-elastically backscattered from solid surfaces. For this simulation work, we modified the previously-constructed Monte Carlo (MC) method (Kwei *et al.* 1998a, 2001) with the inclusion of the recoil energy loss. In addition to the recoil energy loss, there are three effects can affect the experimentally measured energy distributions of elastic peaks. The three effects are the spectrometer energy resolution, the energy distribution of the primary electrons and the thermal motion of atoms (Tóth *et al.* 1998; Gergely *et al.* 2001; Sulyok *et al.* 2001; Varga *et al.* 2001). We also include these effects in the simulation for the energy spectra of elastic peaks.

Moreover, through the measured elastic peak of backscattered electrons, the IMFP of electrons in a solid can be determined experimentally (Krawczyk *et al.* 1998; Zommer *et al.* 1998; Gergely *et al.* 1981, 1999; Lesiak *et al.* 1999; Tanuma *et al.*

2000). In the present chapter, we also discussed this experimental approach.

4.1 Simulation for Energy Spectra of Electrons Quasi-elastically Backscattered from a Semi-infinite Solid

Recently, the MC method has been frequently employed to determine the angular distribution for electrons elastically backscattered from solids (Jablonski 1989; Jablonski *et al.* 1991, 1992, 1993). Due to the recoil energy losses as electrons scattered elastically by atomic nuclei, the energy distribution also characterizes the features of the elastic peak spectra of backscattered electrons. Although the energy loss in each elastic scattering event is very small, the accumulation of each energy loss can not be negligible (Erickson and Powell 1989). Thus, this kind of scattering is called quasi-elastic scattering. The recoil energy loss results in a small energy shift and a width broadening in the elastic peak spectra. In order to calculate the energy spectra of electrons quasi-elastically backscattered from solids, we also adopted the similar MC method of Kwei *et al.* (1998a, 2001).

4.1.1 The Monte Carlo Method

The energy distribution of quasi-elastically backscattered electrons is simulated using the MC method. Backscattered electrons are traced from their impinging points to emerging points by recording the trajectories only involving elastic scattering events. Electron trajectories are recorded through azimuthal scattering angles, polar scattering angles and the path lengths between two consecutive elastic scattering events. By generating the uniformly-distributed random numbers between 0 and 1, the azimuthal and polar scattering angles and the path lengths can be

determined. Note that both the azimuthal and polar scattering angles are relative to the electron direction before elastic scattering. The polar scattering angle θ after each elastic collision can be determined from a random number R_1 using

$$R_1 = \frac{2\pi \int_0^\theta \sin\theta' \left(\frac{d\sigma_e}{d\Omega'} \right) d\theta'}{\sigma_e}, \quad (4.1)$$

where $\frac{d\sigma_e}{d\Omega'}$ is the EDCS, and

$$\sigma_e = 2\pi \int_0^\pi \sin\theta' \left(\frac{d\sigma_e}{d\Omega'} \right) d\theta' \quad (4.2)$$

is the elastic cross section. It is assumed that the azimuthal scattering angle ϕ after each elastic collision is cylindrically symmetric with respect to the electron moving direction before elastic scattering (Kwei *et al.* 1997). As a result, the azimuthal scattering angle can be obtained from a random number R_2 according to

$$\phi = 2\pi R_2. \quad (4.3)$$

Applying the Poisson stochastic process for elastic scattering events, the probability density function of electrons moving along a straight step path length Δs_i between the i th elastic scattering at depth z_i and the $(i+1)$ th elastic scattering at depth z_{i+1} with $\Delta s_i = \frac{z_{i+1} - z_i}{\cos\Theta_i}$ is given by (Reimer 1985)

$$P(\Delta s_i) = \frac{1}{\lambda_e} \exp\left(-\frac{z_{i+1} - z_i}{\lambda_e \cos \Theta_i}\right), \quad (4.4)$$

where the form of the electron EMFP λ_e can be calculated according to Eq. (2.3), and Θ_i denotes the angle between the inwardly-directed surface normal and the electron moving direction after the i th elastic scattering. Eq. (4.4) can be related to a random number R_3 as the following expression (Su 1994):

$$R_3 = 1 - \int_0^{\Delta s_i} P(\Delta s') d\Delta s'. \quad (4.5)$$

By means of Eqs. (4.4) and (4.5), the length between z_i and z_{i+1} can be determined from R_3 by (Kwei *et al.* 2001)

$$z_{i+1} - z_i = -\lambda_e \cos \Theta_i \ln R_3. \quad (4.6)$$

The relation between Θ_i and Θ_{i-1} is given by (Kwei *et al.* 1997)

$$\cos \Theta_i = \cos \Theta_{i-1} \cos \theta_i - \sin \Theta_{i-1} \sin \theta_i \cos \phi_i, \quad (4.7)$$

where θ_i and ϕ_i are the i th polar and azimuthal scattering angles, respectively. When an elastic interaction occurs, electrons lose some energy. This is because the electron scattered by an atomic nucleus suffers the Rutherford-type recoil energy loss, as mentioned in section 2.6. According to Eq. (2.12), the energy of an electron after the i th elastic scattering with θ_i is given by

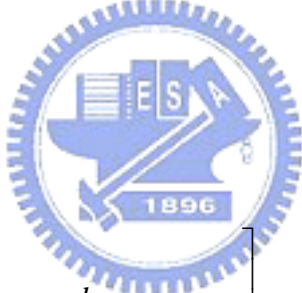
$$E_i(\theta_i) = \left(1 - \frac{4m}{M} \sin^2 \frac{\theta_i}{2}\right) E_{i-1}(\theta_{i-1}), \quad (4.8)$$

where $E_{i-1}(\theta_{i-1})$ is the electron energy after the $(i-1)$ th elastic scattering.

According to the Poisson stochastic process for inelastic scattering events, the probability density function that an electron travels Δs_i path length between the i th and the $(i+1)$ th elastic scatterings without inelastic scattering is

$$P_i = \exp \left[-\frac{1}{\cos \Theta_i} \int_{z_i}^{z_{i+1}} \frac{dz}{\lambda_i^{v \rightarrow s} \left(\Theta_i, E_i, \frac{z}{\cos \Theta_i} \right)} \right], \quad (4.9a)$$

or



$$P_i = \exp \left[-\frac{1}{\cos \Theta_i} \int_{z_i}^{z_{i+1}} \frac{dz}{\lambda_i^{s \rightarrow v} \left(\pi - \Theta_i, E_i, \frac{-z}{\cos \Theta_i} \right)} \right], \quad (4.9b)$$

where $\lambda_i^{v \rightarrow s} \left(\Theta_i, E_i, \frac{z}{\cos \Theta_i} \right)$ and $\lambda_i^{s \rightarrow v} \left(\pi - \Theta_i, E_i, \frac{-z}{\cos \Theta_i} \right)$, respectively, are the

IMFPs at depth z for electrons of energy E_i moving inward and outward inside the solid, and they can be calculated using Eqs. (3.26) ~ (3.29). Besides, the probability density function of an electron with energy E crossing the surface by a crossing angle α without surface excitations is determined from the use of the SEPs expressed in Eqs. (3.30) and (3.31) (Chen *et al.* 1994). Then the probability density function is given by

$$\exp\left[-P_s^{v \rightarrow s}(\alpha_1, E_1)\right], \quad \text{for incident electrons,} \quad (4.10a)$$

or

$$\exp\left[-P_s^{s \rightarrow v}(\alpha_R, E_R)\right], \quad \text{for backscattered electrons,} \quad (4.10b)$$

where α_1 and E_1 are the incident angle and the incident energy of the electron, respectively, and α_R and E_R are the emission angle within the acceptance angles and the emission energy of the electron, respectively. However, it is difficult using Eqs. (3.26) ~ (3.31) in Eqs. (4.9) and (4.10) to determine the probabilities since too much computing time must be taken. Thus, we made approximations to reduce the computing time. In Figs. 3.6 and 3.7, we can see that the inverse IMFP inside the solid could be roughly regarded as being isotropic. Therefore, to simplify the calculation for the MC simulation, we assumed that the values of IMFP inside the solid for all directions are equal to those for normally-incident and normally-escaping electrons (Kwei *et al.* 2001). Accordingly, the probability density function in Eq. (4.9) can be rewritten as

$$P_i = \exp\left[-\frac{1}{\cos\Theta_i} \int_{z_i}^{z_{i+1}} \frac{dz}{\lambda_i^{v \rightarrow s}(0, E_i, z)}\right], \quad (4.11a)$$

or

$$P_i = \exp \left[-\frac{1}{\cos \Theta_i} \int_{z_i}^{z_{i+1}} \frac{dz}{\lambda_i^{s \rightarrow v}(0, E_i, -z)} \right], \quad (4.11b)$$

where $\lambda_i^{v \rightarrow s}(0, E_i, z)$ and $\lambda_i^{s \rightarrow v}(0, E_i, -z)$, respectively, are the IMFPs for electrons of energy E_i normally moving inward and outward inside the solid, and they can be calculated through Eqs. (3.26) ~ (3.29) by taking $\alpha = 0^\circ$ or through the previous inelastic-scattering model (Kwei *et al.* 1998b). Besides, the fitting formula shown in Eq. (3.32) or the previous fitting formula, $\frac{aE^{-b}}{\cos \alpha}$, (Kwei *et al.* 1998b) were applied to calculate SEPs for Eq. (4.10).

By tracking the electrons until either they backscattered from the surface within acceptance angles or their paths in the solid become so large that the contributions to the intensity can be neglected. Then, the intensity of quasi-elastically backscattered electrons with energy E is given by

$$I(E) = \frac{1}{n} \sum_{j=1}^n \Delta I_j(E), \quad (4.12)$$

where $\Delta I_j(E)$ is the intensity of quasi-elastically backscattered electrons with energy E for the j th trajectory and n is the total number of sampled trajectories.

4.1.2 The Results Calculated Using Monte Carlo method

Figures 4.1 and 4.2 show the energy distributions of the elastic peaks contributed by one, two, three and all elastic scatterings for 5000 eV normally incident electrons backscattered from Si and Au, respectively. Here, in the MC simulation, the EDCSS for Si and Au are calculated using the relativistic model with the solid-atom potential

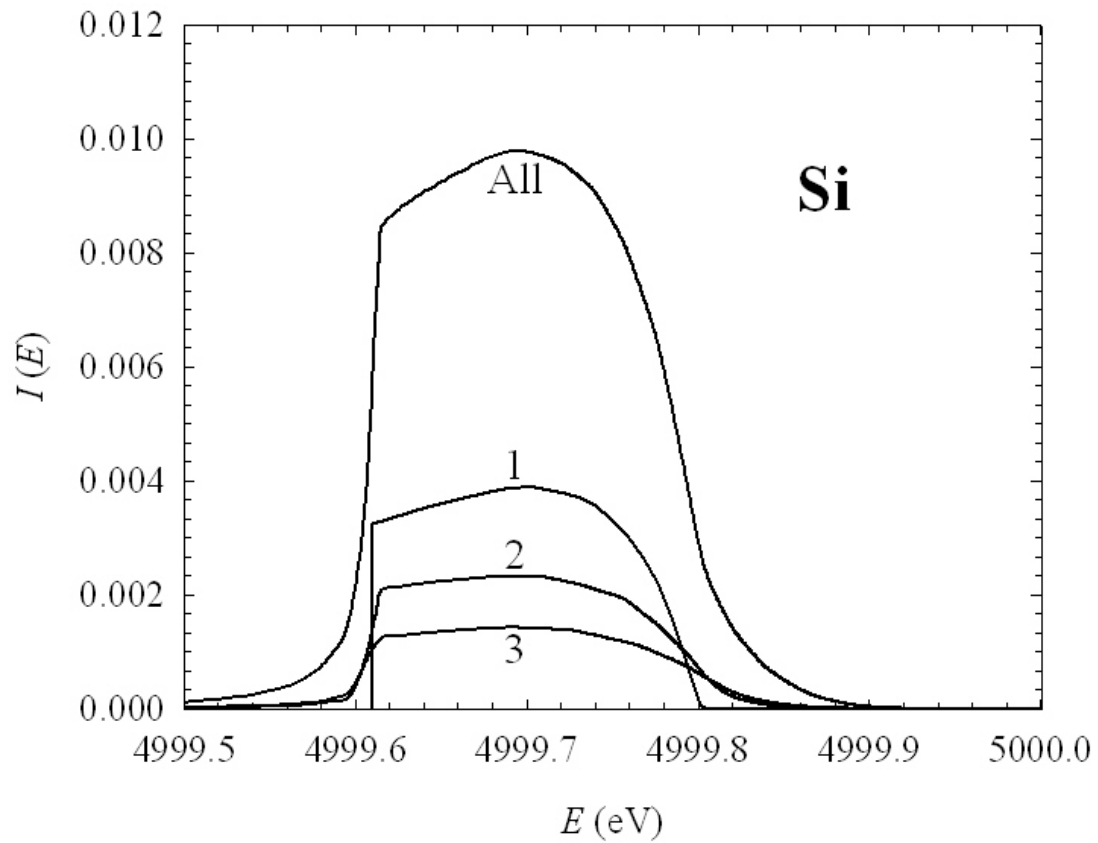


Fig. 4.1 A plot of the MC simulation results on the energy distribution of electrons quasi-elastically backscattered from Si for normally incident electrons of 5000 eV. Individual contributions from one, two, three and all elastic scatterings are plotted separately.

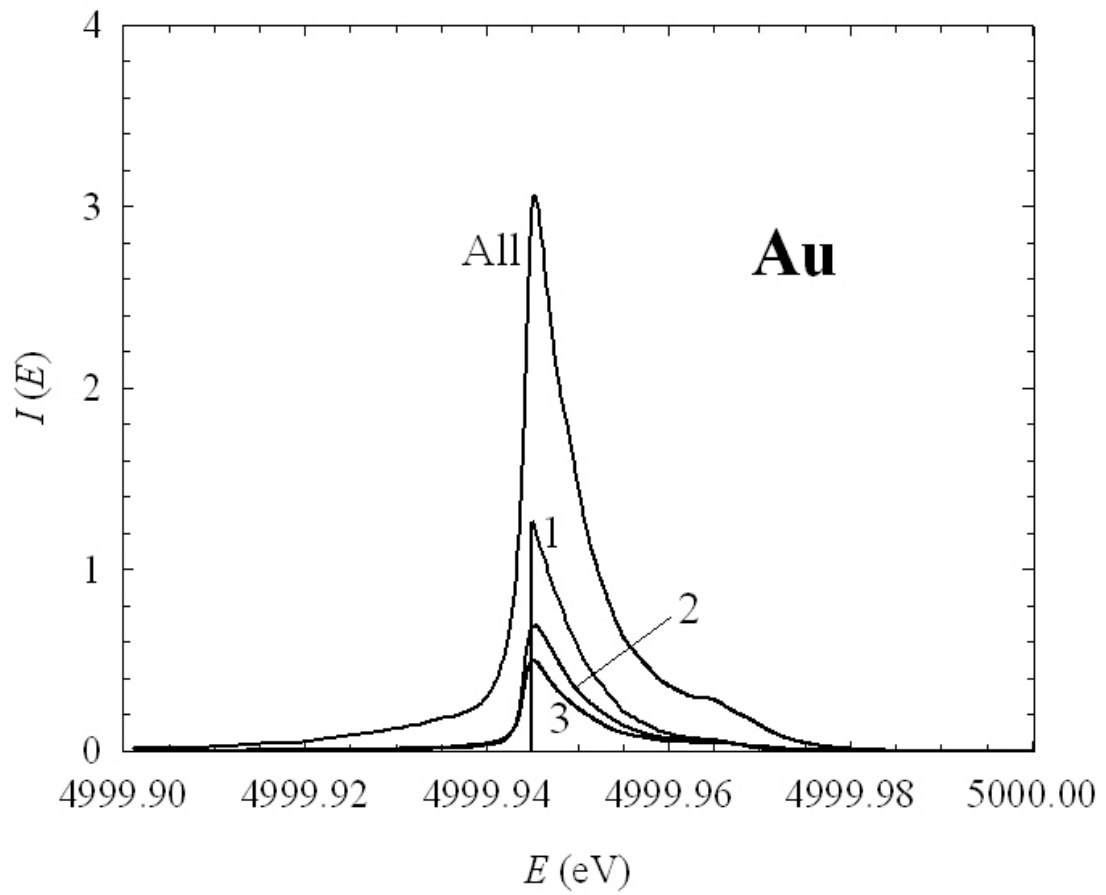


Fig. 4.2 A plot of the MC simulation results on the energy distribution of electrons quasi-elastically backscattered from Au for normally incident electrons of 5000 eV. Individual contributions from one, two, three and all elastic scatterings are plotted separately.

as mentioned in Chapter 2. The depth-dependent IMFPs for normally moving electrons, $\lambda_i^{v \rightarrow s}(0, E_i, z)$ and $\lambda_i^{s \rightarrow v}(0, E_i, -z)$, are calculated using the previous inelastic-scattering model (Kwei *et al.* 1998b), in which the extended Drude dielectric function derived from experimental optical data (Kwei *et al.* 1993) are adopted. The SEPs were calculated using the fitting formula of $\frac{aE^{-b}}{\cos\alpha}$ with the fitted values of parameters listed in the article of Kwei *et al.* (1998b). In these two figures, the small energy shifts and the width broadenings of the elastic peaks can be seen. In order to compare the energy spectra accounting for all elastic scatterings in Figs. 4.1 and 4.2, we plot them again in Fig. 4.3 (Si: dashed curve, Au: solid curve). The left ordinate is for Si and the right ordinate is for Au. It reveals that, for Au, the energy shift of the peak maximum is much smaller, and the recoil width broadening of the peak is narrower. From this finding, we can conclude that the energy loss is smaller for solids composed of heavier atoms as discussed in section 2.4. Besides, it can be found in Figs. 4.1 ~ 4.3 that the exact shapes of the elastic peaks depend strongly on the elastic scattering cross sections for different solids.

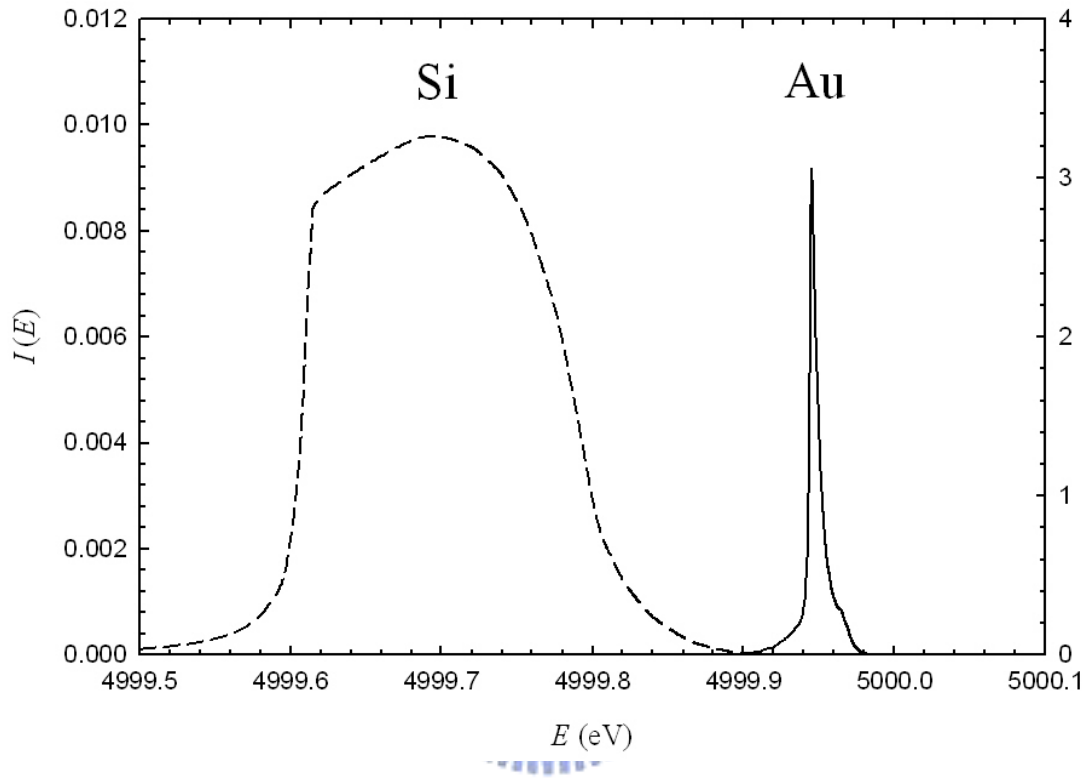


Fig. 4.3 A plot of the MC simulation results on the energy distribution of electrons quasi-elastically backscattered from Si and Au for normally incident electrons of 5000 eV. The left and right longitudinal axes are for Si and Au, respectively.

4.1.3 Adjustments to Energy Spectra of Quasi-elastically Backscattered Electrons

There are two experimental factors that affect the height and the width in the energy distribution of the electron elastic peak detected by a spectrometer (Tóth *et al.* 1998; Gergely *et al.* 2001; Sulyok *et al.* 2001). One is the energy distribution of the primary electron beam emitted from an electron gun. The other is the energy resolution of the analyzer of a spectrometer. To simulate the experimental results of elastic peak electron spectra, these two effects were considered in our MC algorithm for the energy distribution of backscattered electrons.

We assumed that both the energy distribution of the electron beam and the resolution function are Gaussian distributions. Let $G(\gamma; \gamma_0, \tau)$ be the Gaussian function of a variable γ with the mean value γ_0 and the standard deviation τ . Considering the Gaussian energy distribution of the primary electron beam, the energy distribution of quasi-elastically backscattered electrons before the measuring of the spectrometer can be expressed as

$$h(E) = \int_{-\infty}^{\infty} I(E - \omega + E_0) G(\omega; E_0, \tau_g) d\omega, \quad (4.13)$$

where E_0 is the mean energy of the primary electron beam and τ_g is the standard energy deviation of the energy distribution of the electron beam. By taking the further consideration of the energy resolution of the spectrometer, the energy distribution becomes

$$H(E) = \int_{-\infty}^{\infty} h(E')G(E; E', \tau_r) dE', \quad (4.14)$$

where τ_r is the standard energy deviation of the resolution function. Using Eqs. (4.13) and (4.14), the simulated quasi-elastic electron peak spectra is comparable with experimental data.

In Fig. 4.4, we plot the energy distributions of elastic peaks for electron beams normally incident into Si with 5000 eV mean energy and two different FWHMs, 0.3 eV and 0.5 eV. It can be seen that the spectra are broadened Gaussian peaks. As compared to the primary electron beams, the width broadenings in the two Gaussian peaks are arisen from the recoil width broadening displayed in Fig. 4.1. In addition, the FWHM of the resulting spectrum is wider when ΔE_g of the electron beam increases. Here ΔE_g is the FWHM of the energy distribution of the electron beam. A similar plot is shown in Fig. 4.5 for Au. The FWHM of the resulting spectrum for Au is obviously narrower than that for Si. This is because the recoil width broadening is much smaller for Au. Figures 4.6 and 4.7 show the energy distributions of the elastic peaks for Si and Au, respectively, using different spectrometer resolutions but the same Gaussian distributed normally incident electron beam with 0.3 eV FWHM and 5000 eV mean energy. The spectrometer function was assumed to be a Gaussian distribution with two different FWHMs, 0.3 eV and 0.5 eV. The results without the consideration of the energy resolution of the spectrometer are also included for comparison. It is found that all the spectra depend strongly on the spectrometer functions. The larger ΔE_s , the FWHM of the spectrometer function, results in the larger ΔE_t , the FWHM of the total spectrum.

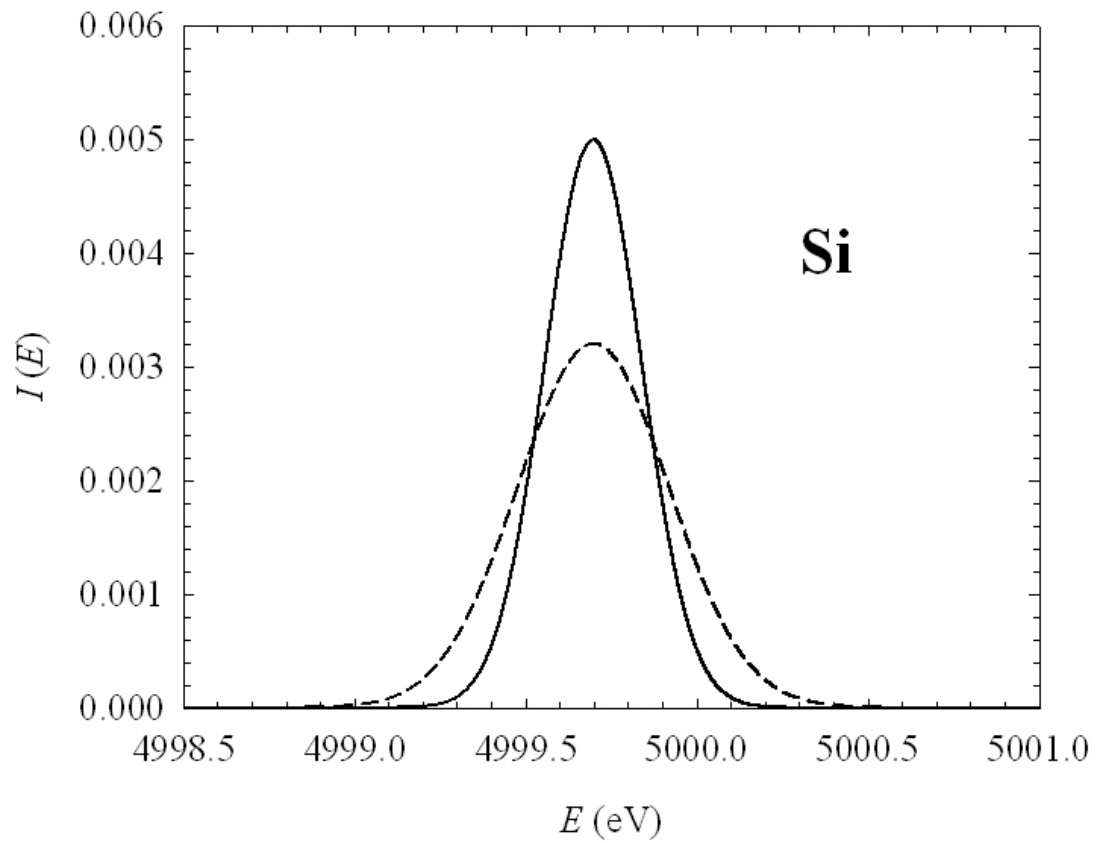


Fig. 4.4 A plot of the MC results on the energy spectra of electrons quasi-elastically backscattered from Si for normally incident electrons of 5000eV mean energy and 0.3 eV (solid curve) and 0.5 eV (dashed curve) FWHM.

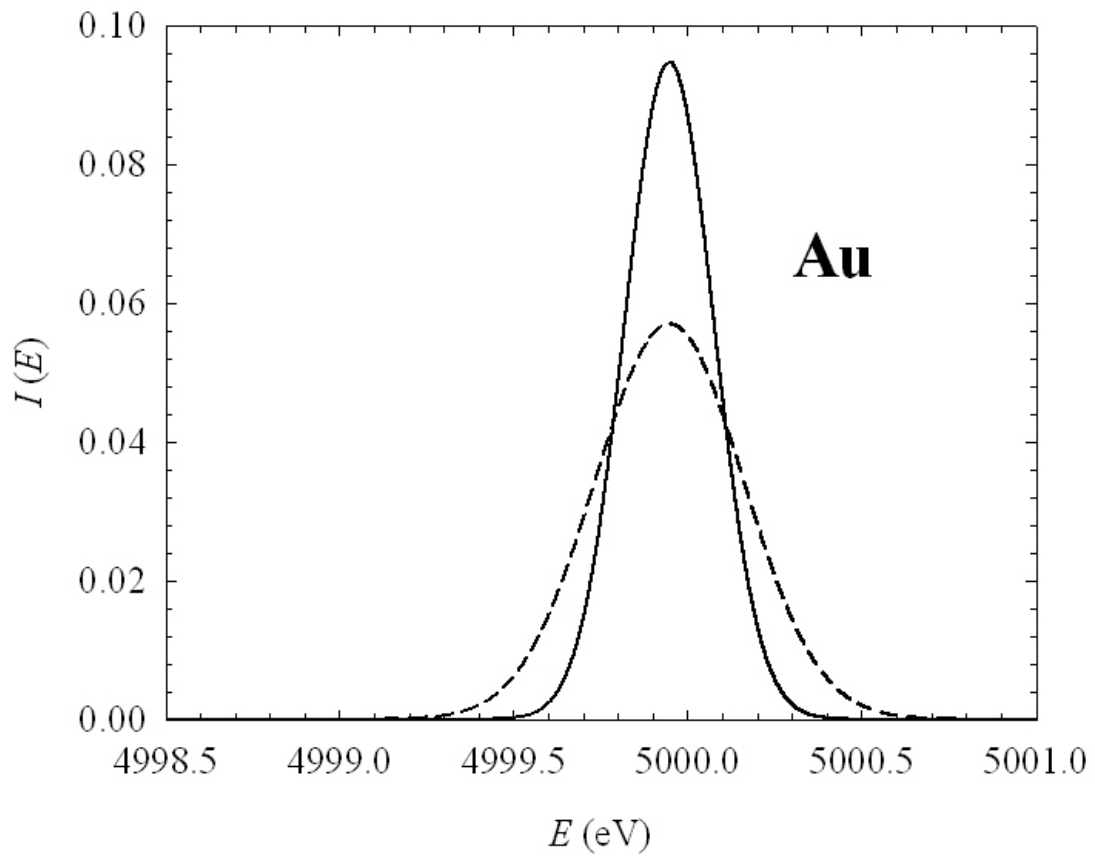


Fig. 4.5 A plot of the MC results on the energy spectra of electrons quasi-elastically backscattered from Au for normally incident electrons of 5000eV mean energy and 0.3 eV (solid curve) and 0.5 eV (dashed curve) FWHM.

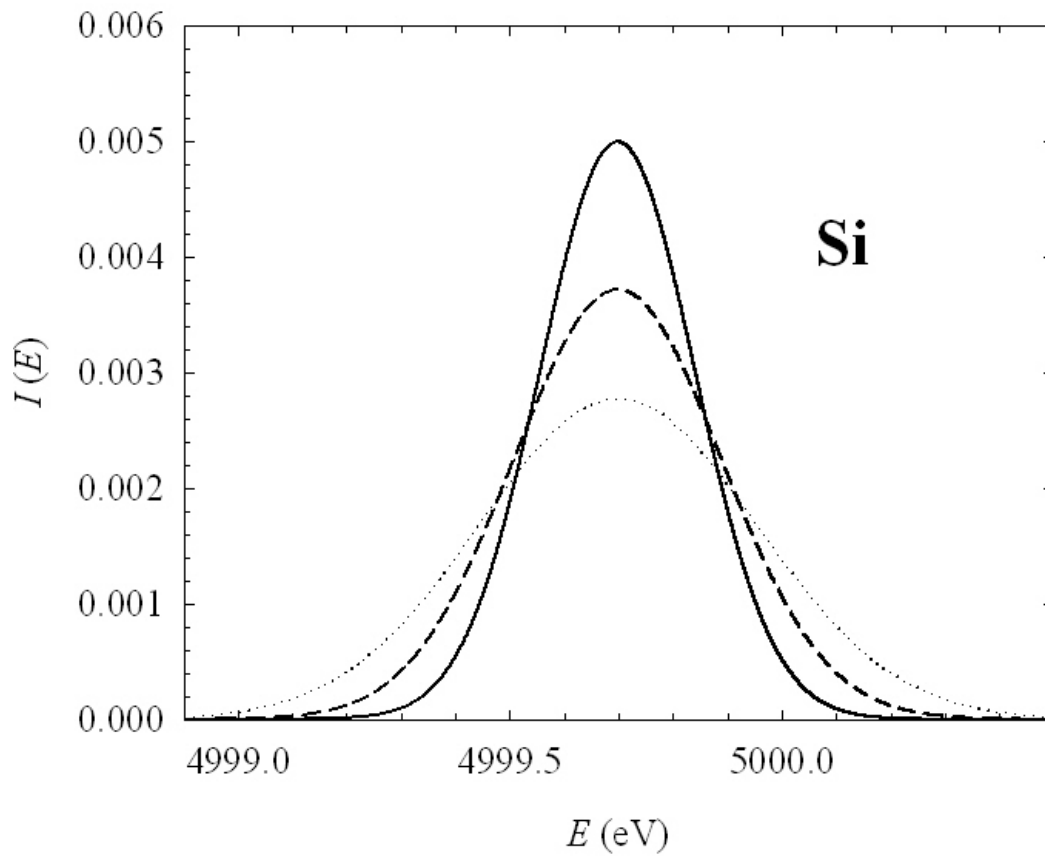


Fig. 4.6 A plot of the MC results on the energy spectra of electrons quasi-elastically backscattered from Si for normally incident electrons of 5000eV mean energy and 0.3 eV FWHM. The spectrometer resolutions are 0 eV (solid curve), 0.3 eV (dashed curve) and 0.5 eV (dotted curve).

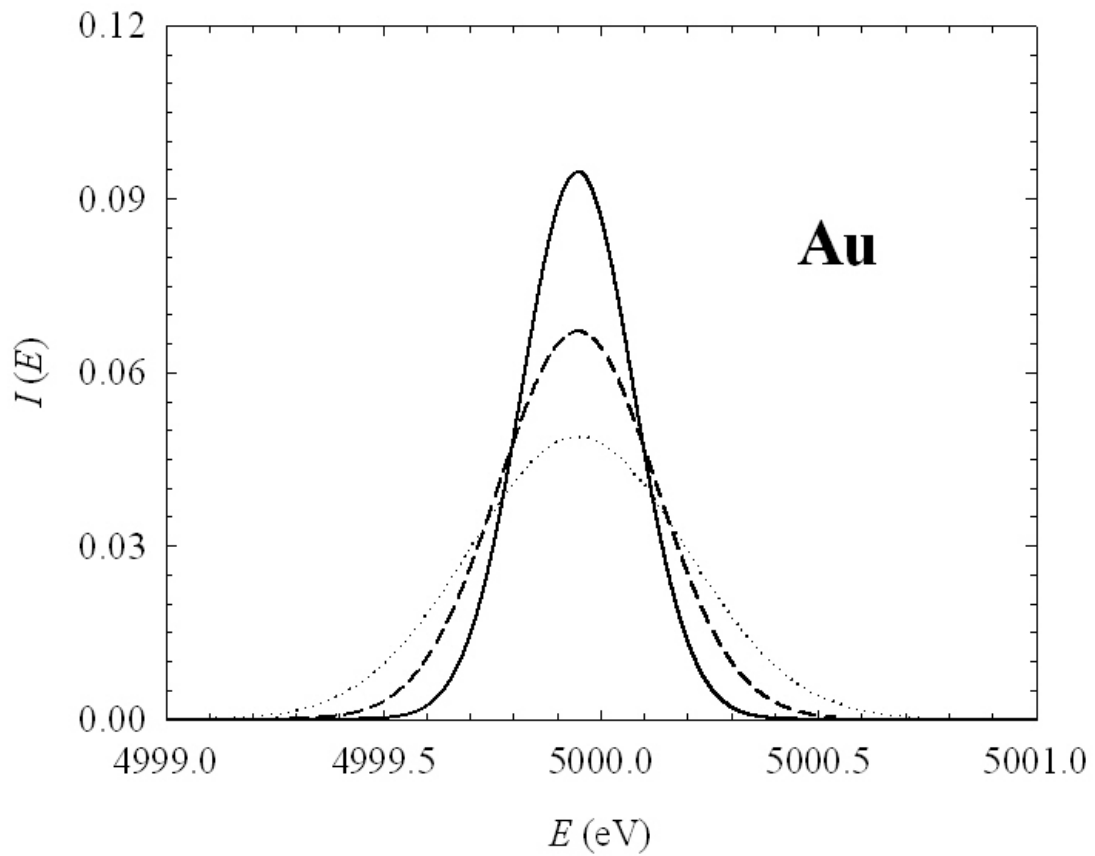


Fig. 4.7 A plot of the MC results on the energy spectra of electrons quasi-elastically backscattered from Au for normally incident electrons of 5000eV mean energy and 0.3 eV FWHM. The spectrometer resolutions are 0 eV (solid curve), 0.3 eV (dashed curve) and 0.5 eV (dotted curve).

It is seen that ΔE_t of the present calculated spectra are in good agreement with the approximation (Tóth *et al.* 1998; Gergely *et al.* 2001)

$$\Delta E_t = \sqrt{\Delta E_r^2 + \Delta E_g^2 + \Delta E_s^2}, \quad (4.15)$$

where ΔE_r is the FWHM of the recoil width broadening. For our case of 5000 eV normally incident electrons, ΔE_r is 0.18 eV for Si and 0.0048 eV for Au. ΔE_r is small in comparison with ΔE_g and ΔE_s used in our work. Therefore, all the spectra are almost Gaussian distributions so that the widths of the quasi-elastic elastic peaks are dominated by ΔE_g and ΔE_s . Figure 4.8 shows our calculated spectra without and with the consideration of the thermal corrections in the recoil losses. The experimental results (Varga *et al.* 2001) are included for comparison. Here the electron beam with 5000 eV mean energy and $\Delta E_g = 0.4$ eV was obliquely incident into Si. The incident angle was 50° . The acceptance angles were between 0° and 3° . The energy resolution of the spectrometer ΔE_s was 0.28 eV. The spectrum without the thermal effect is a Gaussian distribution with its maximum at 4999.69 eV and a FWHM of 0.5 eV (solid curve). For such narrow acceptance angles, the broadening is expected to be completely dominated by ΔE_g and ΔE_s . The spectrum including the thermal effect was calculated by applying the single scattering model (Varga *et al.* 2001). In this model, it was assumed that the recoil energy losses followed a Gaussian distribution with its maximum at the most probable recoil energy loss for atoms at rest. Here the thermal Gaussian function with its maximum at 4999.69 eV and a FWHM $\Delta E_r = 0.3$ eV was adopted for Si at room temperature.

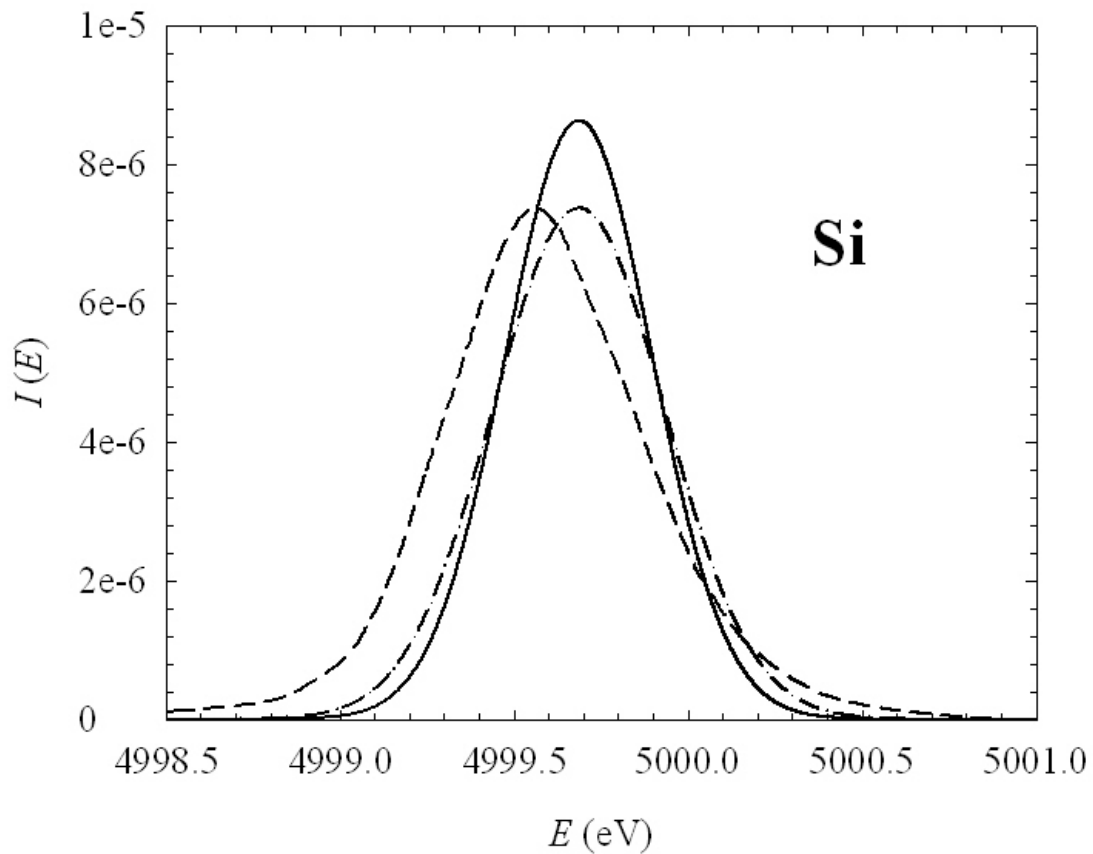


Fig. 4.8 A plot of the MC simulation results on the energy spectra of electrons quasi-elastically backscattered from Si for normally incident electrons of 5000 eV mean energy and 0.4 eV FWHM. Here electrons are incident at an angle 50° ; acceptance angles are between 0° and 3° ; the spectrometer resolution is 0.28 eV. The thermal effect of atoms is neglected (solid curve) and considered (dash-dot) by applying the single scattering model (Varga *et al.* 2001) with a FWHM of $\Delta E_T = 0.3$ eV at the room temperature. For comparison, the experimental data (dashed curve) (Varga *et al.* 2001) are also included.

The resulting spectrum with the thermal effect (dash-dot curve) is a Gaussian function with a FWHM of 0.58 eV. Then we can find that this FWHM, ΔE , is in good agreement with $\Delta E = \sqrt{\Delta E_T^2 + \Delta E_g^2 + \Delta E_s^2}$. However, the peak position is associated with the most probable recoil energy loss for the vibrating atoms, not for atoms at rest. In addition, the thermal effect in multiple scatterings shifts the peak position and widens the spectra. Thus, this simple model is not enough to describe the shift and the broadening. Owing to the experimental data (Varga *et al.* 2001) were in arbitrary units, the experimental data shown in the figure were adjusted in magnitude to match our expectation of absolute values.

4.1.4 Formula for Energy Spectra Contributed by Single-scattering Event

Based on the above mentioned algorithm of the MC simulation, we can obtain a formula that can calculate the energy distribution of quasi-elastically backscattered electrons suffering a single scattering in solids. This formula in a differential energy interval dE around energy E is given by

$$I_1(E)dE = \frac{M}{2mE_I} e^{-P_s(\alpha_I, E_I)} \int_{-\phi_A}^{\phi_A} \int_0^{\infty} \exp[-P_s(\alpha_R, E)] P_\Omega(\theta_1, \phi_1) F_I(z_1) F_R(z_1, \alpha_R) dz_1 d\phi_1 dE. \quad (4.16)$$

The value of ϕ_A is given by

$$\phi_A = \begin{cases} \cos^{-1}\left(\frac{\cos\beta + \cos\alpha_I \cos\theta_1}{\sin\alpha_I \sin\theta_1}\right), & \text{for } \pi - \alpha_I - \beta \leq \theta_1 \leq \pi - \alpha_I + \beta \text{ when } \beta \leq \alpha_I \\ \cos^{-1}\left(\frac{\cos\beta + \cos\alpha_I \cos\theta_1}{\sin\alpha_I \sin\theta_1}\right), & \text{for } \pi - \alpha_I - \beta \leq \theta_1 \leq \pi + \alpha_I - \beta \text{ when } \beta > \alpha_I \\ \pi, & \text{for } \pi + \alpha_I - \beta < \theta_1 \leq \pi \text{ when } \beta > \alpha_I, \end{cases} \quad (4.17)$$

where β is the largest acceptance angle of escape electrons relative to outwardly directed surface normal (i.e. $0 \leq \alpha_R \leq \beta$). $F_I(z_1)$ is the probability density function for electrons reaching the depth z_1 , at which the elastic scattering occurs, without any inelastic interaction and is given by

$$F_I(z_1) = \frac{1}{\lambda_e} \exp\left(-\frac{z_1}{\lambda_e \cos\alpha_I}\right) \exp\left(-\frac{1}{\cos\alpha_I} \int_0^{z_1} \frac{dz'}{\lambda_i^{v \rightarrow s}(0, E_i, z')}\right), \quad (4.18)$$

where $\lambda_i^{v \rightarrow s}(0, E_i, z')$ is the injected electron IMFP at depth z' . The factor $F_R(z_1, \alpha_R)$ is the probability density function for ejected electrons at depth z_1 to reach the surface without any elastic and inelastic interactions is written as

$$F_R(z_1, \alpha_R) = \exp\left(-\frac{z_1}{\lambda_e \cos\alpha_R}\right) \exp\left(-\frac{1}{\cos\alpha_R} \int_0^{z_1} \frac{dz'}{\lambda_i^{s \rightarrow v}(0, E_i, -z')}\right), \quad (4.19)$$

where $\lambda_i^{s \rightarrow v}(0, E_i, -z')$ is the ejected electron IMFP at depth z' . Here $\cos\alpha_R$ can be denoted by

$$\cos\alpha_R = -\cos\alpha_I \cos\theta_1 + \sin\alpha_I \sin\theta_1 \cos\phi_1 \quad (4.20)$$

due to $\Theta_1 = \pi - \alpha_R$ and $\Theta_0 = \alpha_I$ substituted into Eq. (4.7) for $i=1$. Therefore, the energy distribution of quasi-elastically backscattered electrons contributed by a single elastic scattering can be calculated using Eqs. (4.8) and (4.16) ~ (4.20).

For Si, Figs 4.9 presents the calculated energy distributions of the backscattered electrons contributed by the single scattering event using Eq. (4.16) (dotted curve) and using MC simulation method (solid curve). It is seen that the calculated results for Eq. (4.16) are in excellent agreement with the results for MC method. The similar results for Au can be seen in Fig. 4.10.



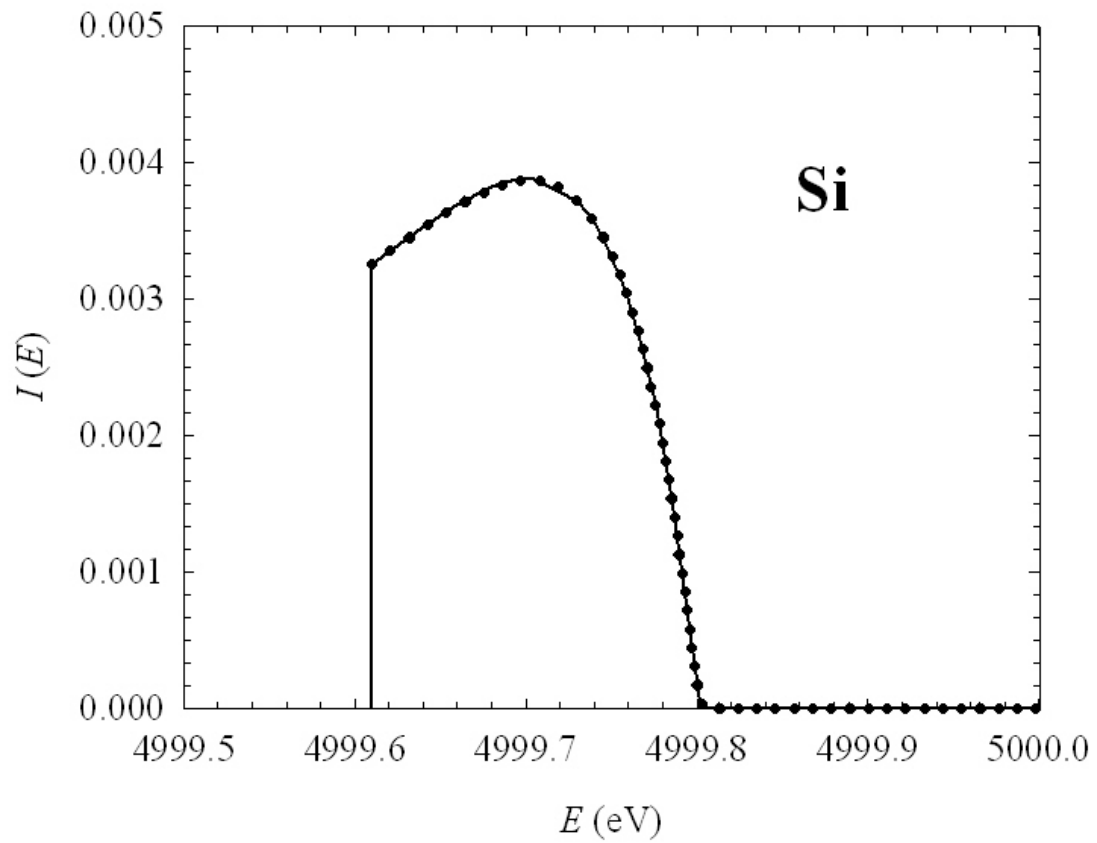


Fig. 4.9 A plot of MC results on the energy distribution of electrons quasi-elastically backscattered from Si for 5000 eV normally incident electrons suffering single elastic scattering inside the solid (solid curve). The dotted curve represents the results calculated by Eqs. (4.16) and (4.17).

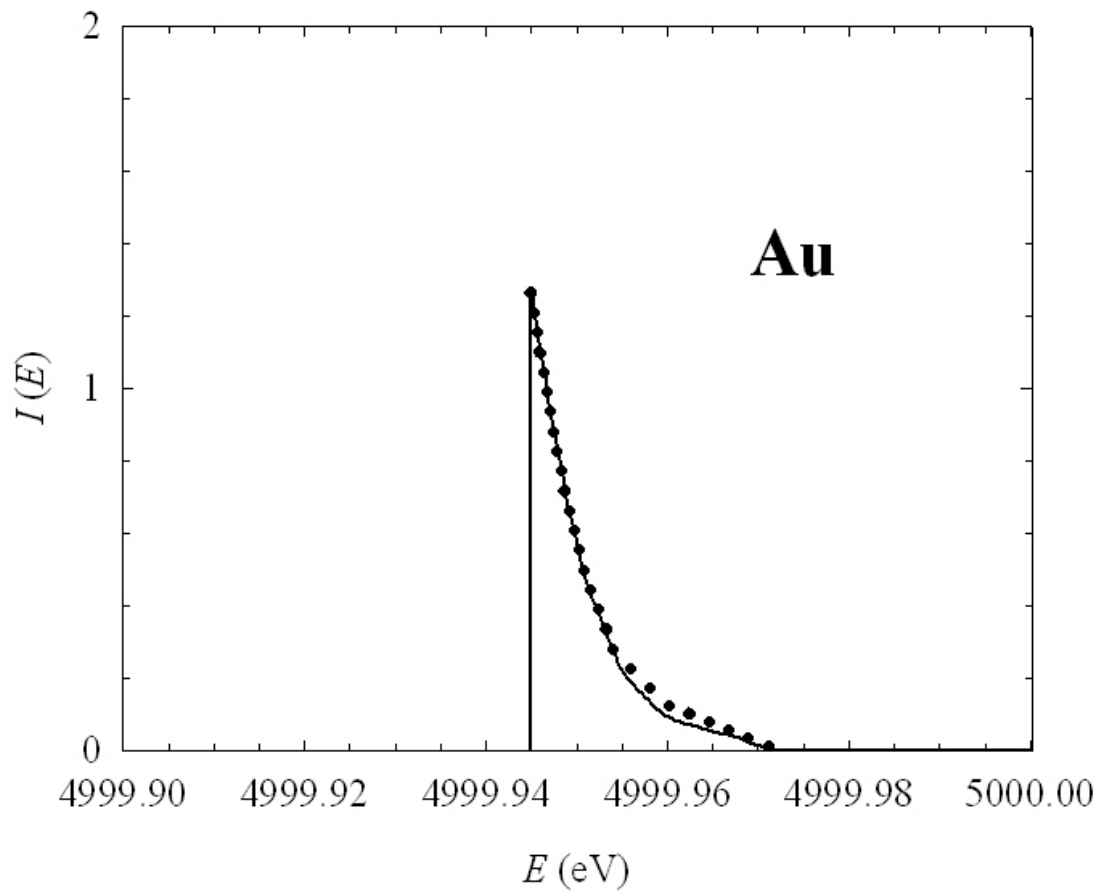


Fig. 4.10 A plot of MC results on the energy distribution of electrons quasi-elastically backscattered from Au for 5000 eV normally incident electrons suffering single elastic scattering inside the solid (solid curve). The dotted curve represents the results calculated by Eqs. (4.16) and (4.17).

4.2 Elastic Reflection Coefficient

Moreover, from Eq. (4.12), the elastic reflection coefficient for backscattered electrons within a range of energy between E_a and E_b can be calculated using

$$\eta(E_a, E_b) = \int_{E_a}^{E_b} I(E) dE. \quad (4.21)$$

Through the elastic reflection coefficients of electrons, significant information can be extracted from the elastic peak. In the later sections, we used the elastic reflection coefficients of electrons backscattered from a compound to determine the electron effective IMFPs.

4.3 Elastic Reflection Coefficient for a Compound

4.3.1 The Monte Carlo Algorithm for a Compound

In Section 4.1.1, a MC algorithm considering the SEPs and depth-dependent IMFPs was developed to calculate the intensity of electrons quasi-elastically backscattered from a solid composed of only one element. In this section, the MC algorithm is modified in order to calculate the elastic peaks of electrons backscattered from a compound.

The modification is that a new random number R_4 between 0 and 1 is introduced to determine which element in the compound scatters the electron while an elastic collision occurs. Using Eqs. (2.4), (2.5) and (2.7), the probability of an electron being scattered by the j th element in the compound composed of n kinds of elements is given by (Howell and Boyde 1998)

$$P_{\sigma_e}(j) = \frac{a_j \sigma_{e,j}}{\sum_{j=1}^n a_j \sigma_{e,j}}, \quad (4.22)$$

Applying Eq. (4.22), the j th element is collided by the electron in each elastic scattering event if

$$\sum_{j=1}^{k-1} P_{\sigma_e}(j) < R_4 \leq \sum_{j=1}^k P_{\sigma_e}(j), \quad \text{for } k = 1, 2, 3, \dots, n. \quad (4.23)$$

Eq. (4.23) can be used to determine the element which is collided by the electron. Then the EDCS of the element is taken to find the polar scattering angle θ after the scattering through the help of Eqs. (4.1) and (4.2). In addition, the average EMFP can be obtained from the individual element EMFPs in the compound according to Eq. (2.6). Note that we used the relativistic model with free-atom potentials depicted in chapter 2 to calculate the total elastic cross sections and the average EMFPs for compounds. Then the elastic peak spectra of electrons backscattered from a compound can be carried out using the modified MC algorithm. Also, the elastic reflection coefficient for electrons backscattered from a compound can be obtained.

4.3.2 Using Elastic Reflection Coefficient to Determine Electron Inelastic Mean Free Path for a Compound

The method to extract the IMFP from the elastic peak electron spectra is based on the calculation of the elastic reflection coefficient. To determine the IMFP from the elastic reflection coefficient, calibration curves are established. The calibration curves present the relation between IMFP and the ratio of the elastic reflection

coefficient for a compound sample relative to a Ni reference. In this section, the SEPs and various values of depth-independent IMFP are first applied in the modified MC algorithm. Then the calibration curves can be obtained. Besides, using the extended Drude dielectric function, the calculated depth-dependent IMFPs and SEPs were applied to determine the electron elastic reflection coefficient for a compound by means of the modified MC simulations. Subsequently, an effective IMFP for the compound can be extracted by the intersection of the calibration curve and the calculated elastic reflection coefficient.

Figure 4.11 shows the intensity ratio of electrons backscattered from GaAs to those from Ni for a 50° incident angle and $0^\circ \sim 90^\circ$ emission angles (solid circles) and for a 0° (normally) incident angle and $36.3^\circ \sim 48.3^\circ$ emission angles (solid triangles). Corresponding experimental data (open circles and triangles) (Krawczyk *et al.* 1998; Zommer *et al.* 1998) are plotted for comparisons. The differences between present results and experimental data are due to the lack of information on experimental configurations.

Figure 4.12 shows the same intensity ratio as a function of depth-independent electron IMFP, or the calibration curve, calculated using the same simulation configurations as those applied to Fig. 4.11. The solid and dashed curves are, respectively, for a 50° incident angle and $0^\circ \sim 90^\circ$ emission angles and for a 0° incident angle and $36.3^\circ \sim 48.3^\circ$ emission angles. The symbols are the corresponding results obtained by MC simulations using the depth-dependent electron IMFPs and SEPs. From the intersection of the calibration curve and the simulated intensity ratio, the effective IMFP may be determined. These results of the effective IMFP are plotted in Fig. 4.13 as a function of electron energy for a 50° incident angle and $0^\circ \sim 90^\circ$ emission angles (solid circles) and for a 0° incident angle and $36.3^\circ \sim 48.3^\circ$ emission angles (solid triangles). These results are also compared with

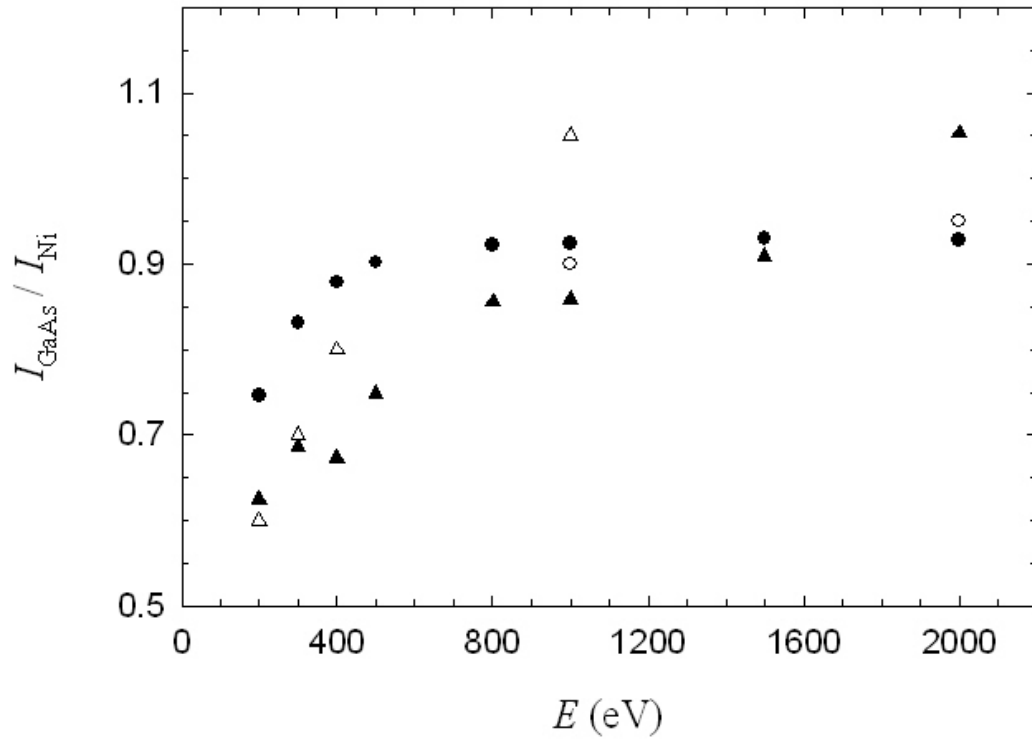


Fig. 4.11 The intensity ratio of electrons backscattered from GaAs to those from Ni for a 50° incident angle and $0^\circ - 90^\circ$ emission angles (solid circles) and for a 0° (normally) incident angle and $36.3^\circ - 48.3^\circ$ emission angles (solid triangles). Experimental data of Krawczyk *et al.* (1998) (open circles) and Zommer *et al.* (1998) (open triangles) are plotted for comparison.

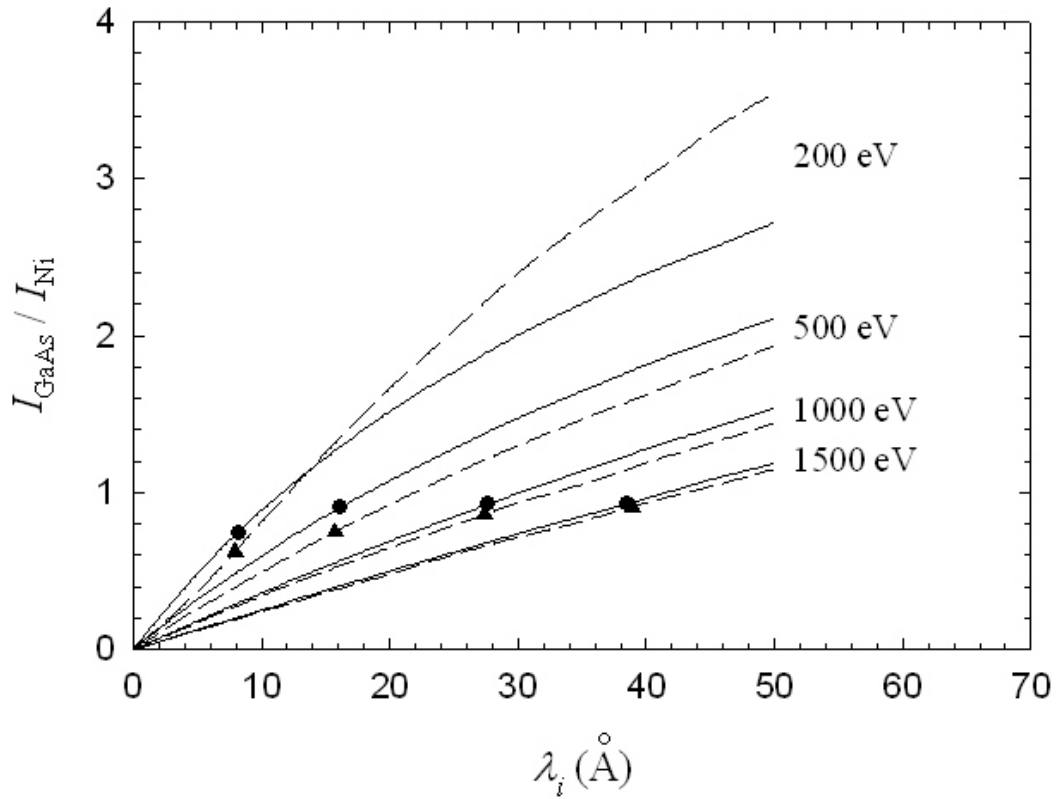


Fig. 4.12 The intensity ratio of electrons backscattered from GaAs to those from Ni calculated using the depth-independent electron IMFP (abscissa). The solid and dashed curves are, respectively, for a 50° incident angle and $0^\circ - 90^\circ$ emission angles and for a 0° incident angle and $36.3^\circ - 48.3^\circ$ emission angles. The symbols are the corresponding results obtained by MC simulations using the depth-dependent electron IMFPs and SEPs.

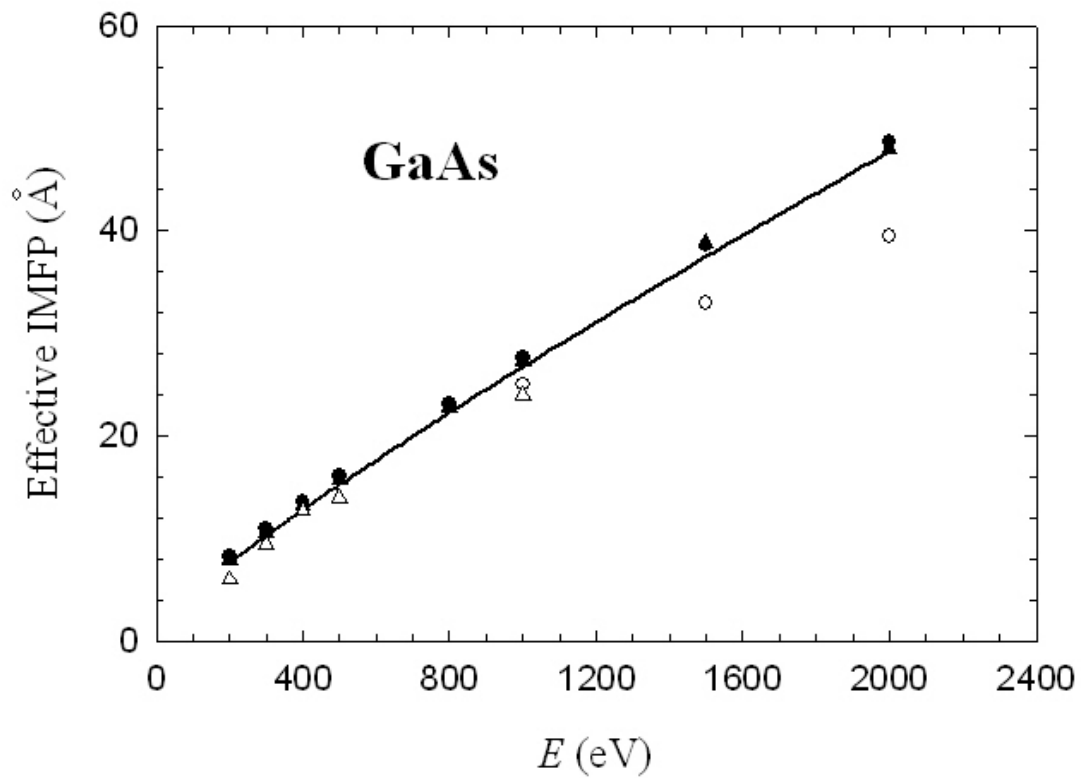


Fig. 4.13 The effective IMFP as a function of electron energy for a 50° incident angle and $0^\circ - 90^\circ$ emission angles (solid circles) and for a 0° incident angle and $36.3^\circ - 48.3^\circ$ emission angles (solid triangles). Also plotted are experimental data of Krawczyk *et al.* (1998) (open circles) and Zommer *et al.* (open triangles), and calculated IMFPs for volume excitations (solid curve).

experimental data (open circles and triangles) (Krawczyk *et al.* 1998; Zommer *et al.* 1998), and with calculated IMFPs for volume excitations (solid curve). The effective IMFPs determined here are in good agreement with electron IMFPs for volume excitations. This indicates that a depth-independent IMFP is approximately valid due to the compensation of volume and surface excitations inside the solid (Chen and Kwei 1996; Kwei *et al.* 1998b). Since parameters in the extended Drude dielectric function were fitted mainly for the response of valence electrons (Chen 2002), the lack of inner shell responses caused the deviation between calculated effective IMFPs and experimental values at high energies.



CHAPTER 5

SUMMARY

In this thesis, the elastic and inelastic interactions between electrons and solids were studied theoretically.

For elastic interaction, the non-relativistic and the relativistic approximations with free-atom and solid-atom potentials to determine EDCS and EMFP were described and compared. The calculated results showed that the relativistic elastic-scattering model is more realistic, especially for the solids composed of heavy atoms. In addition, the derivation of the electron total elastic cross sections and total EMFPs for compounds was further made based on elastic cross sections and based on elastic mean free paths of individual elements. These two methods also can determine the probability of each element in a compound being bumped by an electron. Besides, the recoil effect was also discussed for the energy loss of the electron after elastic scattering. It was found that the recoil effect is significant for atoms of low and intermediate atomic numbers.

In the research about inelastic interaction, a new model was constructed based on the dielectric response theory. Formulas were derived to calculate the stopping power, DIIMFP, IMFP and SEP for electrons escaping from and incident into solids. It was found that the DIIMFP, IMFP and SEP for electrons near surfaces are dependent of the electron's moving direction and position. These results arise from the number of the surface excitations varying with the electron's distance to the solid surface. Deep inside the solid, the DIIMFP and IMFP reduced to the values for electrons moving in the infinite solid since the spherical coordinates were adopted. With this adoption, the momentum integration limits can completely satisfy the

conservations of energy and momentum. Moreover, the inelastic-scattering model with the inclusion of retardation effect was constructed for electrons moving parallel to solid surfaces. The calculated results for high-speed electrons revealed that the stopping power and DIIMFP with retardation effect were lower than the stopping power and DIIMFP without retardation effect.

Based on the theories on the elastic and inelastic interactions of electrons with solids, we further established a MC method to simulate the energy distribution of elastic peaks of electrons backscattered from solid surfaces. The energy distribution is due to the Rutherford-type recoil energy losses occurring in elastic scatterings. The simulated results showed that the recoil energy loss caused the peak energy shift and width broadening in the ideal energy spectrum of an electron elastic peak. However, the ideal energy spectra did not agree with the experimental data well. Adjustment of the contributions from spectrometer energy resolution, the energy distribution of the primary electrons and the thermal motion of atoms were included. It was found that the width broadenings of the energy spectra of elastic peaks were mainly contributed by the spectrometer energy resolution, the energy distribution of the primary electrons and the thermal effect. Regarding the applied model of the thermal effect, it was also discussed that the recoil energy loss should be centered at the most probable value of this loss for vibrating atoms rather than for atoms at rest, and the thermal effect due to multiple elastic scatterings could shift the peak position and widen the peak. More information on both phenomena should be given to study the energy distribution of electron elastic peaks. Besides, the method to extract effective IMFPs from electron elastic peaks was discussed. We obtained the effective IMFPs for GaAs using our MC method. The obtained effective IMFPs were in agreement with the calculated IMFPs for volume excitation due to the compensation of surface excitation and volume excitation inside the solid.

References

- Abril I, García-Molina R, Denton C D, Pérez-Pérez F J and Arista N R (1998) *Phys. Rev. A* **58** 357.
- Beilschmidt H, Tilinin I S and Werner W S M (1994) *Surf. Interf. Anal.* **22** 120.
- Beiser A (2003) *Concepts of Modern Physics 6th ed.* New York: The McGraw-Hill Companies, Inc.
- Boersch H, Wolter R and Schoenebneck H (1967) *Z. Phys.* **199** 124.
- Bonham R A and Strand T G (1963) *J. Chem. Phys.* **39** 2200.
- Chen Y F, Su P, Kwei C M and Tung C J (1994) *Phys. Rev. B* **50** 17547.
- Chen Y F, Kwei C M and Su P (1995) *J. Phys. D: Appl. Phys.* **28** 2163.
- Chen Y F and Kwei C M (1996) *Surf. Sci.* **364** 131.
- Chen Y F (2002) *Surf. Sci.* **519** 115.
- Cheng D K (1989) *Field and Wave Electromagnetics, 2nd ed.* New York: Addison-Wesley.
- Chiou S Y (1998) *Thesis of Master*, Hsinchu, Taiwan: National Chiao Tung University.
- Clementi E and Roetti C (1974) *Atomic Data and Nuclear Data Tables* **14** 177.
- Cowley J M (1982a) *Phys. Rev. B* **25** 1401.
- Cowley J M (1982b) *Surf. Sci.* **114** 587.
- Ding Z-J and Shimizu R (1996) *Scanning* **18** 92.
- Dolinski W, Mröz S and Zagórski M (1988) *Surf. Sci.* **200** 361.
- Dressel M and Grüner G (2002) *Electrodynamics of solids: Optical Properties of Electrons in Matter, 1st ed.* United Kingdom: Cambridge University Press.
- Egerton R F (1986) *Electron Energy-Loss Spectroscopy in the Electron Microscope*

- New York: Plenum.
- Erickson N E and Powell C J (1989) *Phys. Rev. B* **40** 7284.
- Flores F and García-Moliner F (1979) *J. Phys. C.* **12** 907.
- García-Molina R, Gras-Martí A, Howie A and Ritchie R H (1985) *J. Phys. C* **18** 5335.
- Gauvin R, L'Espérance G. and St Laurent S. (1992) *Scanning* **14** 37.
- Gergely G (1981) *Surf. Interf. Anal.* **3** 201.
- Gergely G, Sulyok A, Menyhard M, Tóth J, Varga D, Jablonski A, Krawczyk M, Gruzza B, Bideux L and Robert C (1999) *Appl. Surf. Sci.* **144-145** 173.
- Gergely G, Menyhard M, Benedek Zs, Sulyok A, Kövér L, Tóth J, Varga D, Berényi Z and Tökési K. (2001) *Vacuum* **61** 107.
- Goto K and Shimizu R (1997) *Proc. Inter. Symp. Atomic Level Characterization for Materials and Devices '97 (Maui, Hawaii) The Microbeam Anal.* vol 141 *Comp. Japan. Soc. Promotion Science*, p 403.
- Gruzza B and Pariset C (1991) *Surf. Sci.* **247** 408.
- Green A J and Leckey R C G (1976) *J. Phys. D: Appl. Phys.* **9** 2123.
- Howell P G T and Boyde A (1998) *Scanning* **20** 45.
- Hsu Y. H. (2003) *Thesis of Master*, Hsinchu, Taiwan: National Chiao Tung University.
- Jablonski A (1985) *Surf. Sci.* **151** 166.
- Jablonski A, Gryko J, Kraaer J and Tougaard S (1989) *Phys. Rev. B* **39** 61.
- Jablonski A (1991) *Phys. Rev. B* **43** 7546.
- Jablonski A, Hansen H S, Jansson C and Tougaard S (1992) *Phys. Rev. B* **45** 3694.
- Jablonski A, Jansson C and Tougaard S (1993) *Phys. Rev. B* **47** 7420.
- Jackson J D (1975) *Classical Electrodynamics, 2nd ed.* New York: Wiley.
- Jardin C, Gergely G and Gruzza B (1992) *Surf. Interf. Anal.* **19** 5.
- Joachain C J (1975) *Quantum Collision Theory*, North-Holland, Amsterdam.

- Kirschner J and Staib P (1973) *Phys. Lett.* **42** 335.
- Kirschner J and Staib P (1975) *Appl. Phys.* **6** 99.
- Krawczyk M, Jablonski A, Tougaard S, Tóth J, Varga D and Gergely G (1998) *Surf. Sci.* **402** 491.
- Kwei C M (1984) *Thin Solid Films* **111** 83.
- Kwei C M, Chen Y F, Tung C J and Wang J P (1993) *Surf. Sci.* **293** 202.
- Kwei C M, Su P, Chen Y F and Tung C J (1997) *J. Phys. D: Appl. Phys.* **30** 13.
- Kwei C M, Chen Y F and Tung C J (1998a) *J. Phys. D: Appl. Phys.* **31** 36.
- Kwei C M, Wang C Y and Tung C J (1998b) *Surf. Interface Anal.* **26** 682.
- Kwei C M, Chiou S Y and Li Y C (1999) *J. Appl. Phys.* **85** 8247.
- Kwei C M, S S Tsai and Tung C J (2001) *Surf. Sci.* **473** 50.
- Kwei C M, Hwang S J, Li Y C and Tung C J (2003) *J. Appl. Phys.* **93** 9130.
- Laser D and Seah M P (1993) *Phys. Rev. B* **47** 9836.
- Lesiak B, Kosinski A, Krawczyk M, Zommer L, Jablonski A, Zemek J, Jiricek P, Kővér L, Tóth J, Varga D and Cserny I (1999) *Appl. Surf. Sci.* **144-145** 168.
- Marks L D (1982) *Solid State Commun.* **43** 727.
- Mott N F (1929) *Proc. R. Soc. A* **124** 425.
- Murata K, Yasuda K and Kawata H (1995) *Scanning* **17** 228.
- Moreau P, Brun N, Walsh C A, Colliex C and Howie A (1997) *Phys. Rev. B* **56** 6774.
- Ohanian H. C. *Principles of Quantum Mechanics*, New Jersey: Prentice-Hall.
- Oswald R (1997) *Ph.D. thesis*, University of Tübingen.
- Reimer L (1985) *Scanning Electron Microscopy*, New York: Springer.
- Ritchie R H (1957) *Phys. Rev.* **106** 874.
- Shimizu R and Ding Z-J (1992) *Repors Progr. Phys.* 487.
- Su P, (1994) *Thesis of Master*, Hsinchu, Taiwan: National Chiao Tung University.
- Sulyok A, Gergely G, Menyhard M., Tóth J, Varga D, Kővér L, Berényi Z, Lesiak B

- and Kosinski A (2001) *Vacuum* **63** 371.
- Tanuma S, Powell C J and Penn D R (1988) *Surf. Interf. Anal.* **11** 577.
- Tanuma S, Powell C J and Penn D R (1991a) *Surf. Interf. Anal.* **17** 911.
- Tanuma S, Powell C J and Penn D R (1991b) *Surf. Interf. Anal.* **17** 927.
- Tanuma S, Ichimura S and Goto K (2000) *Surf. Interf. Anal.* **30** 212.
- Tóth J, Varga D, Cserny I, Kóvér L, Gruzza B, Zeze D, Jardin C and Gergely G (1998) *Vacuum* **50** 473.
- Tucker T C, Roberts L D, Nestor C W and Carson T A (1969) *Phys. Rev.* **178** 998.
- Tung C J, Chen Y F, Kwei C M and Chou T L (1994) *Phys. Rev. B* **49** 16684.
- Tung C J and Ritchie R H (1977) *Phys. Rev. B* **16** 4302.
- Varga D, Tókési K, Berényi Z, Tóth J, Kóvér L, Gergely G and Sulyok A (2001) *Surf. Interf. Anal.* **31** 1019.
- Yubero F and Tougaard S (1992) *Phys. Rev. B* **46** 2486.
- Yubero F, Sanz J M, Ramskov B and Tougaard S (1996) *Phys. Rev. B* **53** 9719.
- Zommer L, Lesiak B, Jablonski A, Gergely G, Menyhard M, Sulyok A and Gurban S (1998) *J. Elect. Spectrosc. Rel. Phenomen.* **87** 177.

簡 歷

姓 名：黎 裕 群

性 別：男

出生日期：民國 66 年 10 月 12 日

出 生 地：台灣省花蓮縣

學 歷：

國立交通大學電子工程學系畢業（85 年 6 月～89 年 2 月）

國立交通大學電子研究所碩士班（89 年 2 月～90 年 2 月）

國立交通大學電子研究所博士班（90 年 2 月入學）



論文名稱：準彈性反射電子模擬與分析

The Simulation and Analysis of Quasi-elastically Backscattered
Electrons

PUBLICATION LIST

Referred Journal Papers:

1. **Y. C. Li**, Y. H. Tu, C. M. Kwei and C. J. Tung, "Influence of the Direction of Motion on the Inelastic Interaction between Electrons and Solid Surfaces," **Surf. Sci.** (accepted)
2. C. M. Kwei and **Y. C. Li**, "Electron inelastic mean free paths and surface excitation parameters for GaAs," **Appl. Surf. Sci.** **238**, 151 (2004).
3. C. M. Kwei, **Y. C. Li** and C. J. Tung, "Energy Spectra of Electrons Quasi-elastically Backscattered from Solid Surfaces," **J. Phys. D: Appl. Phys.** **37**, 1394 (2004).
4. C. M. Kwei, S. J. Hwung, **Y. C. Li**, and C. J. Tung, "Energy Losses of Charged Particles Moving Parallel to the Surface of an Overlayer System," **J. Appl. Phys.** **93**, 9130 (2003).
5. C. M. Kwei, S. Y. Chiou and **Y. C. Li**, "Electron Inelastic Interaction with Overlayer Systems," **J. Appl. Phys.** **85**, 8247 (1999).

International Conference Papers:

1. C. M. Kwei, **Y. C. Li** and C. J. Tung, "Angular and Energy Dependences of the Surface Excitation Parameter for Electrons Crossing a Solid Surface," in **23rd European Conference on Surface Science (ECOSS 23)**. (accepted)
2. C. M. Kwei and **Y. C. Li**, "Electron inelastic mean free paths and surface excitation parameters for GaAs," in **1st International Meeting on Applied Physics (APHYS 2003)**, pp. 314 (2003)